GEOCHEMICAL PROPERTIES AND ENVIRONMENTAL IMPACTS OF THE MAZINO COAL DEPOSIT, CENTRAL IRAN

Mohammad Yazdi[a] and Hadi Golzar[a]

Keywords: Coal composition, Tabas coalfield, Central Iran

Tabas coalfield is one of the most important coalfields in Central Iran. The area is located in the central desert of Iran, very far from any inhabited areas. Mazino is the largest thermal coal deposit in Tabas coalfield. Coal-bearing strata in Tabas coalfield (as well as in Mazino deposit) are within the Middle Jurassic formations. This sedimentation has been developed in alluvial plain and coastal environment in Tabas coalfield. The coal-bearing sediments mainly consist of sandstone, shale, siltstone, and carbonatic rocks. Several coal seams with different thickness are interbedded with these sediments. Petrographic observations have shown that coals of the Mazino deposit are mainly anthracite to semi-anthracite and dominated by macerals of the vitrinite group; amounts of inertinite macerals are relatively very low. The dominant mineral phases of these coals are pyrite, siderite, calcite, gypsum, illite, and clays. The Mazino coals have high ash (average of 27.78%), low volatile matter (average of 5.2%), and high sulphur (average of 2.62%) content, and high calorific value with average of 22.94 MJ/Kg. The chemical composition shows that the Mazino coals range from semi-anthracite to anthracite (thermal coal), which are suitable as power-plant fuels with low chemical hazards to environment in the area.

* Corresponding Authors
Fax: +98212990643
E-Mail: m-yazdi@sbu.ac.ir
[a] Faculty of Earth Science, Shahid Beheshti University P.O. Box.19396-4716, Evin, Tehran, Iran

Introduction

The coal is going to have new role in the economy of Iran. The coals in Iran are generally used for metallurgical purposes, however, due to increasing oil price, Iran is going to use thermal coal deposits as new energy sources. Since 10 years, the first Iranian coal power plant is going to be established in central Iran, at Tabas coalfield. It is one of the five coal power plant projects that will be established in central and northern coal basins of Iran.

Tabas coal resources are estimated to be about 2 Gt, most of them occur in two main areas, in Parvadeh and Mazino. Our study area is located in the Mazino area which is a steaming coal deposit. The Mazino deposit with 650 Mt estimated reserve is the largest steaming coal deposit not only in Tabas coalfield but also in all parts of Iran. Geological studies on Mazino coal deposits started in the 1995 by Iran Steel Company. During the last decades, several investigations involving geology, drilling, and even palynology were performed in order to study the relationship between coal-forming environments and coal properties in the Tabas coalfield. No systematic petrological and geochemical investigations were performed during the following decades, and published data about Mazino coal deposit is limited. The aims of the present paper are to explain coal geochemistry and coal quality in the Mazino deposit. During different exploration activities 123 boreholes have been made in different depths up to 600 m. During these explorations by Tabas Steel Co. and Russian TPE Co., about 1000 samples from different trenches and boreholes have been analyzed for ash, sulphur, moisture, volatile matter, and heating value. 30 representative coal samples from different trenches and boreholes have been chosen for this study. This research is mainly based on the interpretation of seam geology, petrography, and ash yields. Finally, we use a combination of petrography and geology to yield additional information on the coal-forming environments and reconstruct the depositional environment of Iran coal-bearing formations. The ash and sulphur contents of coals are very important factors for using coals in power plants. These factors depend on the environment of deposition and subsequent geological history. Therefore, geological history and reconstruction of the depositional environment of these coals would give useful information.

Geological setting

Geological studies have been limited so far in the Tabas coalfield, central Iran. Comprehensive literature reviews[1-4] of the geological character of Iranian coals are available. In the early geological work, the emphasis was on the determination of the minability of the coals in the Tabas coalfield.

The Mazino deposit is located in the western part of the Tabas coalfield (Fig.1). [5] The Tabas coalfield includes Mazino and Parvadeh deposits but there are also coal seams in Kemar Mehdi, Kalishour, and Kouchek Ali areas, close to Mazino deposits. These coal seams are also steaming coals. All of these coals are formed within the Middle Jurassic formations. The coal-bearing sediments in the Mazino area are called Mazino (Hojadk) Formation (central Middle Jurassic).

The Mazino Formation mainly consists of sandstone, shale, siltstone, and carbonatic rocks. The thickness of Mazino Formation is about 1200m in the Mazino area and gradually decreases to the east of the area. Several coal seams (26 coal seams) with different thickness are interbedded with these sediments. The thickness of coal layers in different places varies from 0.5 to 15 m.

DOI: 10.17628/ecb.2012.1.125-129

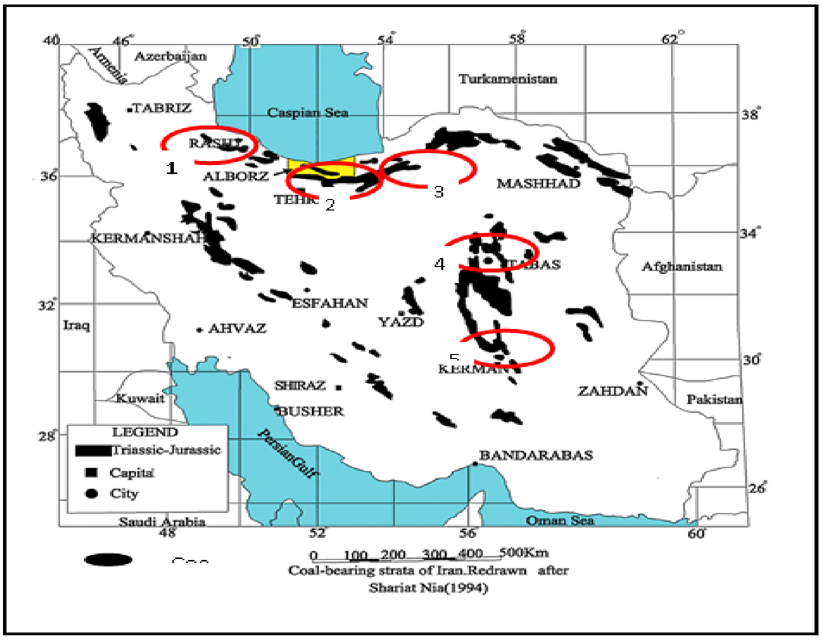

Coal-bearing strata of Iran.Redrawn after Shariat Nia(1994)

Fig. 1. The Mazino coal deposit in the Tabas coalfield, in central Iran (1-Lushan coalfield in Western Alborz zone; 2-Zirab coalfield in Central Alborz zone; 3-Shahroud coalfield in Eastern Alborz zone; 4- Tabas coalfield in Central Iran zone; 5- Kerman coalfield in Central Iran zone)

The Mazino Formation is underlined by the upper Middle Jurassic oolitic limestones (Badamu Formation). It is composed of sandy to oolitic limestones and organic detrital matters that overlain the sandstones. The thickness of Badamu Formation is about 60 m in the Mazino area. The Mazino Formation is also overlained by the lower Middle Jurassic sandy oolitic limestones (Tabas or Parvadeh Formation). Parvadeh Formation is dark oolitic and crystalline limestone. The thickness of Parvadeh Formation is about 40 m in the Mazino area.

The above explanation shows that shallow marine environment was developed in the Tabas basin, whereas the continental alluvial plain was developed in the northern part of Iran in the Alborz basin.[6] The main coal deposits were developed in both the alluvial and littoral plains. During the end of the Upper Middle Jurassic, the marine transgression dominated, and shallow marine and littoral plain environments covered the Tabas basin. The Central Middle Jurassic coal-bearing deposits in the Tabas basin and also in Mazino area have been formed in the shallow marine and littoral plain environments.

All of the coal seams in the Mazino Formation are formed within the complicated monoclines and synclinal folds. The geology of the area is within a syncline which has been deepen to east, and has been cut by several faults. The general dip of strata and coal seams vary from 6° to 25 °E. Coal seams of the Mazino deposit are characterized by a complicated and variable structure due to the presence of intraseam dirt bands and due to the variation of their thickness within a broad range. Therefore, the reserve calculation is very complicated. The method of geological block was used by Russian geologists to estimate coal reserve[8-9].

Coal reserves for categories of C_1 and C_2 were calculated separately for oxidized and non-oxidized coals. The reserve of useful coals (anthracite) was calculated on the basis of isolines of thickness of mine able coal seams and dirty coal bands. Coal reserves mainly belong to the seams with irregular thickness, such as, M_1, M_2, M_6, M_9, M_{10}, M_{14} (78.5%) and coal seams with relatively regular thickness such as M_4, M_5 and M_8.

The mineable coal reserve in the Mazino area was calculated by Iranian geologists as follows; in category of C_1 pure coal seams were estimated to be about 146 Mt for 30% ash contents and estimation for dirty coal seams was 211 Mt for 50% ash contents. The estimation in category of C_2, for pure coal seams was 316 Mt and for dirty coal seams was 417 Mt.[7] The detailed mineable coal reserve was also calculated by Russian geologists. According to their reserve estimation, in category of C_1 pure coal seams were estimated to be about 147 Mt for 28% ash contents and estimation for dirty coal seams was 250 Mt for 48% ash contents.

Analytical methods

The samples were chosen to represent a significant variation in rank. Most samples were selected from distinct clean coal layers and thus have lower mineral contents than the run-of-mine coal. 500 coal samples were collected from 10 different main coal seams, boreholes, and trenches. The samples were chosen from layers of M1-M9 and in depth of below 20 m (below coal oxidation zone). All samples were analyzed for ash, volatile matters, moisture, heating value, and sulphur at the department of chemical laboratory of Energy Ministry of Iran, Foolad Tabas and Rostov regional laboratory center in Yuzhgeologiya of Russia. The ash, volatile matters, moisture, and sulphur values are reported as wt/wt in this study.

The coal samples were initially crushed to smaller than 850 μm and then homogenized. The crushed samples were stored in sealed containers under an inert atmosphere to avoid oxidation. Then, 100 g from each sample was heated to 850 °C for three hours and the ash percentage was determined by analytical balance (conventional method). Other factors also were determined according to Russian GOST (Russian: *ГОСТ*) standard. The results of the analyses are given in Tables 1 and 2.

Petrographic details have been studied at Skochinsky Institute of Mining in Russia. Also, average value of reflection of vitrine and sum of depleted components were analyzed in this institute by Russians. The results of the analyses are given in Table 3. 5 samples were analysed by XRD (Phillips 1400) in Iranian laboratory and 10 samples were analysed in Russia at Rostov laboratory by XRD (DRON-6).

Table 1. Average values of ash, total sulphur, moisture, volatile matter (in wt/wt), and heating value of different samples from Mazino coal deposit

Ash (Ad%)	Sulphur (St%)	Moisture (Wa%)	Volatile matter (Vd%)	Heating Value MJ/kg	C (%)	H (%)	O+N (%)
(n=359)	(n=183)	(n=359)	(n=199)	(n=480)	(n=183)	(n=183)	(n=183)
27.78	2.62	0.68	5.2	22.94	89.87	3.40	6.73

Table 2. Average values of ash and total sulphur (as % wt/wt) in representative samples (n=19) from coal seams and rock inter layers of Mazino coal deposit

Layer No.	Thickness Layer	Thickness coal seam	Ash% Layer	Ash% coal seam	St% Layer	St% coal seam
M1	4.32	2.58	48.73	25.10	2.98	3.41
M2	7.08	3.47	57.17	27.87	1.82	2.26
M4	1.70	1.35	36.95	26.08	2.83	3.17
M5	1.74	1.29	40.67	28.43	1.80	1.96
M6	2.67	1.25	54.39	36.47	2.42	2.73
M8	1.04	0.70	42.53	34.40	2.27	2.50
M9	2.18	1.25	47.35	29.66	1.37	1.52
Average	2.96	1.69	50.56	28.68	2.13	2.56

Table 3. Average value (n=19) for reflection of vitrain in oil (RO), anisotropy reflection (AR), and sum of depleted components (O) from coal seams of Mazino coal deposit

Layers No.	RO	AR	O
M1	2.96	8.5	9.2
M2	2.88	11.1	7.5
M4	2.78	8.3	9.0
M5	2.80	10.0	4.8
M6	2.89	7.3	3.7
M8	2.60	13.05	7.0
M9	2.83	9.9	7.0
M10	3.0	7.6	5.5
Average	2.84	9.47	6.71

Results and discussions

The ash, sulphur contents, heating values, major chemical compounds, major mineral compounds, volatile matters, and moisture of coals are very important factors for using coals in power plants.

These factors mainly depend on the environment of deposition and subsequent geological history. Therefore, the factors are explained as follows:

Ash contents

The result of the analyses of 500 samples shows that all of coal seams in the Mazino deposit have relatively high ash content except coals in M1 and M2. Average of ash contents in rock inter layers is 50.56% and in coal seams 27.78%. We have to take into account that high ash content in coal seams occurs due to rock particle contamination.

Volatile matters and moisture

199 samples were analysed for volatile matters in different Iranian laboratories and 19 samples were analyzed in Russia at Rostov laboratory. The result of analyses shows that the content of volatile matters (Vdaf) ranges from 4.4% to 7.3% with average of 5.2%. 359 samples were analysed for moisture in Iranian laboratory.

DOI: 10.17628/ecb.2012.1.125-129

The result of analyses shows that the moisture content ranges from 0.1% to 2.3% with average of 0.68%.

Major chemical compounds

183 samples were analyzed in Iranian laboratory and 19 samples were analyzed in Russia at Rostov laboratory. The result of analyses shows that sulphur content varies from 1.52 to 3.41, while layers of M1, M4, and M6 have relatively high sulphur. Average of sulphur contents in layers is 2.13% and in coal seams is 2.56%. The sulphur contents in the studied samples can be divided into two groups: a) in the samples with less than 1.5% sulphur, sulphatic sulphur is 0.05% and in the other part, sulphur is approximately equally distributed between pyrite and organic sulphur. b) In the samples with more than 1.5% of sulphur, total sulphur is 2.96%. In these samples the average of sulphatic sulphur is 0.12%, organic sulphur is 0.92%, and pyritic sulphur is 1.92%.[8] These samples were also analysed for C, H, and O+N in Iranian laboratory. The results show average values of C=89.87%, H=3.40% and O+N=6.73% (Table 1).

Heating values

480 samples were analyzed for heating value in Iranian laboratory and in Russia at Rostov laboratory. The result of analyses shows that heating value content varies from 15.21 to 39.32 MJ/kg with average of 22. 94 MJ/kg.

Reflection ability of vitrain

The reflection ability of vitrain was analyzed in Russia at laboratory of Skochinsky institute of mining. Reflection of vitrain in oil (RO) changes within the limits of 2.60 to 3.0 % in different coal layers with average of 2.84 %. Anisotropy of reflection ability of vitrain in air (AR) varies from 7.3 to 13.05 with average of 9.47. The sum of depleted components (O) varies from 3.7 to 9.2 with average of 6.71. Reflection of vitrain in oil is characterized by the low values not exceeding 3.0 % and sum of depleted components not exceeding 9.2 %. The vitrinite reflectance in these coals exceeds 9.9 %. The vitrinite reflectance’s (R_{max}) is ranging from 1.71 % to 2.45 %, spanning the low volatile semi anthracite to anthracite rank.

According to petrographic studies the coals are anthracite to lean-anthracite.[9] The reflection ability of vitrain and sum of depleted components on the maceral structures of these coals also confirm that these coals are anthracite type. In these coals, the dominant maceral phases are vitrinite group and the amounts of inertinite and exinite macerals are relatively very low.

Major mineral compounds

The XRD analysis and petrographic studies showed that dominant mineral phases of these coals are quartz, pyrite, marcasite, siderite, ankerite, calcite, gypsum, halite, barite, illite, sericite, and clays. The clays are argillite, kaolinite, and montmorilinite. Semi quantitative XRD analysis shows that the major minerals are as 70-80% of free silica (mainly quartz and argillite). Under microscope argillites and quartz are the main mineral phases in coals. The argillites have mainly pelitic texture, and quartz has mainly angular textures[10-11].

These coals have the carbonate syngenetic sequence, but a complete sulfide syngenetic precipitation sequence is characterized by radial marcasite precipitation phases and euhedral and massive pyrite. This high-sulfide mineralization stage is probably due to the marine influence affecting the Tabas basin as well as the Mazino area.

Conclusions

The Mazino coals from Tabas basin in central Iran were investigated for their geological, geochemical, and coal properties. The studies show that the Central Middle Jurassic coal-bearing deposits in the Tabas basin and as well as in Mazino area have been formed in the shallow marine and littoral plain environments. The dominant maceral phases of these coals are vitrinite (97-100%) and inertinite (1-3%). The dominant mineral phases are kaolinite, quartz, illite, siderite, and argillite. Traces of calcite, pyrite, and marcasite are also evident. The Mazino coals have reflectances consistent with low volatile matters through anthracite to semi-anthracite rank. These coals have maximum vitrinite reflectance of 9.9%. The vitrinite reflectances (R_{max}) are ranging from 1.71% to 2.45%. Both C and H contents of these coals indicate semi-anthracite to anthracite rank. Data from these studies show that the Mazino coals have high-ash (27.78%), high sulfur (2.6%), low volatile matter (5.2%), low moisture contents (0.68%), and intermediate calorific value (23 MJ/kg).

All of these data show that the Mazino coals range from semi-anthracite to anthracite (thermal coal), which are suitable as power-plant fuels with low chemical hazards to environment in the area. In addition, the area is located in central desert of Iran very far from any inhabited area.

Acknowledgments

The author would like to express his gratitude to Mr. Rabbani vice dean of Managing director of Iran Power Development Co. (IPDC) and Mr. Zirak Zadeh head of Tabas project, those give me opportunities to work as consultant of this project and his colleague for their supports, to Russian company of TPE and Foolad Tabas geologists for their generous helps during the sampling, geochemical and petrological studying of samples.

References

[1] Yazdi M., Coal - from origin to environmental impacts, Polytechniques Jahad Daneshgahi Publishing Co., **2003**, 263 p. (in Persian).

[2] Zadeh Kabir A., A national project to study coals for developing of Iranian steel plans, National Iranian Steel Company, Internal report, **1991**, 745 p. (in Persian).

DOI: 10.17628/ecb.2012.1.125-129

[3] Shariat Nia H., Geological characteristics of the Parvadeh region of the Tabas coal-bearing basin, Central, Iran, Report, **1993**. 22 p.

[4] Razavi Armagani M. B. and Moinosadat S.H., Coal of Iran, Geological Survey of Iran, **1994**, 286 p. (in Persian).

[5] Yazdi M., 32nd international Geological Congress, Florence, Italy, **2004**, Part. 2, pp. 881.

[6] Yazdi M., Int. Earth Sci. Coll. Aegean Regions, Turkey, IESCA-2005, **2005**, p. 173.

[7] Foolad Tabas, Steaming coal exploration project in Mazino, Tabas, Preliminary report, **2001**, *17,* 220p.

[8] Provisional results of chemical and coal-petrographic analyses of coal from Mazino deposit, Iran TPE Report, Power Development Company (IPDC), **2003**, 24 p.

[9] Review of the data of preliminary exploration of Mazino-1, TPE report, Iran Power Development Company (IPDC), **2002**, 242 p.

[10] Golzar H., Geochemistry and mineralogy of coals in the Mazino deposit of Tabas, MSc thesis, Faculty of Earth Science, Shahid Beheshti University, unpublished, **2007**, pp. 121.

[11] Golzar H., M. Yazdi and A. Khakzad, Maceral and mineral in coals of Mazino deposit, proceeding of 14th meeting of crystallography and mineralogy in Iran, **2007**, p.297-302.

Received: 26.08.2012.
Accepted: 02.09.2012.

DOI: 10.17628/ecb.2012.1.125-129

THE VERSATILITY OF HETEROAGGREGATION IN MICROGEL SYSTEMS

Azwan Mat Lazim[a]

Keywords: homoaggregation, heteroaggregation, particles, microgels, external effects

Many researchers have studied aggregation of microgel particles; however, the majority of these studies have been limited to single-component system in which homoaggregation is observed. On the other hand, less attention has been given to multi-component systems whereby heteroaggregation is seen. As such, heteroaggregation is not only important in various applications but is interesting from a fundamental point of view. In such a way, aggregation is driven not only by attractive electrostatic interactions, but also the presence of repulsive forces. Therefore this review discussed on the theoretical background, external effects on heteroaggregation and their potential applications.

Corresponding Authors
Fax: +60389215410
E-Mail: azwani79@ukm.my
[a] School of Chemical Sciences & Food Technology, Faculty of Science & Technology, Universiti Kebangsaan, Malaysia, 43600 Bangi, Malaysia

Introduction

There is considerable interest in developing methods to aid in phase separation and recovery of colloidal systems with as little energy expenditure as possible. Traditional methods such as ultracentrifugation, variation of pressure, temperature, solvent evaporation and antisolvents have been used for many years but are energy intensive.[1] Traditional adsorbents include activated carbon, persimmon tannin gel, ion-exchange resins, tannin and fungal biomass.[2] Unfortunately, they are often ineffective at removing nanoparticulate inorganic and small-molecule impurities. Consideration of the environmental impact of these techniques is also now much more important and so alternatives are being sought.[2] Thus, it is a challenge to fabricate a sustainable procedure with very low environmental impact in conjunction with control over colloid ‘instability’ and ‘stability’.

Over the last two decades, there has been much interest in the generation and properties of colloidal microgels, with new and exciting developments being driven by subtle and sophisticated methods. Due to their flexiblity and ease of handling, many useful materials have been developed; this has led to a wide spectrum of creative approaches to combine them with organic and inorganic compounds. Microgels have many significant applications such as sensors[3], pharmaceuticals[4], catalyst carriers[5] and for environmental clean-up.[6]

For many years, research has focused on developing monodisperse microgel systems, with many studies devoted to the synthesis of colloidal particles with diameters in the range 100-1000 nm. However, the majority of these studies have been limited to single-component systems. To date, there is currently considerable interest in the preparation and application of mixed microgel systems and their colloidal heteroaggregation. Microgel dispersions are generally stable; however they can also exhibit aggregation in the swollen state due to a low effective Hamaker constant.[7] The aggregation process composed by different particles is known by three different names: heteroaggregation, heterocoagulation or heteroflocculation. These terms are interchangeable but each definition pertains to a specific process. Heterocoagulation is generally used to describe irreversibility of aggregation due to permanent contact between particles. A coagulated aggregate separates out by sedimentation if it is denser than the medium, or form a creamy phase (creaming) if its density is less than that of the dispersion medium. Heteroflocculation refers to reversible or temporary contact between particles, whilst heteroaggregation is a general term which refers to particle aggregation.[8]

Interestingly, systems made from a mixture of anionic and cationic particles can be modified to meet certain requirements. Heteroaggregation occurs when there is an attractive interaction between the different particles of a mixed dispersion, which is at least as strong as the attraction between particles of the same type. According to Islam *et. al.*[8] an ideal heteroaggregate structure forms when there is only an attractive interaction between different particle types. This is most frequently achieved by mixing dispersions of particles with opposite charges.

The dispersion and aggregation of microgel particles can be manipulated by external stimuli such as temperature, pH or presence of electrolytes. Such materials also offer many promising applications with controllable ‘on’ and ‘off’ systems. This review focuses on the heteroaggregation of microgels and discusses the background, techniques and the parameters that cause destabilisation. The development of significant experiments will be discussed, including structural characterizations along with a description of the properties and applications of heteroaggregation.

General theory of aggregation

The developments in the theory of heteroaggregation are based upon the energy interactions of the electrical double layer on the surface of the particles. Derjaguin[9] was amongst the first to theoretically determine the interaction and

DOI: 10.17628/ecb.2012.1.130-134

adhesion of dissimilar particles in the presence of electrolytes. Using a non-linear equation developed from Poisson-Boltzmann theory, the interactions between spherical particles with unequal potentials at constant force was solved. This model was then simplified by Hogg *et. al.*[10] by combining the Poisson-Boltzmann linear equation with Debye-Huckle theory. This finding is applicable to spherical particles with unequal surface charges. However, approximations must be made when particle sizes and surface potentials are very small. In order to solve this problem, the Derjaguin approximation has been used in cases where the value of the electrical double layer is smaller than the particle size and surface potential.[9]

In systems which undergo aggregation, the number of clusters involved depends on the aggregation of small particles and their combination with the existing clusters.[14-16] The first order of cluster aggregation depends on the concentration of small species, whilst the second order is directly related to the concentration of particular clusters. Puertas *et. al.*[11] studied the heteroaggregation kinetics for different charged particles. They suggested a general approach in dilute systems, which consider only binary collisions. The aggregation kinetics can then be described by:

$$\frac{dn^m(t)}{dt} = \sum_{i,j}^{\infty} k^{i,j} n^{i(t)} - n^m(t) \sum_{k=1}^{\infty} k^{m,k} n^k(t) \qquad i \oplus j = m \qquad (1)$$

where n^m is the concentration of aggregates with a configuration *m*, and the summations are over configurations. The first summation describes the formation of *m*-clusters, from any two clusters that can produce the final configuration *m* ($i \oplus j = m$). The second term rationalizes the disappearance of aggregates. Finally, for every aggregation reaction between two clusters, *i* and *j*, the reaction constant must be specified, $k^{i,j.}$

Fundamental techniques for heteroaggregation analysis

Light scattering, either static light scattering (SLS) or dynamic light scattering (DLS), usually being used to measure the heteroaggreagtion rate constant especially at early stage of aggregation. The Rayleigh-Debye-Gans (RDG) approximation is usually applied to calculate the rate constant from light scattering.

Ryde and Matijevic[18] have successfully explored RDG theory to support their light scattering data and reported that absolute heteroaggregation rate constants can be determined by analyzing time-dependent multi-angle static light scattering (SLS). Using the RDG theory, Galetto's group have focused on the time resolved simultaneous static and dynamic light scattering (SSDLS) of larger and complex particles.[17] More recently, they reported detailed heteroaggregation rate constants of amidine latex particles, sulfate latex particles, and silica particles using different ionic strengths and surface charge densities based on SLS and DLS based on DLVO theory.[13]

Clusters are formed as a result of interactions between soft particles and hard particles. Reversibility was studied by Vincent *et. al.*[19,20] and an aggregation mechanism was proposed by determining the fractal dimensions of the aggregates. The basis of the mechanism was postulated to be the competing osmotic and elastic contributions regarding the 'soft' character of the microgel particles. Owing to the organic side chains (hairy nature) of the microgel surface, the minimum in the potential energy has a restricted depth.[21] As a further approach, by combining DLS and Brownian dynamics simulation, they studied the heteroaggregation kinetics of two polymers with opposite charge densities. They observed faster diffusion aggregation in cases of high ionic concentrations and suggested reversibility was controlled by a secondary minimum aggregation. Multi-angle light scattering is very useful in enhancing the single-angle approach, especially in interpreting the kinetic interaction of dissimilar particles. This technique however is limited to particles of radii and refractive indices below certain critical values. In a review by Kim *et. al.*[22] the physical effects of changing temperature, ionic strength, pH and kinetic stimulation of the clusters in heteroaggregation were discussed in detailed.

Another approach to determine heteroaggreagtion of colloidal particles is turbidimetry. The changes in turbidity reflect changes in the system stability. Thus, the observed state of aggregation/stability is the result of a complex balance between diffusion effects (Brownian motion), repulsive and attractive and van der Waals forces. This also takes into account the influence of the environment of microgels, their relative concentrations, surface charge potential and charge density under a particular set of experimental conditions.[21]

Recently Snowden *et. al.*[21] determined the dispersibility (*n*) of a mixed anionic and cationic microgel system by setting a value (2) as an approximate boundary between dispersed and aggregated systems (Figure 1) at various pHs, temperatures and media which developed from previous experimental procedures.[23] They deduced that the relative effect of concentration could be used as a trigger for aggregation at a temperature under the volume phase transition temperature (VPTT). It was noted by varying pH that the charge density of the cationic microgels became a major factor in controlling the overall dispersity of the system. The limitation of this technique however arises when it is difficult to explain heteroaggregation, which is dependent on large relative size particles, charge density and also surface charge potentials.[21] Furthermore the results are somewhat inaccurate given the estimations and assumptions made.

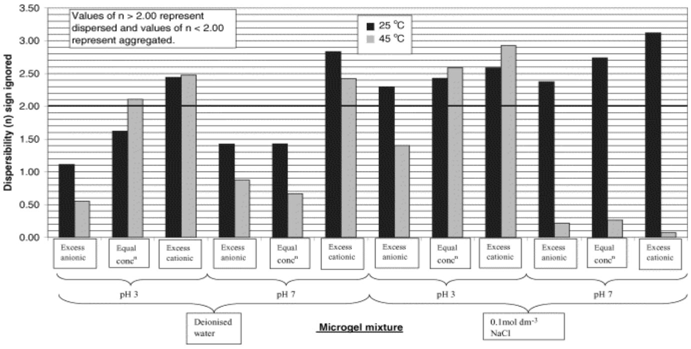

Figure 1: Visual representation of the dispersibility of microgel mixtures at different pH and temperature using turbidimetry.[21]

DOI: 10.17628/ecb.2012.1.130-134

Extensive experiments for microgels heteroaggregation

As ‘smart’ polymers, microgels respond to external stimuli such as temperature, pH and electrolytes. This section will discuss the effect of different postulate parameters that induce microgel polymers to undergo heteroaggregation.

Variable temperature

Usually, materials expand on heating owing to thermal energy increase. In contrast, this behaviour is not applicable to all polymers in aqueous solution. Islam *et. al.*[24] reported the interactions between a cationic microgel and anionic latex as a function of temperature and electrolyte presence at approximately equal particle concentration. Heteroaggregation occurs in mixed microgel systems when the temperature increases above the VPTT. At room

Adjustable pH

Preparation of pH responsive microgels usually comprises either acidic or basic monomers or incorporation with co-monomers. Such poly(vinylpyridine-costyrene)[28], poly(methyl methacrylate-co-methacrylic acid)[29], PNIPAM-co-4-vinylpyridine (P4VP)[21] are among pH responsive microgels with comonomers that have been commonly studied. In the case of microgel complexes, which exhibit thermoresponsive and pH responsive behaviour, the swelling properties of these microgels are strongly dominated by the distribution of the pH-sensitive co-monomers.[30]

This can be seen in a heteroaggregation study of mixed colloidal dispersions of anionic (PNIPAM) and cationic (PNIPAM-co-4VP) microgels reported by Snowden *et. al.*[21] at different relative concentrations. The authors obtained similar results at pH 3 and pH 7 where the system aggregated at equal +ve/-ve concentration. Furthermore, Stark *et. al.*[31] have reported encouraging results for reversible functionalized silica particles (PAA and PEO) triggered by pH. The authors reported that heteroflocculation occurred in the pH range 3.0 - 4.5 but beyond pH 5 the system re-dispersed (Figure 2). This supported their early hypotheses that heteroaggregation could be induced reversibly by changing the pH, which then alters the number of hydrogen bonds, thus controlling the interactions between different types of particles.

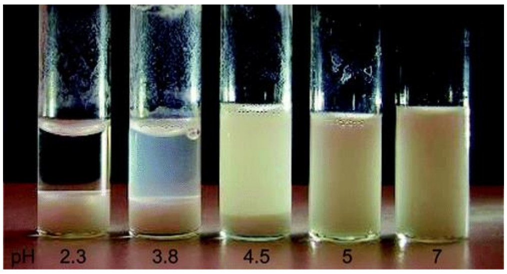

Figure 2: Photograph of heteroaggregation of PAA−PEO mixtures at changable pH.[31]

Another interesting demonstration of using pH-triggered formation of heteroaggregate gels prepared from mixed pigment/polystyrene (PS) dispersions was reported by Hui *et. al.*[32] They found that pigment/PS dispersions have two critical pH values (pH_{crit}) which were 1.9 and 3.45 respectively. At low pH, heteroaggregate particles gels are formed due to pH-triggered electrostatic attractions between oppositely charged particles. Therefore these findings provide some insight into the adjustable pH windows for transitions from liquid to gel forms for further applications.

Electrolytes

The surface charges for anionic/cationic microgel particles are associated with the initiator used in their preparation. The dispersions have been found to remain colloidally stable in electrolyte concentrations up to approximately 1.0 mol dm^{-3}.[21] Particles in the de-swollen state are electrostatically stabilized against aggregation, can however undergo aggregation when sufficient electrolyte is added due to interparticle van der Waals attractions. When they swell, the influx of solvent increases and hence reduces the van der Waals attraction between the particles: at high enough salt concentrations, swollen microgel particles eventually become stable to aggregation. For swollen particles, the van der Waals attraction is eliminated as the particles are predominantly water and as such the Hamaker constant is equivalent to the surrounding fluid. In contrast, for oppositely charged mixtures, the swollen microgel particles will possibly undergo heteroaggregation, although the electrolyte concentration is low with regard to inter particle electrostatic attractions.[32,33]

Using multi-angle SLS and DLS, Lin *et. al.*[13] studied the heteroaggregation rate constants as a function of ionic strength. Results showed that the heteroaggregation rate constants slowly increased with a decrease in ionic strength. This behaviour was explained using a model based on DLVO theory. In other work, DLS was used by Puertas *et. al.*[19,20] to study the critical coagulation concentration (C.C.C.) at different electrolyte concentrations, a parameter which influences heteroaggregation between oppositely charged colloidal particles. A very low electrolyte concentrations produced extremely fast aggregation and simultaneously the rate constant decreased sharply. However, it was noted that the diffusion controlled kinetics value was reached only above the C.C.C.

The fractal dimension of heteroaggregates produced from oppositely charged or similarly sized particles can be controlled by electrolyte concentration, which alters the range of electrostatic interactions between particles. Experimentally, the time evolution of the size, structure and porosity of oppositely charged colloids has been investigated by Snowswell *et. al.*[34] By adjusting the electrolyte concentrations, they were able to control the aggregation time, giving a series of desired pore sizes and morphologies.

Applications of microgels undergoing heteroaggregation

There are many important processes, which are controlled by heteroaggregation. Paper making is a classic example whereby the final product is produced from initial slurry through the heteroaggregation of cellulose fibers and filler particles. The aggregate formation in flotation processes and water purification[35] also utilizes the principles of heteroaggregation. Using modified responsive polystyrene latex, easy to use pregnancy test kits have been developed. The probe was built based on heteroaggregation of human chorionic gonadotropin (HCG) that has been successfully incorporated with polystyrene latex.[36]

In early ceramic processing colloidal clays and animal dung were used as aids. To date, due to their intrinsic chemical and physical characteristics, microgels have been used as alternative aids in modern ceramic processing. When heated, heteroaggregation occurs in the system and the aggregates remain in the ceramic body, forming bridges which result in much stronger adhesion after evaporation of the solvent.[8,25] Microgels have also been successfully exploited in oil recovery.[21] Due to the thermosensitivity of poly(N-isopropylacrylamide) (PNIPAM), these microgels have been designed to enhance the efficiency of crude oil recovery. The systems exist as stable dispersions under the VPTT however flocculate once injected into the ground. This is achieved due to the acute response to the high temperatures prevalent in oil-bearing rock (above VPTT) and the presence of highly concentrated electrolyte in the pumping material, e.g. seawater. Figure 3 shows the schematic process of oil recovery by manipulating heteroaggregation. Microgel aggregation can consequently block off channels of high permeability, thus enabling the oil in the less permeable areas to be mobilised. This process however depends on the strength of the aggregates, which must bear huge shear forces resulting from the high pressure. Therefore mixed charge microgel particles are the best choice to demonstrate stronger and more robust heteroaggregation characteristics compared to homoaggregated systems.

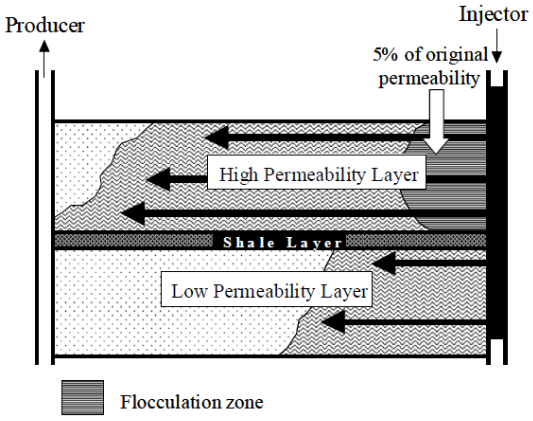

Figure 3: Schematic showing how microgels may be used to block a portion of high permeability rock therefore forcing a greater amount of the injected water through the low permeability layer which in turn forces out more oil.[21]

Conclusions

This review has discussed the versatility of microgel heteroaggregation, which is much richer from a conceptual point of view because of the inherent asymmetry originating from the two surfaces of the different particles. Heteroaggregation occurs when there is an attractive interaction between oppositely charged particles in mixed dispersions. Although the heteroaggregation process is more complicated compared to homoaggregating dispersions, a substantial understanding of colloidal interactions in these systems has emerged and been developed. There are many strategies for designing and preparing multifunctional microgel systems that can be employed to control the outcomes by manipulating responses to external stimuli.

Heteroaggregation of colloidal microgels has mainly been studied as a function of temperature, pH and electrolyte concentration. Therefore, for each kind of stimulus involved, procedures including physical and chemical methods that led to heteroaggregation have been discussed respectively. It has been shown that heteroaggregation in systems of variable charge and charge density are also heavily influenced by a complex balance of forces, both electrostatic and steric, and can be affected significantly by the environment of the particles. Aggregation under various conditions of pH, electrolyte, temperature, charge density and relative concentration can be induced by the careful manipulation of any one or more of these environmental conditions. Furthermore, aggregation of these systems can be controlled to drive towards a system of permanent coagulation or flocculation using one or more stimuli. The separate phases from destabilised systems can then be easily filtered. This is potentially useful as physico-chemical properties can be manipulated to generate a multifunctional system for dispersion and separation purposes.

The flexibility offered by oppositely charged microgels and their heteroaggregation have numerous advantages. The underlying principles shown here rely on strong surface interactions which can be altered and monitored. This holds much promise for new developments in many areas such as oil recovery, reusable high precious nanometals and its recovery, biomedical, chemical separations and purifications and catalysis. Functionalization of these frameworks via impregnation of active components and structure can create highly structured systems with controllable properties.

Acknowledgements

The author would like to thanks the Ministry of Higher Education of Malaysian for FRGS grant FRGS/1/2011/SG/UKM/02/25 and Universiti Kebangsaan Malaysia for grants UKM-GGPM-NBT-030-2011.

References

[1] Myakonkaya, O.; Eastoe, J. *Adv. Colloid Interface Sci.* 2009, *149*, 39.

[2] Hollamby, M. J.; Eastoe, J.; Chemelli, A.; Glatter, O.; Rogers, S.; Heenan, R. K.; Grillo, I. *Langmuir* **2010**, *26*, 6989.

[3] Hoare, T.; Pelton, R. *Macromolecules* 2007, *40*, 670.

[4] Oh, J. K.; Drumright, R.; Siegwart, D. J.; Matyjaszewski, K. *Prog. Polym.Sci.* **2008**, *33*, 448.

[5] Mei, Y.; Lu, Y.; Polzer, F.; Ballauff, M.; Drechsler, M. *Chem. Mater.* **2007**, *19*, 1062.

[6] Abd El-Rehim, H. A. *Radiat. Phys. and Chem.* **2005**, *74*, 111.

[7] Bergström, L. *Adv. Colloid Interface Sci.***1997**, *70*, 125-169.

[8] Islam, A. M.; Chowdhry, B. Z.; Snowden, M. J. *Adv. Colloid Interface Sci.* **1995**, *62*, 109.

[9] Derjaguin, B. V. *Discuss. Faraday Soc.* **1954**, *18*, 85.

[10] Hogg, T. W. *Trans. Faraday Soc.* **1966**, *62*, 1638.

DOI: 10.17628/ecb.2012.1.130-134

[11] Puertas, A. M.; Fernández-Barbero, A.; de las Nieves, F. J. *Physica A* **2002**, *304*, 340.

[12] Elimelech, M. *J. Colloid Interface Sci.* **1991**, *146*, 337-352.

[13] Lin, W.; Kobayashi, M.; Skarba, M.; Mu, C.; Galletto, P.; Borkovec, M. *Langmuir* **2005**, *22*, 1038.

[14] Grolimund, D.; Elimelech, M.; Borkovec, M.; Barmettler, K.; Kretzschmar, R.; Sticher, H. *Environ.Sci. Technol.***1998**, *32*, 3562.

[15] Yang, J.; Bos, R.; Poortinga, A.; Wit, P. J.; Belder, G. F.; Busscher, H. J. *Langmuir* **1999**, *15*, 4671.

[16] Böhmer, M. R.; van der Zeeuw, E. A.; Koper, G. J. M. *J. Colloid Interface Sci.***1998**, *197*, 242.

[17] Galletto, P.; Lin, W.; Borkovec, M. *Phys. Chem. Chem. Phys.***2005**, *7*, 1464.

[18] Matijevic, N. R. *J. Chem. Soc. Faraday Trans* **1994**, *90*, 167.

[19] Fernandez-Barbero, A.; Vincent, B. *Phys. Rev. E* **2000**, *63*, 011509.

[20] Fernandez-Nieves, A.; Fernandez-Barbero, A.; Vincent, B.; de las Nieves, F. J. *Langmuir* **2001**, *17*, 1841.

[21] Hall, R. J.; Pinkrah, V. T.; Chowdhry, B. Z.; Snowden, M. J. *Colloids Surf. A* **2004**, *233*, 25.

[22] Kim, A. Y.; Hauch, K. D.; Berg, J. C.; Martin, J. E.; Anderson, R. A. *J. Colloid Interface Sci.***2003**, *260*, 149.

[23] Long, J. A.; Osmond, D. W. J.; Vincent, B. *J. Colloid Interface Sci.***1973**, *42*, 545.

[24] Islam, A. M.; Chowdhry, B. Z.; Snowden, M. J. *J. Phys.Chem.***1995**, *99*, 14205.

[25] Greenwood, R.; Kendall, K.; Ritchie, S.; Snowden, M. J. *J. Eur. Ceram. Soc.* **2000**, *20*, 1707.

[26] Hui, D.; Morris, D.; Edwards, M.; Saunders, B. R. *J.Colloid Interface Sci.***2010**, *342*, 320.

[27] Hou, Y.; Ye, J.; Wei, X.; Zhang, G. *J. Phys. Chem. B* **2009**, *113*, 7457.

[28] Loxley, A.; Vincent, B. *Colloid Polym.Sci.***1997**, *275*, 1108.

[29] Saunders, B. R.; Crowther, H. M.; Vincent, B. *Macromolecules* **1997**, *30*, 482.

[30] Palioura, D.; Armes, S. P.; Anastasiadis, S. H.; Vamvakaki, M. *Langmuir* **2007**, *23*, 5761.

[31] Starck, P.; Ducker, W. A. *Langmuir* **2009**, *25*, 2114.

[32] Hui, D.; Nawaz, M.; Morris, D. P.; Edwards, M. R.; Saunders, B. R. *J.Colloid Interface Sci.* **2008**, *324*, 110.

[33] Routh, A. F.; Vincent, B. *J.Colloid Interface Sci.* **2004**, *273*, 435.

[34] Snoswell, D. R. E.; Rogers, T. J.; Howe, A. M.; Vincent, B. *Langmuir* **2005**, *21*, 11439.

[35] Buffle, J.; Wilkinson, K. J.; Stoll, S.; 899.Filella, M.; Zhang, J. *Environ. Sci.Technol.***1998**, *32*, 2887

[36] Ouali, L.; Pefferkorn, E.; Elaissari, A.; Pichot, C.; Mandrand, B. *J.Colloid Interface Sci.* **1995**, *171*, 276.

Received: 03.09.2012.

Accepted: 05.09.2012)

KINETICS AND MECHANISM OF THE OXIDATION OF SUBSTITUTED BENZALDEHYDES WITH BIS(PYRIDINE) SILVER PERMANGANATE

Jayshree Banerji,[a] László Kótai,[b] Pradeep K. Sharma,[c] and K.K. Banerji[d]*

Keywords: Permanganate, kinetics, correlation analysis, mechanism, oxidation

The oxidation of thirty-six *ortho-*, *meta-* and *para*-substituted benzaldehydes by bis(pyridine)silver permanganate (BPSP) resulted in the formation of the corresponding benzoic acids. The reaction is first order with respect to both BPSP and aldehydes. The reaction is catalyzed by hydrogen ions. The rate of reaction increases with an increase in the amount of acetic acid in the solvent. The correlation analyses of the rate of oxidation of thirty-six aldehydes were performed in terms of Charton’s LDR and LDRS equations. The rate of oxidation of *meta-* and *para*-substituted benzaldehydes showed excellent correlation with Charton's LDR equation. The rates of *ortho*-compounds showed excellent correlation with LDRS equation. The oxidation of *para*-compounds is more susceptible to the delocalization effect. The oxidation of *ortho-* and *meta*-compounds exhibited a greater dependence on the field effect. The polar reaction constants are negative indicating an electron-deficient centre in the rate-determining step. A mechanism involving a rate-determining hydride transfer from the aldehyde to the protonated BPSP has been proposed.

* Corresponding Authors
Fax: +91 291 2557540
E-Mail: banerjikk@gmail.com
[a] Department of Chemistry, RGP Mahavidyalaya, Kolar Road, Bhopal 462042, India ű
[b] Institute of Materials and Environmental Chemistry, Research Centre for Natural Sciences, Hungarian Academy of Sciences, H-1025, Pusztaszeri u. 59-67, Budapest, Hungary
[c] Department of Chemistry, J N V University, Jodhpur 342011, India
[d] Faculty of Science, National Law University, Mandore, Jodhpur 342304, India

1. Introduction

Bis(pyridine)silver permanganate (BPSP) is a mild and selective oxidizing agent. It is found to be better reagent than potassium permanganate in many reactions, e.g. oxidative alkylamination of electron-deficient (hetero) aromatic compounds.[1] We have reported its thermally induced intra-molecular redox reaction,[2] the oxidation of oxalic and formic acid[3] and of organic sulfides[4] with BPSP. The oxidation of aldehydes with BPSP has not been reported, therefore, we have undertaken this work.

2. Experimental Section

2.1 Materials

BPSP was prepared by reported method[5] and its purity was checked by iodometric method. The aldehydes were commercial products. The liquid aldehydes were purified through their bisulfite addition compounds and distilling them, under nitrogen, just before use.[6] The solid aldehydes were recrystallized from ethanol.

Deuteriated benzaldehyde (PhCDO) was also prepared by the literature method.[7] Its isotopic purity, as ascertained by its NMR spectrum, was 97±3%. Perchloric acid was used as a source of hydrogen ions. Acetic acid was refluxed with acetic anhydride and chromic oxide for 3 h and then distilled.

2.2 Product Analysis

The product analysis was carried out under kinetic conditions. In a typical experiment, freshly distilled benzaldehyde(0.05 mol) and BPSP (0.01 mol) were made up to 50 cm^3 in 1:1 acetic acid-water (v/v) and kept in the dark for *ca*. 10 h to ensure completion of the reaction. It was rendered alkaline with NaOH, filtered and filtrate evaporated to under reduced pressure. The residue was dissolved in minimum amount of concd. HCl and cooled in ice to yield crude acid (2 g), which was recrystallized from hot water to produce pure benzoic acid (1.9 g, 90%, m.p. 121^{o} C).

2.3 Kinetic Measurements

The reactions were studied under pseudo-first-order conditions by keeping a large excess of the aldehyde (× 15 or larger) over BPSP. The solvent was 1:1 (v/v) acetic acid-water, unless stated otherwise. The reactions were studied at constant temperature (±0.1 K) and followed up to 80% completion by monitoring the decrease in absorption due to BPSP at 529 nm. The pseudo-first-order constants, k_{obs}, were computed from the linear ($r > 0.990$) least-squares plots of log[BPSP] versus time plots. Duplicate kinetic runs showed that rate constants are reproducible within ±4%. Preliminary experiments showed that the oxidation is not sensitive to changes in ionic strength, therefore, no attempt was keep it constant.

DOI: 10.17628/ecb.2012.1.135-140

3. Results and Discussion

The rate laws and other data were obtained for all compounds investigated. Since the results are similar only representative data are reproduced here.

3.1 Stoichiometry

The oxidation of aromatic aldehydes resulted in the formation of corresponding benzoic acid (1)

$$ArCHO + 2Mn^{VII} + 3H_2O \rightarrow ArCO_2H + 2Mn^{IV} + 6H^+ \quad (1)$$

Thus BPSP is reduced to Mn(IV). To confirm that Mn(IV) is indeed formed as a result of reduction of BPSP by aldehydes, the rate were determined by monitoring the increase in [Mn(IV)] at 418 nm also.[8,9] The rates of decay at 529 nm and increase at 418 nm agreed within ±7%. BPSP has virtually no absorption at 418 nm. This agrees with the observations of earlier workers.[8,9]

3.2 Rate Laws

The reactions are first order with respect to BPSP. Further, the values of k_{obs}, are independent of initial concentration of BPSP. The reaction rate increases linearly with an increase in the concentration of aldehydes showing that the reaction is first order with respect to aldehydes also. The rate of oxidation increases linearly with an increase in the acidity of the solution (Table 1).

Table 1. Rate constants for the oxidation of benzaldehyde by BPSP at 298 K

10^3[BPSP] mol dm^{-3}	**[Aldehyde]** mol dm^{-3}	**[H$^+$]** mol dm^{-3}	**10^4 k_{obs}** s^{-1}
1.0	0.10	1.0	2.33
1.0	0.20	1.0	4.62
1.0	0.40	1.0	9.36
1.0	0.60	1.0	14.0
1.0	0.80	1.0	18.2
1.0	1.00	1.0	23.3
1.0	2.00	1.0	46.7
2.0	0.40	1.0	9.36
4.0	0.40	1.0	9.56
6.0	0.40	1.0	9.12
8.0	0.40	1.0	9.61
1.0	1.00	0.2	4.70
1.0	1.00	0.4	9.32
1.0	1.00	0.6	14.1
1.0	1.00	0.8	18.7
1.0	0.40	1.0	9.54*

*contained 0.001 mol dm^{-3} acrylonitrile

3.3 Test for free radicals

The oxidation of benzaldehyde, in an atmosphere of nitrogen, failed to induce polymerization of acrylonitrile. In blank experiments, with the aldehyde absent, no noticeable consumption of BPSP was observed. The addition of acrylonitrile had no effect on the reaction rate (Table 1). To further confirm the absence of free radicals in the reaction pathway, the reaction was carried out in the presence of 0.05 mol dm^{-3} of 2,6-di-*t*-butyl-4-methylphenol (butylated hydroxytoluene or BHT). It was found that BHT was recovered unchanged almost quantitatively.

3.4 Effect of Substituents

The rates of oxidation of a number of *ortho*-, *meta*- and *para*-substituted benzaldehydes were determined at different temperatures and the activation parameters were calculated (Table 2).

3.5 Kinetic Isotope Effect

To ascertain the importance of the cleavage of the aldehydic C – H bond in the rate-determining step, the oxidation of [^{2}H]benzaldehyde (PhCDO) was studied. The results (k_H/k_D = 5.66 at 298 K) showed the presence of a substantial primary kinetic effect (Table 2).

3.6 Effect of Solvent Composition

The rate of oxidation of was determined in solutions containing different amounts of acetic acid and water. It was observed that the rate of oxidation increased with an increase in the amount of acetic acid in the solvent (Table 3). The rate of oxidation increases with an increase in the amount of acetic acid in the solvent. This may be attributed to the change in the acidity of the medium with a change in the amount of acetic acid. Hammett's acidity function, H_0, for low concentration of perchloric acid in a series of acetic acid-water mixtures has been determined.[10] It is observed that the acidity increases as the concentration of acetic acid increases. The present reaction is an acid-catalyzed one and with an increase in the acidity of the solution, the rate is expected to increase.

3.7 Correlation Analysis of Reactivity

The correlation between the activation enthalpies and entropies of the oxidation of the thirty-six aldehydes is just satisfactory (r^2 = 0.9132), indicating the presence of a weak compensation effect.[11] However, a correlation between the calculated values of enthalpies and entropies is often vitiated by the experimental errors associated with them. The reaction exhibited an excellent isokinetic relationship, as determined by Exner's method.[12] An Exner's plot between log k_2 at 288 K and at 318 K was linear (r^2 = 0.9970, slope = 0.8350 ± 0.0078). The value of isokinetic temperature evaluated from the Exner's plot is 469±27 K. The linear isokinetic correlation implies that all the aldehydes are oxidized by the same mechanism and the change in the rate of oxidation is governed by changes in both the enthalpy and entropy of the activation.

The rate constants for the oxidation of *meta*- and *para*-substituted benzaldehydes were correlated in terms of Hammett equation[13] but no significant correlation was obtained (Eqn. 2).

DOI: 10.17628/ecb.2012.1.135-140

Table 2 Rate constants and activation parameters of the oxidation of substituted benzaldehydes by BPSP

Substrate	**10^4 k_2 (dm^3 mol^{-1} s^{-1})**				**Δ H***	**Δ S***	**Δ G***
	288K	298K	308K	318K	kJ mol^{-1}	J mol^{-1} K^{-1}	kJ mol^{-1}
H	8.80	23.3	57.6	139	67.3±0.3	−70 ± 1	88.0±0.2
p-Me	18.5	47.0	113	252	63.8±0.1	−76 ± 1	86.3±0.1
p-OMe	43.0	105	234	556	62.0±0.9	−75 ± 3	84.3±0.7
p-F	10.6	28.8	72.0	176	68.6±0.3	−63 ± 1	87.5±0.2
p-Cl	6.51	18.0	46.1	114	70.0±0.1	−63 ± 1	88.7±012
p-NO$_2$	0.52	1.71	4.90	14.0	80.7±0.5	−47 ± 2	94.5±0.4
p-CF$_3$	1.36	4.02	12.1	31.1	77.4±0.6	−51 ± 2	92.3±0.5
p-CO$_2$Me	2.00	5.35	14.6	37.3	71.9±0.8	−67 ± 3	91.6±0.6
p-Br	6.32	17.5	44.6	112	70.3±0.3	−63 ± 1	88.8±0.3
p-NHAc	22.0	52.5	127	290	63.0±0.5	−77 ± 2	85.9±0.5
p-CN	0.90	2.81	8.00	21.4	77.8±0.1	−52 ± 1	93.3±0.1
p-SMe	25.0	62.7	149	340	63.7±0.2	−74 ± 1	85.5±0.2
p-NMe$_2$	178	412	843	1770	55.4±0.5	−86 ± 2	80.9±0.4
m-Me	17.7	40.0	97.0	220	61.7±0.5	−84 ± 3	86.5±0.6
m-OMe	16.5	41.5	98.3	224	63.6±0.2	−78 ± 1	86.6±0.2
m-Cl	2.70	7.41	19.9	46.3	69.9±0.5	−71 ± 2	90.8±0.4
m-Br	2.68	7.28	18.5	46.6	69.8±0.4	−71 ± 1	90.9±0.3
m-F	3.35	0.07	23.4	54.1	68.3±0.4	−75 ± 1	90.4±0.3
m-NO$_2$	0.30	0.91	2.53	7.05	77.4±0.5	−63 ± 2	96.1±0.4
m-CO$_2$Me	1.45	4.25	11.3	28.9	72.3±0.2	−64 ± 1	92.3±0.2
m-CF$_3$	1.02	2.90	8.66	21.7	75.6±0.8	−59 ± 3	93.1±0.6
m-CN	0.52	1.53	4.30	11.9	76.8±0.6	−61 ± 2	94.7±0.4
m-SMe	11.4	29.0	66.6	145	61.9±0.4	−86 ± 1	87.5±0.3
m-NHAc	9.92	25.0	63.1	142	65.3±0.4	−76 ± 2	87.8±0.3
o-Me	80.0	182	400	812	56.4±0.2	−89 ± 1	82.9±0.2
o-OMe	75.7	176	380	798	57.1±0.1	−87 ± 1	83.0±0.1
o-NO$_2$	1.00	2.74	7.41	19.8	73.2±0.7	−68 ± 3	93.3±0.7
o-CO$_2$Me	6.60	17.2	41.0	98.7	65.9±0.5	−77 ± 2	88.8±0.4
o-NHAc	112	252	520	1060	54.3±0.2	−94 ± 1	82.1±0.2
o-Cl	19.2	46.7	107	233	60.8±0.1	−86 ± 1	86.2±0.1
o-Br	25.4	61.6	137	308	60.6±0.4	−85 ± 1	85.6±0.3
o-I	43.0	98.6	214	445	56.8±0.1	−93 ± 1	84.5±0.1
o-CN	1.96	5.44	14.0	35.9	71.1±0.5	−69 ± 1	91.6±0.4
o-SMe	108	240	490	1000	53.8±0.3	−96 ± 1	82.3±0.2
o-F	13.0	30.8	72.5	170	62.7±0.8	−83 ± 3	87.3±0.6
o-CF$_3$	15.0	36.1	82.6	184	61.0±0.2	−87 ± 1	86.9±0.2
PhCDO	1.51	4.12	10.6	26.3	69.9±0.2	−76 ± 1	92.3±0.2
k_H/k_D	5.83	5.66	5.43	5.29			

Table 3. Effect of Solvent Composition on the Reaction Rate
[BPSP] 0.001 mol dm^{-3} [PhCHO] 0.60 mol dm^{-3} [H$^+$] 1.0 mol dm^{-3} T = 298 K

% Acetic acid (v/v)	20	30	50	60	70
10^4 k_{obs} (s^{-1})	5.76	10.5	14.0	24.6	38.0

DOI: 10.17628/ecb.2012.1.135-140

$$\log k_2 = -1.77 \pm 0.14\sigma - 2.51 \qquad (2)$$

$r^2 = 0.8778$, sd = 0.24, $n = 24$, $T = 298$ K

It has been stated[14] that in the absence of proximity effects, the polar effects of *ortho*-substituents parallel those of *para*-substituents. In this case, however, the rate constants of *ortho*- and *para*-substituted benzaldehydes are not linearly related (Eqn. 3). This indicates that the polar effects are not solely responsible for the observed effect of *ortho*-substituents on this reaction.

$$\log k_{\text{ortho}} = 0.91 \pm 0.16 \log_{\text{para}} - 3.42 \qquad (3)$$

$r^2 = 0.7733$, sd = 0.33, $n = 11$, $T = 298$ K

There have been many attempts to describe a single substituent-parameter equation for *ortho*-substituents. Charton[14] has compiled a list 32 sets of such constant. We analyzed the rate constants of the *ortho*-compounds in terms of *ortho*-substituent constant, σ_o, of Tribble and Traynham[15] which has the biggest set of data, but the correlation is unsatisfactory (Eqn. 4).

$$\log k_2 = -\,0.78 \pm 0.22\, \sigma_o - 2.99 \qquad (4)$$

$r^2 = 0.5723$, sd = 0.52, $n = 11$, $T = 298$ K

The data for *o*-NO_2 and *o*-SMe were not included in this correlation as the σ_o values are not available.

Since the rate constants failed to yield satisfactory correlation with any single substituent-parameter equation, the rates were analyzed in terms of Taft's[16] and Swain-Lupton's [17] dual substituent-parameter equations. However, no satisfactory correlation was obtained in of these equations also. In the late 1980s, Charton [18] introduced a triparametric LDR equation for the quantitative description of structural effects on chemical reactivities. In this work we have applied the LDR equation (5) to the rate constants, k_2.

$$\log k_2 = L\,\sigma_l + D\,\sigma_d + R\,\sigma_e + h \qquad (5)$$

Here, σ_l is a localized (field and/or inductive) effect parameter, σ_d is the intrinsic delocalized electrical effect parameter when the active site electronic demand is minimal and σ_e represents the sensitivity of the substituent to changes in electronic demand by the active site. The latter two substituent parameters are related by equation (6)

$$\sigma_D = \eta\sigma_e + \sigma_d \qquad (6)$$

Here η represents the electronic demand of the reaction site and is given by $\eta = R/D$, and σ_D represents the delocalized electrical parameter of the diparametric LD equation.

For *ortho*-substituted compounds, it is necessary to account for the possibility of steric effects and Charton,[18] therefore, modified the LDR equation to generate the LDRS equation (7).

$$\log k_2 = L\,\sigma_l + D\,\sigma_d + R\,\sigma_e + S\,\nu + h \qquad (7)$$

where ν is the well known Charton's steric parameter based on Van der Waals radii.[19]

The rates of oxidation of *ortho*-, *meta*- and *para*-substituted benzaldehydes show an excellent correlation in terms of the LDR/LDRS equations (Table 4). We have used the standard deviation (sd), the coefficient of multiple determination (R^2), and Exner's parameter,[20] ψ, as the measures of goodness of fit.

The comparison of the *L* and *D* values for the substituted benzaldehydes showed that the oxidation of *para*-substituted benzaldehydes is more susceptible to the delocalization effect than to the localized effect. However, the oxidation of *ortho*- and *meta*-substituted compounds exhibited a greater dependence on the field effect. In all cases, the magnitude of the reaction constants decreases with an increase in the temperature, pointing to a decrease in selectivity with an increase in temperature.

All three regression coefficients, *L*, *D* and *R*, are negative indicating an electron-deficient carbon centre in the activated complex for the rate-determining step. The positive value of η adds a negative increment to σ_d, increasing the electron-donating power of the substituent and its capacity to stabilize a cationic species. The positive value of *S* indicates that the reaction is subject to steric acceleration by an *ortho*-substituent.

To test the significance of localized, delocalized and steric effects in the ortho-substituted benzaldehydes, multiple regression analyses were carried out with (i) σ_l, σ_d and σ_e (ii) σ_d, σ_e and υ and (iii) σ_l, σ_e and υ. The absence of significant correlations showed that all the four substituent constants are significant.

$$\log k_2 = -1.47\,(\pm 0.43)\sigma_l - 1.69\,(\pm 0.34)\sigma_d - 3.51\,(\pm 1.95)\sigma_e - 2.24 \qquad (8)$$

$R^2 = 0.8268$; sd = 0.30; $n = 13$; $\psi = 0.47$

$$\log k_2 = -1.78\,(\pm 0.44)\sigma_d - 1.80\,(\pm 2.72)\sigma_e + 0.89\,(\pm 0.50)\upsilon - 3.16 \qquad (9)$$

$R^2 = 0.7042$; sd = 0.39; $n = 13$; $\psi = 0.62$

$$\log k_2 = -1.95\,(\pm 0.69)\sigma_l - 0.41(\pm 3.30)\,\sigma_e + 1.31\,(\pm 0.62)\upsilon - 2.32 \qquad (10)$$

$R^2 = 0.5635$; sd = 0.47; $n = 13$; $\psi = 0.75$

Similarly in the cases of the oxidation of para- and meta-substituted benzaldehydes, multiple regression analyses indicated that both localization and delocalization effects are significant. There is no significant collinearity between the various substituents constants for the three series.

DOI: 10.17628/ecb.2012.1.135-140

Table 4. Temperature dependence for the reaction constants for the oxidation of substituted benzaldehydes by BPSP

T/K	L	D	R	S	η	R^2	sd	ψ	P_D	P_S
Para-substituted										
288	−1.47	−1.90	−1.25	-	0.66	0.9996	0.016	0.02	56.4	-
298	−1.35	−1.82	−1.16	-	0.64	0.9998	0.009	0.01	57.4	-
308	−1.26	−1.70	−1.06	-	0.68	0.9998	0.008	0.01	57.4	-
318	−1.16	−1.62	−0.98	-	0.60	0.9999	0.004	0.01	58.3	-
Meta-substituted										
288	−1.99	−1.42	−1.16	-	0.82	0.9995	0.015	0.03	41.6	-
298	−1.87	−1.35	−1.11	-	0.82	0.9999	0.007	0.01	41.9	-
308	−1.79	−1.27	−0.90	-	0.71	0.9995	0.014	0.03	41.5	-
318	−1.71	−1.16	−0.84	-	0.72	0.9995	0.013	0.03	40.6	-
Ortho-substituted										
288	−1.77	−1.71	−1.24	1.25	0.73	0.9998	0.011	0.02	49.1	26.4
298	−1.71	−1.62	−1.25	1.17	0.77	0.9999	0.003	0.01	48.6	26.0
308	−1.63	−1.53	−1.13	1.09	0.74	0.9999	0.006	0.01	48.4	25.7
318	−1.53	−1.43	−1.09	0.99	0.76	0.9998	0.008	0.02	48.3	25.1

The percent contribution[18] of the delocalized effect, P_D, is given by following equation (11).

$$P_D = (|D| \times 100) / (|L| + |D|) \tag{11}$$

Similarly, the percent contribution[18] of the steric parameter to the total effect of the substituent, P_S, was determined by using equation(12).

$$P_S = (|S| \times 100) / (|L| + |D| + |S|) \tag{12}$$

The values of P_D and P_S are also recorded in Table 4. The value of P_D for the oxidation of *para*-substituted benzaldehydes is *ca.* 57% whereas the corresponding values for the *meta-* and *ortho*-sobstituted aldehydes are *ca.* 42 and 48% respectively. This shows that the balance of localization and delocalization effects is different for differently substituted benzaldehydes. The less pronounced resonance effect from the *ortho*-position than from the *para*-position may be due to the twisting away of the aldehydic group from the plane of the benzene ring.

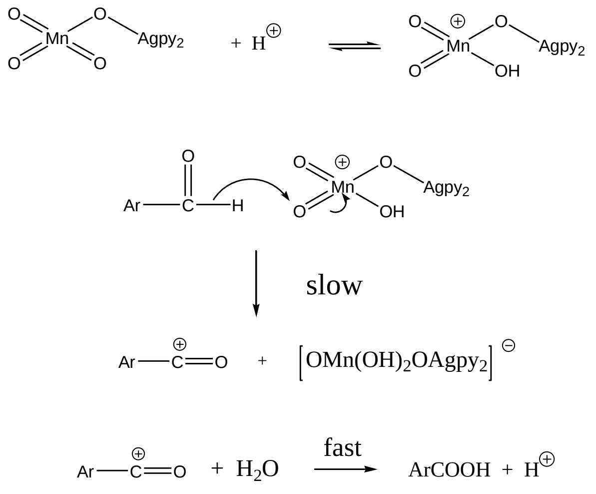

Scheme 1

The magnitude of the P_S value shows that the steric effect is significant in this reaction.

3.8 Mechanism

A hydrogen abstraction mechanism leading to the formation of the free radicals is unlikely in view of the failure to induce polymerization of acrylonitrile and no effect of the radical scavenger on the reaction rate. The presence of a substantial kinetic isotope effect confirms the cleavage of the aldehydic C-H bond in the rate determining step. The linear increase in the rate with acidity indicates (a) presence of a protonation pre-equilibrium, (b) that the protonation constant is small and (c) the protonation is not complete within the acid range studied and (d) only the protonation species is reactive. This suggests the presence of a pre-equilibrium protonation of BPSP to yield a better oxidant and electrophile.

$$[Agpy_2]MnO_4 + H^+ \leftrightarrows [Agpy_2Mn(OH)O_3]^+$$

The negative values of the localization and delocalization electrical effects i.e. of L, D and R points to an electron-deficient reaction centre in the rate-determining step. It is further supported by the positive value of η, which indicates that the substituent is better able to stabilize a cationic or electron-deficient reactive site. Therefore, a hydride-ion transfer in the rate-determining step is suggested. The benzoyl cation is reported to have a considerable keten character.[21] The linear structure of the acylium cation has also been confirmed by X-ray crystallography.[22] The change from sp^2 to *sp* hybridization results in steric relief. This relief is greater in crowded reductants and is reflected in the observed steric acceleration. The observed negative value of entropy of activation also supports the proposed mechanism. As the charge separation takes place in the transition state, the charged ends become highly solvated. This results in an immobilization of a large number of solvent molecules, reflected in the loss of entropy.[23]

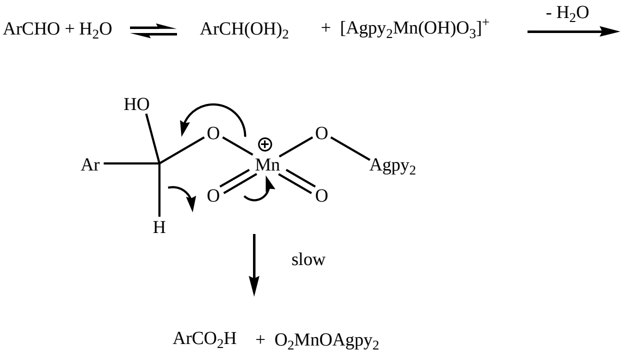

Scheme 2

An alternative mechanism involving a rapid ester formation between the aldehyde hydrate and protonated BPSP (Scheme 2) is also possible. The reaction involving *gem*-diol form, as shown, is likely to be a low-energy pathway as compared to that in Scheme 1. However, the value of hydration constant of benzaldehyde[24] at 298 K is 1.1 x 10^{-2}. Benzaldehyde, therefore, hydrated to an extent of *ca.*1% in solution. In view of this, the involvement of the hydrated form is less likely. Further, a non-linear transition state, implied in the ester mechanism is likely to result in a lower kinetic isotope effect than observed.

References

[1] Verbeeck, S., Herrebout, W. A., Gulevskaya, A. V., van der Veken, B. J., Maes, B. U. W. *J. Org. Chem.*, **2010**, *75*, 5126.

[2] Kotai, L., Fodor, J., Jakab, E., Sajo, I., Szabo, P., Lonvi, F., Valyon, J., Gacs, I., Argay, G., Banerji, K. K. *Transition Met. Chem.*, **2006**, *31*, 30.

[3] Banerji, J., Kotai, L., Banerji, K. K. *Indian J. Chem.*, **2009**, *48A*, 797.

[4] Banerji, J., Banerji, K. K., Kotai, L., Sharma, D., Sharma, P. K. *J. Indian Chem. Soc.*, **2011**, *88*, 1879.

[5] Kotai, L., Sajo, I., Fodor, J., Szabo, P., Jakab, E., Argay, G., Holly, S., Gacs, I., Banerji, K. K. *Transition Met Chem* **2005**, *30*, 939.

[6] Kalpan,J. *J. Am. Chem. Soc.*, **1958**, *80*, 2639.

[7] Wiberg, K. B. *J. Am. Chem. Soc.*, **1954**, *76*, 5871.

[8] Lee, D. G., Perez-Benito, J. F. *J. Org. Chem.*, **1988**, *53*, 5725.

[9] Freeman, F., Kappos, J. C. *J. Am. Chem. Soc.*, **1985**, *107*, 6628.

[10] Wiberg, K. B., Evans, D. *J. Am. Chem. Soc.*, **1958**, *80*, 3019.

[11] Liu, L., Guo, Q-X. *Chem. Rev.*, **2001**, *101*, 673.

[12] Exner, O. *Collect. Chem. Czech. Commun.*, **1964**, *29*, 1094; **1964**, *29*, 1094.

[13] Johnson, C. D. *The Hammett equation*, University Press, Cambridge, **1973**, 78.

[14] Charton, M. *J. Am. Chem. Soc.*, 1969, **91**, 6649.

[15] Tribble, M. T., Traynham, J. G. *J. Am. Chem. Soc.*, **1969**, *91*, 379.

[16] Dayal, S.K., Ehrenson, S., Taft, R.W. *J. Am.. Chem. Soc.*, **1974**, ***94***, 9113.

[17] Swain, C.G., Unger, S.H., Rosenquest, N.R., Swain, M.S. *J. Am. Chem. Soc.*, **1983**, *105*, 492

[18] Charton, M., Charton, B. *Bull. Soc. Chim. Fr.*, **1988**, 199 and references cited therein.

[19] Charton, M. *J. Org. Chem.*, **1975**, *40*, 407.

[20] Exner, O. *Collect. Chem. Czech. Commun.*, **1966**, *31*, 3222.

[21] Olah, G. A., Westermann, P. W. *J. Am. Chem. Soc.*, **1973**, *95*, 3706.

[22] Boer, F. P. *J. Am. Chem. Soc.*, **1968,** *90*, 6706.

[23] Gould, E. S. *Mechanism and Structure in Organic Chemistry*, Holt, Rinehart & Winston Inc., New York, **1964**, 178.

[24] Greenzaid, P. J. *J. Org. Chem.*, **1973**, *38*, 3164.

Received: 31.08.2012.

Accepted: 06.09.2012

PROPERTIES OF WATER/SODIUM DODECYL SULFATE/N-PROPANOL/ALLYLBENZENE MICELLAR SYSTEMS

Monzer Fanun[a]*, Ahmad Shakarnah[a], Oday Mustafa[a], Michael Schwarze[b], Reinhard Schomäcker[b], Jochanan Blum[c]

Keywords: phase behavior, ultrasonic velocity, density, isentropic compressibility, hydrodynamic diameter

Water/n-propanol/sodium dodecyl sulfate/allylbenzene micellar systems were formulated. The ratio (w/w) of n-propanol/surfactant equals 2/1. The extent of the micellar region as function of temperature was determined. The micellar systems were characterized by the volumetric parameters, density, excess volume, ultrasonic velocity and isentropic compressibility. The micellar densities increase with the increase in the water volume fraction. Excess volumes of the sodium dodecyl sulfate decrease for water volume fraction below 0.3, stabilize for water volume fractions between 0.2 and 0.5 then increase for water volume fraction above 0.5. Excess volumes of the studied micellar systems increase with temperature. Ultrasonic velocities increase with the increase in water volume fraction up to 0.8 then decrease. Ultrasonic velocities increase with temperature for water volume fractions below 0.8 and increase for water volume fractions above 0.8. Isentropic compressibilities decrease with the water volume fraction up to 0.8 then increase. Isentropic compressibilities increase with temperature for water volume fractions below 0.8 and decrease for water volume fractions above 0.8. Structural transitions from water-in-oil to bicontineous to oil-in-water occur along the micellar phase. The particle hydrodynamic diameter of the oil-in-water micellar systems was found to decrease with temperature. In the diluted region nanoemulsion systems were observed.

Corresponding Author
Tel: + 972 5 22 40 60 61;
Fax: + 972 22 79 69 60
E-Mail: Fanunm@gmail.com,
mfanun@ science. alquds.edu
[a] Colloids and Surfaces Research Center, Al-Quds University, East Jerusalem 51000, Palestine
[b] Institut für Chemie, Technische Universität Berlin, Strasse des 17. Juni 124, D-10623 Berlin, Germany
[c] Institute of Chemistry, The Hebrew University of Jerusalem, Jerusalem 91904, Israel

Introduction

Nanoemulsions are transparent or translucent systems that have a dispersed phase with a droplet size range of typically 20 to 500 nm. Nanoemulsions are thermodynamically unstable dispersions, of oil and water stabilized with the help of surfactant and co-surfactant.[1]-[4] Despite their metastability, nanoemulsions can persist over many months or years due to the presence of stabilizing surfactant micelles. The small droplet size, high kinetic stability and optical transparency of nanoemulsions compared to conventional emulsions, give them advantages for their use in many technological applications.[5]-[7] Nanoemulsions are increasingly proposed for use in the chemical industries in organic synthesis as alternatives to organic solvents. Double bond isomerization in alkenes is widely observed in industrial processes such as those associated with petrochemical oil refining steps. Owing to the hydrophobic nature of most alkenes, these reactions are usually carried out in organic solvents under homogeneous conditions. The public concern about the negative effect of the organic compounds on the environment[8] picked the interest of many researchers for replacement of the harmful media by water.[9] However, the application of aqueous systems arises a major problem of the insolubility of most organic reagents in water. Consequently, we developed a water-rich system that overcomes this discrepancy. This system relies on the use of an aqueous nanoemulsions of the substrates and uses a heterogenized organometallic complex that can be recovered by simple filtration as catalyst.[10] We termed the catalyses by this system an emulsion-solid transport process (EST) and demonstrated its utility in catalytic C-C bond coupling reactions[11] as well as in several hydrogen transfer operations such as double bond migration of hydrophobic allylic substrates in water.[12] In order to achieve high efficiency in the EST reactions it is essential to characterize the nature of the microemulsions and formulate them accordingly. We now have characterized the nanoemulsions formed from allylbenzene, n-propanol and aqueous sodium dodecyl sulfate that serves as a model medium in the isomerization of water insoluble allylarenes by recyclable sol gel immobilized late transition metal catalysts shown in Scheme 1.

Experimental

Materials

Allylbenzene (ALB) and n-propanol were purchased from from Sigma-Aldrich Chemical Company. Sodium dodecyl sulfate (SDS) was purchased from Ridel de Haën. All the components were used as supplied without further purification. Triply distilled water was used for all experiments.

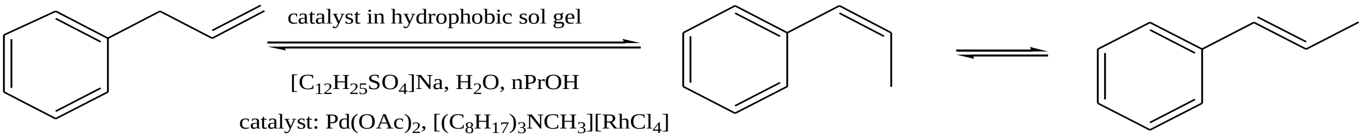

Scheme 1. Isomerization of water insoluble allylarenes by recyclable late transition metal catalysts

Methods

Sample preparation for pseudo ternary phase diagram at constant temperature

The phase behavior of a four-component system is described in pseudo ternary phase diagrams in which the weight ratio of surfactant/cosurfactant is fixed. The determination of the phase behavior was performed in a thermostated bath (T ± 0.1 K). Ten weighted samples composed of mixtures of (surfactant + cosurfactant) and oil were prepared in culture tubes sealed with Viton -lined screw caps at predetermined weight ratios of oil/ surfactant/cosurfactant. The mixtures were titrated with water and were equilibrated during a time interval of up to 24 h. The different phases were determined visually and optically using crossed polarizers method. Appearance of turbidity was considered as an indication for phase separation. The phase behavior was determined only after sharp interfaces had become visible. Centrifuging the samples accelerated the completion of this process. Every sample that remained transparent and homogeneous after vigorous vortexing was considered as belonging to the one phase region in the phase diagram.[13,14]

Ultrasonic velocity and density

The ultrasonic velocity and density were measured using a density and sound velocity analyzer (DSA 5000M- Anton Paar, Austria) with a sound velocity resolution of 0.5 ms^{-1} and density resolution of ($5*10^{-6}$ g cm^{-3}). A 3 ml degassed sample is introduced using Hamilton glass syringe into a U-shaped borosilicate glass tube that is being excited electronically to vibrate at its characteristic frequency. The characteristic frequency (high frequency (above 100 kHz) acoustic waves) changes depending on the density of the sample. Through precise determination of the characteristic frequency and a mathematical conversion, the density of the sample can be calculated. The measuring cell is closed by an ultrasonic transmitter on the one side and by a receiver on the other side. The transmitter sends sound waves of a known frequency through the sample. The velocity of sound was calculated by determining of the period of received sound waves and by considering the distance between transmitter and receiver. Due to the high dependency of the density and velocity of sound values on the temperature, the measuring cells have to be thermostated precisely with two integrated Pt 100 platinum thermometers together with Peltier elements provide an precise thermostating of the sample that equals ±0.01K. Viscosity-related errors were automatically corrected over the full viscosity range by measuring the damping effect of the viscous sample followed by a mathematical correction of the density value. The instrument automatically detects gas bubbles in the density measuring cell by an advanced analysis of its oscillation pattern and generates a warning message. Measurements were made at 298, 310 and 318 K.

Dynamic light scattering

Particle size measurements were performed using Zetasizer Nano S (ZEN 1600) for the measurements of size and molecular weight of dispersed particles and molecules in solution by Malvern Instruments Ltd. (Worcestershire, United Kingdom). The equipment includes a 4mW, 633nm He-Ne laser. Size measurement range between 0.6nm to 6 μm, size measurement angle equals 173º, concentration range for size measurement was between 0.1ppm (0.00001vol%) – 40wt%, molecular weight range between 10^3 to 10^7Da and temperature measurement range between 275 K to 363 K. 1.5 ml micellar sample was introduced in a disposable polystyrene cuvettes and measured at temperatures range between 273 and 323 K by steps of 5 K. The particle hydrodynamic diameter is calculated from the translational diffusion coefficient (D) using the Stokes-Einstein relationship:

$$d_{\mathrm{H}} = \mathrm{k_B}T/6\pi\eta D \qquad (1)$$

where d_{H} is the hydrodynamic diameter, $\mathrm{k_B}$ is Boltzmann's constant, T is the absolute temperature and η is the solvent viscosity. The results are averages of 3 experiments.

Results and Discussion

Phase behavior

Figures 1 presents the phase behaviors of water/ sodium dodecyl sulfate /n-propanol/ allylbenzene systems at 298 K. The ratio (w/w) of n-propanol/ sodium dodecyl sulfate equals 2/1. As shown in the Figure, the phase behavior indicates that the transparent micellar region appears after the addition of about 20-wt% of water. Similar findings on the behavior of sodium dodecyl sulfate in the presence of other aromatic oils were reported.[14] The area of the one phase region , A_{T} (%), varies slightly with temperature. Similar behavior of the dependence of the phase behavior on temperature of ionic surfactants was reported elsewhere.[14]

Volumetric properties

The ultrasonic wave propagates through materials and as it transverses a sample, compressions and decompressions in the ultrasonic wave change the distance between molecules within the sample, which, in turn, respond by intermolecular repulsions and attractions

DOI: 10.17628/ecb.2012.1.141-145

and probes the elastic properties of materials.[15-17]. Figure 2 represent the variation in the density as function of the water volume fraction for the water/n-propanol/ sodium dodecyl sulfate /allylbenzene system at 298 K.

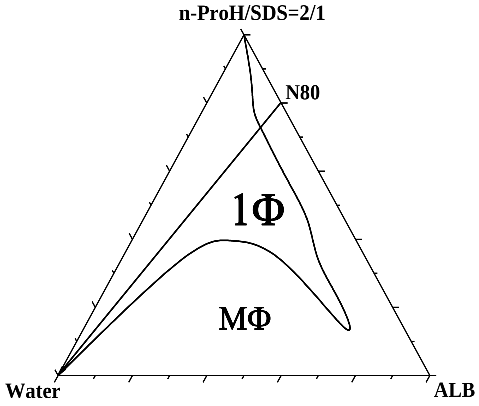

Figure 1. Pseudoternary phase diagram of the water/n-propanol/ sodium dodecyl sulfate /allylbenzene system at 298 K. The mixing ratio (w/w) of n-propanol/surfactant equals 2/1. The one phase region is designated by 1Φ, and the multiple phase regions are designated by (MΦ). N80 is the dilution line where the weight ratio of (surfactant + propanol)/allylbenzene equals 4/1.

The relation (2) can evaluate the excess volume of micelle formation, keeping in view the additivity of volumes of micellar, aqueous and oil phase,

$$V^E = V_{mic} - \sum_i \phi_i V_i \tag{2}$$

where V^E is the excess volume, V_{mic} is the measured micellar specific volume, ϕ_i is the volume fraction of component *i* in the micellar system and V_i is the specific volume of component *i*.

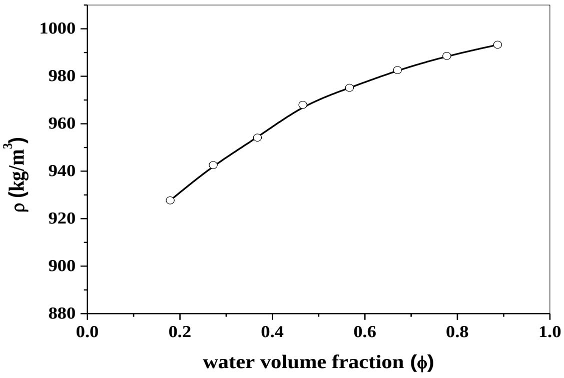

Figure 2. Variation of the density as function of water volume fraction for water/n-propanol/sodium dodecyl sulfate/allylbenzene micellar systems at 298K along the dilution line N80 presented in Figure 1

Figure 3 presents the variation in the excess volume as function of water volume fraction and temperature. The excess volumes are negative and decrease for water volume fraction below 0.3. For water volume fractions between 0.3 and 0.5 the excess volume stabilizes. For water volume fractions above 0.5 the excess volume increase dramatically but remain negative. Negative values of excess volume indicates that the system contracts upon addition of water. The values of excess volume were also determined as function of temperature and it was found that excess volume increases with temperature indicating expansion of the systems with temperature. This behavior could be related to breakage of hydrogen bonds or to dissociation of ionic head groups. Figure 4 presents schematically the proposed microstructures associated with the change in water volume fraction along the N80 dilution line shown in Figure 1. Figure 5 represents the variation of the ultrasonic velocity as function of the water volume fraction for the water/n-propanol/ sodium dodecyl sulfate/allylbenzene system. The ultrasonic velocity increases with the water volume fraction up to 0.8 thereafter decreases. The variation in the values of ultrasonic velocity as function of water volume fraction provides information on the state of water. At low water

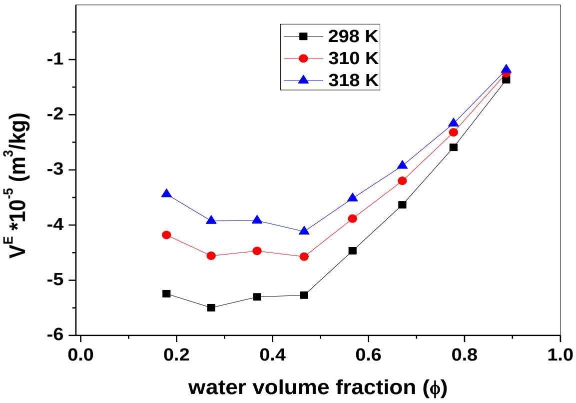

Figure 3. Variation of the excess volume as function of water volume fraction for water/n-propanol/sodium dodecyl sulfate/allylbenzene micellar systems at 298, 310, and 318K along the dilution line N80 presented in Figure 1

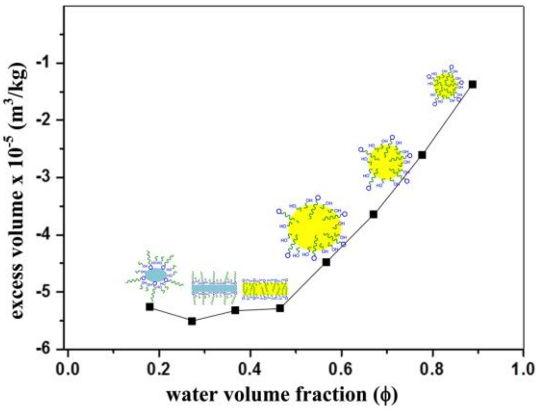

Figure 4. Schematic presentation of the proposed microstructures associated with the change in water volume fraction along the N80 dilution line

DOI: 10.17628/ecb.2012.1.141-145

volume fraction the properties of water are very different from those of bulk (free water) indicating the entrapment of water in the micellar core suggesting the presence of water-in-oil microstructure. The increase in the values of ultrasonic velocity upon addition of water indicates structural transitions along the water dilution line. For water volume fraction above 0.8 the ultrasonic velocity approaches that of pure water indicating that water is the continuous phase and oil-in-water microstructure is present.

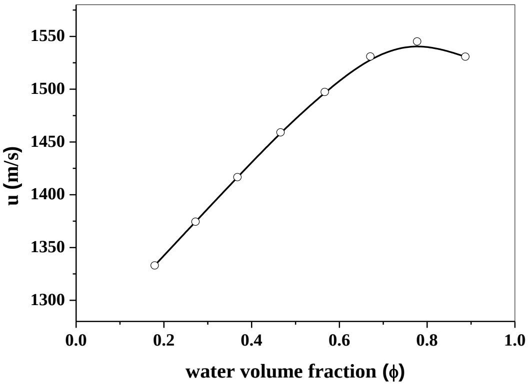

Figure 5. Variation of the ultrasonic velocity as function of water volume fraction for water/n-propanol/sodium dodecyl sulfate/allylbenzene micellar systems at 298K along the dilution line N80 presented in Figure 1

Since ultrasonic velocity is determined by the change of physical properties at the interface between the particle core and the continuous medium, the ultrasonic velocity variation shall also be correlated to the variation of the size of the particle core. In order to better understand these results, we analyzed the ultrasonic velocity in terms of isentropic compressibility k_s, which represents a relative change of volume per unit of pressure applied at constant entropy. k_s is much more sensitive to structural changes than the velocity and can provide qualitative information about the physical nature of the aggregates.

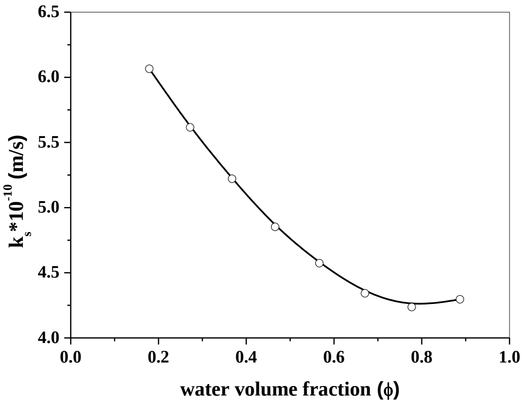

Figure 6. Variation of the isentropic compressibility as function of water volume fraction for water/n-propanol/sodium dodecyl sulfate/allylbenzene micellar systems at 298K along the dilution line N80 presented in Figure 1

The isentropic compressibility k_s values have been evaluated with the help of the Laplace equation.[18-20]

$$k_s = \frac{1}{u^2 \rho} \qquad (3)$$

Figure 6 presents the variation of the isentropic compressibility k_s as function of the water volume fraction. The isentropic compressibility decreases with the water volume fraction below 0.8 and increases thereafter. The variation in the values of isentropic compressibility as function of increasing water volume fraction indicates structural transitions from water-in-oil to bicontinuous to oil-in-water microstructure. The values of the isentropic compressibility were determined as function of temperature (see Figure 7) and found to increase with temperature for water volume fractions below 0.8 while for water volume fraction above 0.8 the isentropic compressibility values decrease.

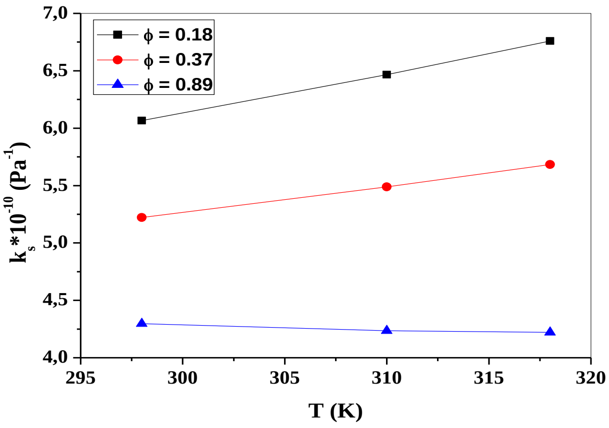

Figure 7. Variation of the isentropic compressibility as function of temperature for water/n-propanol/sodium dodecyl sulfate/allylbenzene micellar systems along the dilution line N80 presented in Figure 1

Diffusion properties

On the assumption that exchange processes are negligible for the surfactant, we can estimate the hydrodynamic diameter (d_H) of the micellar system in the water-rich region at water volume fraction equals 0.95 and above using equation 1. The variation in the values of the hydrodynamic diameter (d_H) at water volume fraction of 0.95 for the studied system as function of temperature is shown in Figures 8.

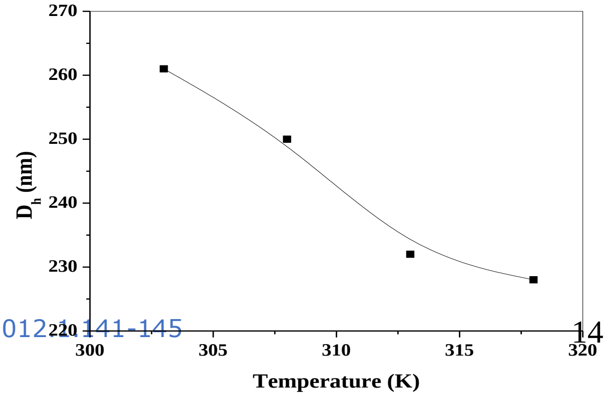

Figure 8. Variation of the particle hydrodynamic diameter as function of temperature for water/n-propanol/ sodium dodecyl sulfate/ allylbenzene oil-in-water nanoemulsions.

As shown in Figure 8, the hydrodynamic diameter decreases with temperature from 269 nm at 303K to 249 nm at 323K. The values of the hydrodynamic diameter indicates that the micellar systems formed are nanoemulsions. These systems will be used as alternative reaction media for the isomerization of allylbenzene.

Conclusion

New nanoemulsions were developed for performing reactions with hydrophobic reagents that will lead to a significant reduction in the vast amount of organic solvents used currently in organic syntheses, and consequently increase the safety and diminish the cost of chemical processes. Quantitative analysis of the studied properties enabled the characterization of structural transition along the micellar phase. Determination of the particle size diameters of the diluted systems enables the distinction of the diluted micellar systems as nanoemulsions. Since the particle size of the micellar system is an important parameter in determining the yield of isomerization reaction of allylbenzene, the results presented in this study recommend performing these reactions at water volume fractions above 0.95 or at surfactant contents slightly above the critical micelle concentration and at high temperatures.

Acknowledgment

We gratefully acknowledge the financial support of this trilateral study by the Deutsche Forschungsgemeinschaft (DFG) through grant SCHO 687/8-2.

References

[1] Forgiarini, A., Esquena, J., González, C.,Solans, C., *Progress in Colloid and Polymer Sci.*, **2000**, *115* , 36.

[2] Forgiarini, A., Esquena, J., González, C.,Solans, C., *Progress in Colloid and Polymer Sci.*, **2001**, *118* , 184.

[3] Solans, C., Izquerdo, P., Nolla, J., Azemar, N., Garcia-Celma, M. *Current Opinion in Colloid & Interface Sci.*, **2005**, *10*, 102.

[4] Maestro, A., Solè, I., González, C., Solans, C., Gutiérrez, J. M., *J. Colloid and Interface Sci.*, **2008**, *327*, 433.

[5] Constantinides, P. P., Chaubal, M. V., Shorr, R., *Adv. Drug Delivery Reviews* **2008**, *60*, 757.

[6] Antonietti, M., Landfester, K. *Progress in Polymer Sci.*, **2002**, *27*, 689.

[7] Sarker, D.K.. *Current Drug Delivery*, **2005**, *2*, 297.

[8] Wei, W., Keh, C. C. K., Li, C.-J., Varma, R. S., *Clean Technol. Environ. Policy* **2004**, *6*, 250. and references cited therein.

[9] Lindström, U. M. (Ed). *Organic Reactions in Water*, Blackwell Publishing, **2007**.

[10] Abu-Reziq, R., Blum, J., Avnir, D. *Chem. Eur. J.*, **2004**, *10*, 958.

[11] Tsvelikhovsky, D., Blum, J. *Eur. J. Org. Chem.*, **2008**, 2417.

[12] Nairoukh, Z., Blum, J. *J. Mol. Catal. A: Chem.* **2012**, *358*, 129. and references cited therein.

[13] Fanun M. J Colloid Interface Sci., **2010**, 343, 496.

[14] Fanun, M., Shakarnah, A., Meltzer, D., Schwarze, M., Schomaecker, R., Blum J., *Tenside Surf. Deterg*. **2011**, *48*, 400.

[15] Hickey, S., Lawrence, M. J., Hagan, S. A. and Buckin, V., Langmuir **2006**, *22*, 5575.

[16] Mehta S. K., Bala, K., Fluid Phase Equilibria, **2000**, *172*, 197.

[17] Alberola, C., Dederichs, T., Emeis, D., Moller, M., Sokolowski, T., Witten, K.P., J. Colloid Interface Sci., **2007**, **307**, 500.

[18] Ye, L., Weitz, D. A., Sheng, P., Bhattacharya, S., Huang, J. S., Higgins, H. J. J. Phys. Rev. Lett., **1989**, *63*, 263.

[19] Wood, A. B. *A Textbook of Sound*, G. Bell, London, **1941**.

[20] Barret-Gultepe, M. A., Yeager, E. B., J. Phys. Chem., **1983**, *87*, 1039.

Received: 05.09.2012.

Accepted: 06.09.2012.

STUDIES ON THE UTILIZATION OF SOLAR ENERGY IN THE EFFLUENT TREATMENT

K. K. Sivakumar[a] and M.S. Dheenadayalan[b]

Keywords: Effluent Treatment, Effluent, dyestuff, solar evaporation, zero liquid discharge

Textile industry is the largest number compared to other industries in Tamil Nadu. In spite of the continuous efforts to prevent water pollution from these industries, solving of the high total dissolved solids (5000-10000 mg L^{-1}) in the effluent is not yet successfully done. India, being the tropical country, solar radiation is available in plenty during most of the year, enables the industries to use the solar evaporation ponds as a simple and economical treatment system. An experimental textile effluent evaporation tank made by natural black colored stone is developed. It showed excellent results of evaporation utilizing solar energy. The usage of overall pond depth of 17.5 cm and an initial liquid depth ranging from 5 cm to 15 cm depending upon the season with a salt removal period ranging from 5 to 6 days will make the solar evaporation pond an effective system for the recovery of the dissolved salts. Data have been collected, allowing us to know the mean evaporation to be expected in the region of Tamil Nadu, India. A solar wastewater treatment system is proposed for textile industry from this, which leads to possible recycling of chemicals and water by using solar evaporation. Calculation shows that the proposed system is quite competitive with conventional coagulation in the range of small textile effluent treatment installations.

* Corresponding Authors
E-Mail: sivakumarccet@gmail.com
[a] Department of Chemistry, Chettinad College of Engineering & Technology, Karur-639 114. Tamil Nadu, INDIA
[b] PG and Research Department of Chemistry, GTN Arts College, Dindigul. Tamil Nadu, INDIA

Introduction

Textile industry is the largest number compared to other industries in Tamil Nadu. In spite of the continuous efforts to prevent water pollution from these industries, solving of the high total dissolved solids (TDS) in the effluent is not yet successfully done. India, being the tropical country, solar radiation is available in plenty during most of the year, enables the industries to use the solar evaporation ponds as a simple and economical treatment system. Since the available solar radiation energy is not used properly in the ponds, the attempt to use the solar evaporation ponds to recover the salts from the effluent led to a wrong impression that solar evaporation ponds are ineffective treatment systems.

In textile industries, evaporators can be installed to achieve zero liquid discharge of effluent. Evaporation is being considered as an alternative process in an increasing number of wastewater treatment applications. It can be effective for concentrating or removing salts, heavy metals and a variety of hazardous materials from solution. Also, it may be used to recover useful by-products from a solution, or to concentrate liquid wastes prior to additional treatment and final disposal. Most applications of the technology also produce a high quality, reusable distillate-a very important feature where water conservation is a priority.

During evaporation, a solution is concentrated when a portion of the solvent, usually water, is vaporized, leaving behind saline liquor that contains virtually all of the dissolved solids, or solute, from the original feed. The process may be carried out naturally in solar evaporation ponds, or through the use of commercially available evaporation equipment. [1]

Solar Evaporation Ponds may be extensively used in the textile dyeing and bleaching industries to treat the effluent which contains high total dissolved solids in the range of 5000 to 10000 mg L^{-1}. Presence of TDS in the treated effluent discharge by the industries poses a great danger to the agricultural lands. Optimum usage of the existing solar evaporation ponds is the need of the hour. Hence, there is a necessity for a study to find the variation in the rate of evaporation from the effluent stored in the ponds so as to suggest a method for an effective operation of the ponds.[2]

The development of solar evaporation technology gained attraction in the effluent purification both economic and environmental benefits. This chapter covers the idea of solar evaporation system by constructing solar ponds to avoid groundwater contamination and safe recovery of salt removal. [3]

Principle of solar evaporation tank

Radiation is a process by which heat flows from a body at a higher temperature to a body at a lower temperature when the bodies are separated in space or even a vacuum exists between them. The energy transmitted so called radiant heat. Radiation is the mode of the heat transfer by which the sun transfers energy to the earth. The quantity of energy leaving a surface as radiant heat depends on the absolute temperature and the nature of the surface. A perfect radiator, so called black body emits radiant energy from its surface at a rate 'Q' is given by,

$$Q = A\,\sigma\,T^4 \tag{1}$$

Where, A is the area of the body, T is absolute temperature in K and σ is a constant known as Stefan's Boltzmann constant.

Real bodies do not meet the specifications of an ideal radiation and emit radiation at a lower rate than black bodies. The ratio of the radiation emission of a real body to the

DOI: 10.17628/ecb.2012.1.146-149

radiation emission of a black body at the same temperature is called the emittance. Thus a real body emits radiation at a rate.

$$Q = \varepsilon A \sigma T^4 \qquad (2)$$

where, ε is the average emittance of the surface. According to physical phenomena, the surface which absorbs all incident energy is called black surface. It is defined as one which absorbs the entire energy incident upon it and reflects none; such a body is used extensively in radiation heat transfer work.

Materials and Methods

Black Kadappa stone – natural material quite impervious, long-lasting, hard, more resistant than most other sedimentary rocks and can withstand to any exposure. Its hardness is 3 to 4 on Mohr's scale, density is between 2.5 and 2. 7 g cm$^{-3,}$ compressive strength is between 60 and 170 N mm^{-2}, water absorption is less than 1% and porosity is quite low.

Industrial mixed effluents collected from outlet of the local industry. It is measured for TDS about 4700 ppm.

The solar evaporation tank is constructed with three segments. They are having the depth of 17.5 cm and area of 1849 cm^{-2} in stepwise position. The outlet pipe from tank-I is located near the upper part of the tank-II. Likewise the outlet pipe from tank-II is located near the upper part of the tank-III. These three tanks are placed on cemented roof in North-South direction as shown in the figure. The three tanks are kept in open exposed sunlight from the greater absorption of solar energy in the stepwise position.

The solar evaporation tank contains untreated/partially treated dyeing effluent. By natural buoyancy forces causes the heated layers of water to rise as it becomes less dense, once it reaches the surface the water loses it heat to the air through convection. The cold part which is heavier moves down to replace the warmer part creating a natural convective circulation that mixes the water and dissipates the heat. Initially, 15 L of effluent is placed in the tank-I, measured depth is about 9.2 cm. 10 ppm alum and 0.5 ppm polyelectrolyte is added into the tank so as to facilitate clariflocculation and then the supernatant liquid is allowed to flow into the tank-II and tank-III. Now the depth of the each tank is 4.2 cm. TDS of both tanks is measured with the help of TDS meter is about 4264 ppm. Now both the tanks are exposed to solar radiation on first day. The temperature of the effluent at 10 am is measured with the help of thermometer and then is measured for one hour time interval for the effluent level depth. TDS and temperature effluent in the tanks II and III was noted. This process was continued upto 4 pm and the same is continued for 6 days for complete evaporation.

The same procedure is followed with 10 L of effluent in tank-I. The tank-I depth is 6.2 cm. The tank-II and III depth is about 2.7 cm each. The process had 5 days for complete evaporation.

Studies have been conducted in the solar evaporation ponds to find the following:

1) The daily average rate of evaporation of the effluent stored in the pond

2) The initial liquid depth of the effluent that is to be stored in the pond for the efficient operation of the pond;

3) A simple method to increase the rate of evaporation of the effluent stored in the pond;

4) A regression equation to estimate the rate evaporation of the effluent stored in the pond using the generally available meteorological data and the TDS of the effluent.

5) The variations in the rate of evaporation of the effluent with that of water, salt water, and effluent added with black dye that were stored in the different ponds under similar conditions are also studied.

Result and Discussion

The experimental observation is presented in the Table 1 and 2. Solar evaporation certainly causes the decrease in depth of effluent level in tanks II and III to a greater extent corresponding to the value of temperature and so the concentration of effluent in the tanks increases, clearly indicates the evaporation.

Table 1 -Solar Evaporation of 15 L Effluent

Sl. No.	**Day No.**	**Temp.(°C)**	**Depth, cm**	**TDS, ppm)**
	Tank-II and III			
1	**Day 1 (Start)**	**30**	**4.1**	**4264**
2	Day 1 (End)	35	3.5	5418
3	Day 2 (Start)	28	3.4	5450
4	Day 2 (End)	36	2.8	6910
5	Day 3 (Start)	32	2.7	7012
6	Day 3 (End)	36	2.1	12022
7	Day 4 (Start)	30	2	12124
8	Day 4 (End)	37	1.5	17520
9	Day 5 (Start)	32	1.4	17610
10	Day 5 (End)	38	0.8	23820
11	Day 6 (Start)	29	0.7	24010
12	**Day 6 (End)**	**Completely Evaporated**		

Table 2 Solar Evaporation of 10 L Effluent

Sl. No.	**Day No.**	**Temp., °C**	**Depth,cm**	**TDS,ppm**
	Tank-II and III			
1	Day 1 (Start)	30	2.7	4214
2	Day 1 (End)	33	2.6	4340
3	Day 2 (Start)	28	2	5520
4	Day 2 (End)	36	1.5	6840
5	Day 3 (Start)	32	1.4	6880
6	Day 3 (End)	36	1	11840
7	Day 4 (Start)	30	0.9	11900
8	Day 4 (End)	37	0.4	16862
9	Day 5 (Start)	32	0.3	16940
10	**Day 5 (End)**	**Completely Evaporated**		

The Fig.1 to 4 explains the day vs depth of the tank and day vs TDS in the tank effluent. The five parameters such as temperature, velocity of the wind, the atmospheric pressure, extent of free surface of effluent and the quantity of vapor already present in the environment plays important role in the evaporation.

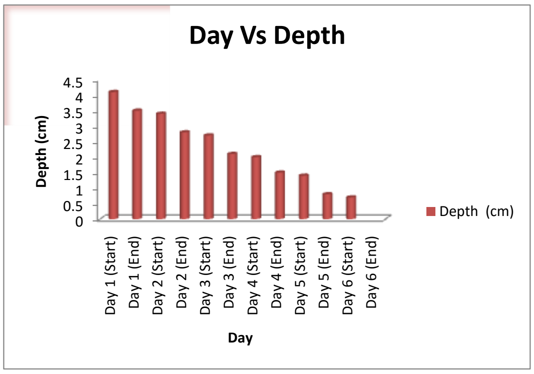

Fig. 1. Depth of the tank at various days (for 15 L)

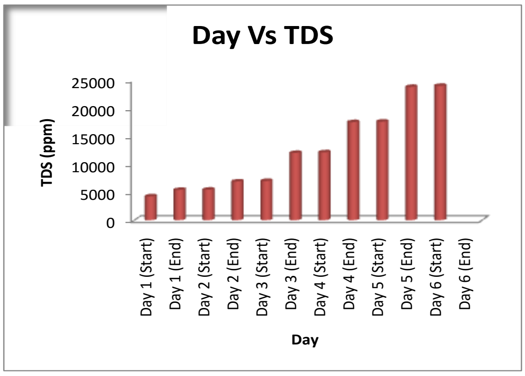

Fig. 2. TDS of the tank at various days (for 15 L)

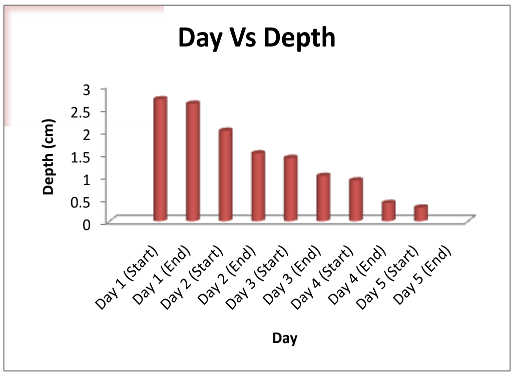

Fig. 3. Depth of the tank at various days (for 10 L)

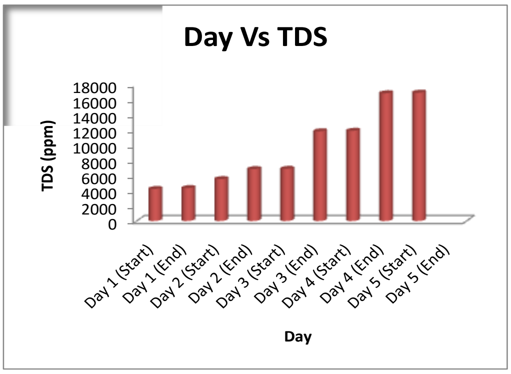

Fig. 4. TDS of the tank at various days (for 10 L)

As higher the temperature of the liquid the greater is the kinetic energy of the molecules and hence faster is the formation of vapor. The rate of evaporation increases with the velocity of the wind blowing over the surface of the exposed effluent, since the molecules of effluent escaping from its surface are carried away immediately as they are out of the effluent. The rate of evaporation is inversely proportional to the atmospheric pressure. It has been found experimentally that low atmospheric pressure increases the rate of evaporation and it is maximum in vacuum. The larger area of the free surface of the effluent exposed to the atmosphere increases the rate of evaporation. Moreover the rate of evaporation of any effluent decreases with the increase of the quantity of vapor of that liquid in the air.

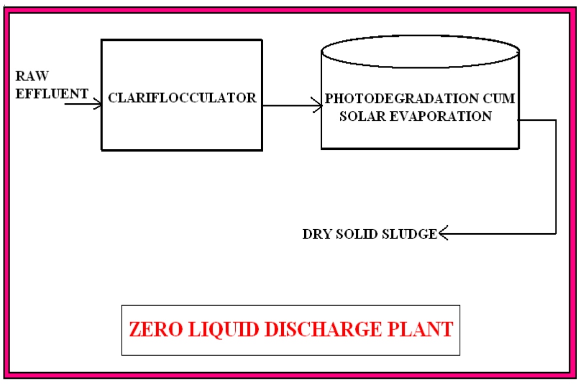

Fig. 5. Proposed Zero Liquid Discharge Plant

The studies have indicated that the effectiveness of the pond depends mainly on the intensity of the solar radiation of the day and the initial liquid depth of the effluent stored in the pond. The usage of the overall pond depth of 15 cm and an initial liquid depth ranging from 4 cm to 13 cm depending upon the season with a salt removal period ranging from 7 to 10 days will make the solar evaporation pond an effective treatment system for the recovery of the dissolved salts. Usage of natural black kadappa stone alternate to cement concrete ponds increases the rate evaporation of the effluent by around 100% which can be easily adopted by industries to increase the rate of evaporation. The proposed zero liquid discharge plant is shown in the Figure 5.

Conclusion

The rise in temperature of dyeing effluent from 50ºC to 70ºC improves the greater evaporation of effluent having high TDS.

Solar energy can be dependable energy source with specialized nature of its wide and comfort utilization without any new requirement of high technical ideas. In addition there is no underground seepage which causes groundwater contamination.

This black colored kadappa stone evaporation system can be offered as ecofriendly, simple and easy for adoption. It offers better performance during summer with very high evaporation rate. The total number of days taken for the complete evaporation of 15 L of effluent is 6 days and 5 days for 10 L for the designed tank. This is comparatively better performance than cement concrete tank which takes average 10 days for complete evaporation.

Acknowledgement

The authors are thankful to their concerned Management and Principal of their college for constant encouragement and financial support to promote such innovative solution for the environmental effluent problem.

References

[1] Nielsen C., A. Akbarzadeh, J. Andrews, H.R.L. Becerra and P. Golding, *The History of Solar Pond Science and Technology*, in*:* Proceedings of the 2005 Solar World Conference Orlando, FL , **2005**.

[2] Salzman S.A., G. Allinson, F. Staqnitti, M. Coates and R.J. Hill, *Water Res*., **2001**, *35*(9), p.2121-2128.

[3] Jarboui R., F. Sellami, C. Azri, N. Gharsallah and E. Ammar, *J Hazard Mater*., **2010**. *176*(1-3), 992.

Received: 05.09.2012.

Accepted: 06.09.2012

DOI: 10.17628/ecb.2012.1.146-149

CORROSION INHIBITION BY TRISODIUM CITRATE (TSC – Zn^{2+} SYSTEM)

B. Shyamala Devi[a] and S. Rajendran[b,c]

Keywords: Corrosion inhibition, Carbon steel; Trisodium citrate; Synergistic effect

The inhibition efficiency (IE) of various concentrations of a TSC- Zn^{2+} system in controlling corrosion of mild steel immersed in well water was evaluated by a weight-loss study. The formulation consisting of 50 ppm of TSC and 25 ppm of Zn^{2+} showed 70% inhibition efficiency. A synergistic effect was noticed between trisodium citrate - Zn^{2+} system. In the presence of Zn^{2+} TSC has excellent inhibition efficiency. Polarization studies reveal that TSC - Zn^{2+} function as a mixed inhibitor. AC impedance spectra suggest that a protective film is formed on the metal surface. FTIR spectra reveal that the protective film consists of Fe^{2+} - TSC complex and $Zn(OH)_2$. SEM micrographs and AFM reveals that a protective film is formed on the metal surface

* Corresponding Authors
E-Mail: shyapranesh@yahoo.com
[a] Department of Chemistry, Vivekanandha Institute of Engineering and Technology for Women, Tiruchengodu, Tamil Nadu, India
[b] Corrosion Research Centre, Post Graduate and Research Department of Chemistry, GTN Arts College, Dindigul-624 005, India
[c] Department of Chemistry, RVS School of Engineering and Technology, Dindigul, India

1. INTRODUCTION

Water soluble carboxylic acids have been used as corrosion inhibitor. Much investigation suggests that corrosion inhibitors based on carboxylic acids remain a fruitful field of investigation.[1-30]

The ability of carboxylic acids to inhibit corrosion in automotive cooling systems was first reported more than 50 years ago. Aromatic carboxylic acids, such as benzoic acid and its derivatives, have been extensively studied and are used in Europe as corrosion inhibitors in commercials coolants. There are few studies of corrosion inhibition by aliphatic carboxylic acids in the open literature. In carboxylic acids the carboxyl groups form strong chemical bonds with Fe^{2+} which, it is suggested, compete successfully with Cl^- as a complexing agent for iron. It is suggested that the resulting carboxylate complex with iron is itself electrically neutral; it remains in the vicinity of the anode, thus interrupting the cycle of oxidation of Fe to Fe^{2+}, its complexation, transportation and further oxidation, to insoluble Fe^{3+} with release and recycling of the chloride.

The present work investigated the inhibition efficiency of TSC and Zn^{2+} on the inhibition efficiency of trisodium citrate-Zn^{2+}system in controlling corrosion of carbon steel (CS) immersed in well water. Potentio-dynamic polarization study and alternating current (AC) impedance spectra have been used. FTIR spectra reveal that the protective film consists of Fe^{2+} -TSC and $Zn(OH)_2$. SEM micrographs and AFM reveals that a protective film is formed on the metal surface.

2. EXPERIMENTAL

2.1.Weight loss method

The weighed specimen, in triplicate were suspended by means of glass hooks in 100 ml beakers containing 100 ml of well water containing various concentrations of the inhibitor in the presence and absence of Zn^{2+} for 3 days of immersion. After 3 days of immersion the specimens were taken out, washed in running water, dried and weighed. From the change in weights of the specimen, corrosion rates were calculated using the following relationship.

$$R_{corr} = \frac{\Delta m}{S * \Delta t} \qquad (1)$$

where

R_{corr} – corrosion rate, mg dm^{-2} d^{-1}
Δm – loss in weight (mg)
S – surface area of specimen, dm^2
Δt – period of immersion, day

Corrosion inhibition efficiency (IE) was then calculated using the equation

$$IE = 100 * \left[1 - \frac{W_2}{W_1}\right] \qquad (2)$$

where

W_1 - corrosion rate in the absence of the inhibitor,
W_2 - corrosion rate in the presence of the inhibitor

2.2. Potentiodynamic polarization study

This study was carried out in an H and CH electrochemical work station impedance analyzer model CHI 660. A three-electrode cell assemble was used. The working electrode was carbon steel with one face of the electrode of constant 1 cm^2 area exposed and the rest being shielded with red lacquer. A saturated calomel electrode (SCE) was used as reference electrode. A rectangular platinum, foil was used as the counter electrode. The area of the counter electrode was much larger compared to the area of the working electrode. This can exert a uniform potential field on the working electrode and minimized the polarization effect on the counter electrode. The results such as Tafel slopes, I_{corr} and E_{corr} values were calculated.

The working electrode and platinum electrode were immersed in well water in the absence and presence of inhibitor. Saturated calomel electrode was connected with the test solution through a salt bridge. Potential (E) vs log current (I) plots were then recorded. Corrosion potential (E_{corr}) and Tafel slopes b_a and b_c were determined from E vs log I plots. Tangents were drawn on the cathodic and anodic polarization curves. From the point of intersection of the two tangents I_{corr} and E_{corr} were calculated

2.3. AC impedance measurements

H and CH electrochemical work station impedance analyzer model CHI 660 was used to record AC impedance measurements. The cell setup was the same as that used for polarization measurements. The real part (z') and imaginary part (z'') of the cell impedance were measured in ohms for various frequencies. The R_t (charge transfer resistance) and C_{dl} (double layer capacitance) values were calculated.

2.4. Surface characterization studies

The carbon steel specimens were immersed in blank, as well as inhibitor solutions, for a period of one day. After 1 day, the specimens were taken out and dried. The nature of the film formed on the surface of the metal specimens was analyzed by various surface analysis techniques.

2.4.1. FTIR spectra

These spectra were recorded in a Perkin – Elmer 1600 spectrophotometer. The film was carefully removed, mixed thoroughly with KBr and made into pellets and the FTIR spectra were recorded. After the immersion period of 1 day in various environments, the specimens were taken out of the test solutions and dried. The film formed on the surface was scratched carefully and it was thoroughly mixed so as to make it uniform throughout. FTIR spectrum of the powder (KBr pellet) was recorded using Perkin – Elmer 1600 FTIR spectrophotometer with a resolving power of 4 cm^{-1}

2.4.2. Scanning Electron Microscopic studies (SEM)

The carbon steel specimen immersed in blank and in the inhibitor solution for a period of one day was removed, rinsed with double distilled water, dried and observed in a scanning electron microscope to examine the surface morphology. The surface morphology measurements of the carbon steel were examined using Hitachi S-3000 H computer controlled scanning electron microscope.

2.4.3. Atomic Force Microscopy characterization (AFM)

The carbon steel specimen immersed in blank and in the inhibitor solution for a period of one day was removed, rinsed with double distilled water, dried and subjected to the surface examination. The surface morphology measurements of the carbon steel surface were carried by atomic force microscopy (AFM) using PicoSPM 2100 with the software version of Picoscan version 5.4.

2.5. Determination of biocidal efficiency of the system

The inhibitor formulation that offered the best corrosion inhibition efficiency with the biocide Sodium dodecyl sulphate (SDS) and N-cetyl-N,N,N-trimethyl ammonium bromide (CTAB) was selected. The biocidal efficiency of SDS and CTAB on the inhibitor system was determined. Various concentrations of CTAB and SDS namely 50 ppm, 100 ppm, 150 ppm, 200 ppm and 250 ppm were added to the formulation consisting of the inhibitor system. Polished and degreased carbon steel specimens in triplicate were immersed in these environments for a period of three days. After three days one ml each of test solutions from the environments was pipetted out into sterile Petri dishes containing about 20 ml of the sterilized zobell medium kept in a sterilized environment inside the laminar flow system fabricated and supplied by CECRI – Pilani. The Petri dishes were then kept for 48 hours. The total viable heterotropic bacterial colonies were counted using a bacterial colony counter.

3. RESULTS AND DISCUSSION

3.1. Weight loss method

The corrosion rates (CR) of carbon steel immersed in well water and also inhibition efficiencies (IE) in the absence and presence of inhibitor trisodium citrate (TSC) and Zn^{2+} obtained by weight loss method are given in Tables 1 to 3.

It is observed from Table 1 that TSC shows some inhibition efficiencies. 50 ppm of TSC has 22% inhibition efficiency. As the concentration of TSC increases the inhibition efficiency increases. 250 ppm of TSC shows 50 % IE.

Table 1. Corrosion rates of (CR mdd) carbon steel immersed in well water, and inhibition efficiencies (IE%) obtained by weight loss method

TSC, ppm	$Zn^{2+,}$ ppm	CRmdd	IE, %
0	0	23.64	-
50	0	18.44	22
100	0	16.07	32
150	0	14.18	40
200	0	12.29	48
250	0	11.82	50

Immersion period = 3 days

DOI: 10.17628/ecb.2012.1.150-157

3.2. Influence of Zn^{2+} on the inhibition efficiency of TSC

The influence of Zn^{2+}on the inhibition efficiency of TSC is given in Tables 2 and 3. It is observed that when Zn^{2+} is added, the inhibition efficiency of TSC increases. The increase in IE is more pronounced at 50 ppm of Zn^{2+} than at lower concentrations of Zn^{2+}, ie at 25 ppm. It is observed that a synergistic effect exists between TSC and Zn^{2+} . For example, 25 ppm of Zn^{2+} has 15% IE. 250 ppm of TSC has 50% IE. Interestingly their combination has 90% IE. This suggests that a synergistic effect exists between TSC and Zn^{2+}.

Table 2 : Corrosion rates of (CR mdd) carbon steel immersed in well water, and inhibition efficiencies (IE%) obtained by weight loss method

TSC ppm	Zn^{2+} ppm	CR mdd	IE %
0	50	22.46	5
50	50	6.38	73
100	50	4.73	80
150	50	3.55	85
200	50	2.36	90
250	50	1.	1895

Immersion period = 3 days

Table 3 : Corrosion rates of (CR mdd) carbon steel immersed in well water, and inhibitionefficiencies (IE%) obtained by weight loss method

SC ppm	Zn^{2+} ppm	CR mdd	IE %
0	25	20.09	15
50	25	7.09	70
100	25	4.96	79
150	25	4.73	80
200	25	4.02	83
250	25	2.36	90

Immersion period = 3 days

3.3. Influence of Immersion period on IE of TSC-Zn^{2+}system

The influence of immersion period on IE of TSC - Zn^{2+}system is given in Tabe. 4. It is observed as the period of immersion increases (1,3,5,7,9 days) the IE% decreases. This is due to the fact as the immersion period increases the protective film is ruptured by the cl^- , present in the solution.

3.4. Analysis of results of potentiodynamic plorization study

Polarization study has been used to study the formation of protective film on the metal surface. The potentiodynamic polarization curves of carbon steel immersed in well water in the absence and presence of inhibitors are shown in Fig 1.

The corrosion parameters namely corrosion potential (E_{corr}) Tafel slopes, b_c and b_a, linear polarization resistance (LPR) and corrosion parameter (I_{corr}) are given in Table 5. It is observed (Fig .1a) that when carbon steel immersed in well water, the corrosion potential is - 701 mV vs SCE (saturated Calomel Electrode). The LPR value is 3.742×10^4ohm cm^2. The corrosion current value is 1.219×10^{-6} A/cm^2.

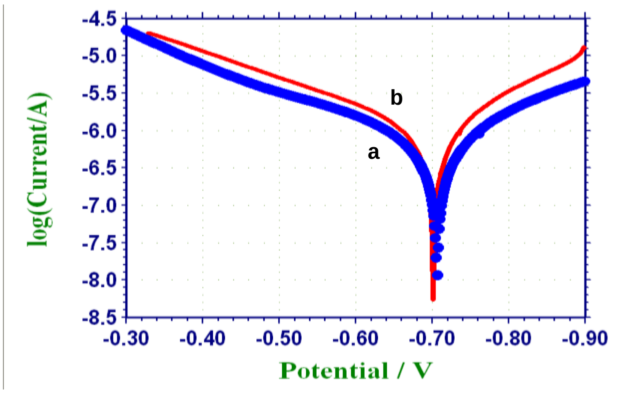

Figure 1. Polarization curves of mild steel immersed in various test – solutions. a - well water; b - TSC (50 ppm) + Zn^{2+} (25 ppm)

When 50 ppm of TSC and 25 ppm of Zn^{2+} are added to the above environment the corrosion potential is shifted to the anodic side (-706 mV vs SCE) (Fig .1.b). However this shift is very small. Further, the Tafel slopes are almost equal. Hence TSC- Zn^{2+} system functions as a mixed inhibitor. It is observed from Table 5. that the LPR value increases and the corrosion current value decreases. These observations suggest the formation of a protective film on the metal surface. This prevents the corrosion of metal.

3.5. Analysis of AC impedance spectra

AC impedance spectra of carbon steel immersed in well water in the absence and presence of inhibitors are showm in Fig .2 (Nyquist plots) and Fig .3 (Bode plots).

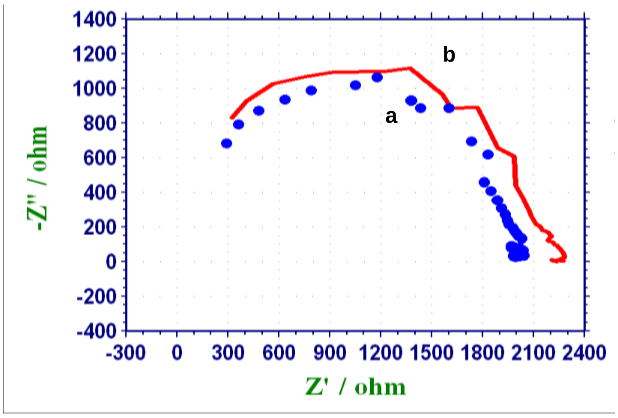

Figure 2. Ac impedance spectra of carbon steel immersed in various test solutions (Nyquist plot): a- well water; b- well water + TSC (50 ppm) + Zn^{2+} (25ppm)

The corrosion parameters namely charge transfer resistance (R_t) and double layer capacitance (C_{dl}) derived from Nyquist plots are given in Table 6. The impedance, log (Z/ohm) values derived from Bode plots are also give in Table 6. It is observed that when carbon steel immersed in well water the R_t value is 1779.8 ohm cm^2. The C_{dl} value is 2.865×10^{-8} F/cm^2 . The impedance value [log (Z/ohm)] is 3.305.

Table 4 : Influence of immersion period on TSC - Zn^{2+}system

Days	1	3	5	7	9
Well water (Blank)					
CR mdd	18.32	23.64	25.14	27.36	29.42
TSC (50ppm) + Zn^{2+} (25ppm)					
CR mdd	3.48	7.09	8.80	11.22	13.53
IE%	81	70	65	59	54

Table 5: Corrosion parameters of carbon steel immersed in well water, obtained frompotentiodynamic polarization study

System	E_{corr}, mV vs SCE	b_a, mV/decade	b_c, mV/decade	LPR, Ohm cm^2	I_{corr}, A/ cm^2
Well water	-701	249	181	3.742 x 10^4	1.219 x 10^{-6}
Well water+TSC (50ppm)+ Zn^{2+} (25ppm)	-706	250	201	6.063 x 10^4	7.985 x 10^{-7}

When inhibitors (50ppm of TSC + 25ppm of Zn^{2+}) are added the R_t values increases from 1779.8 to 2080.4 ohm cm^2. The C_{dl} value decreases from 2.865 x 10^{-9} to 2.451 x 10^{-9} F/cm^2. The impedence value increases from 3.305 to3.340. These observation suggest that a protective film is formed on the metal surface.

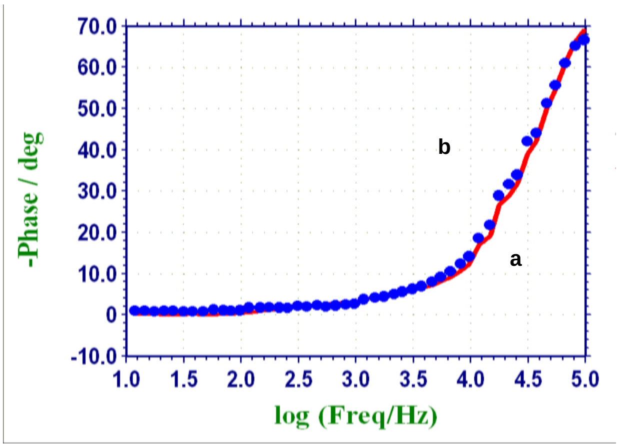

Figure 3.i: Ac impedance spectra of carbon steel immersed in various test solutions (Bode plot impedance) a - well water (blank); (b) well water + TSC (50ppm)+Zn^{2+} (25ppm)

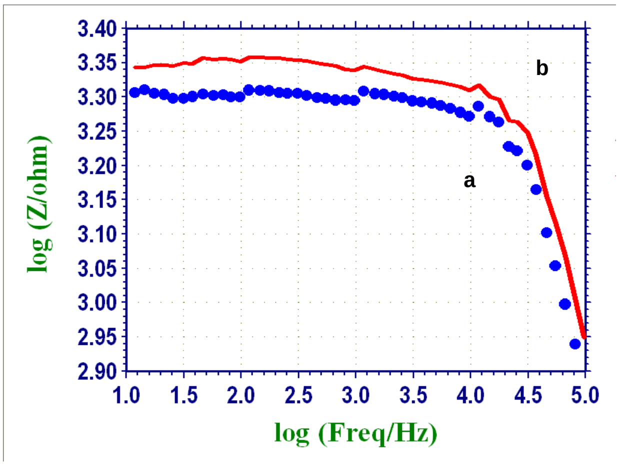

Figure 3.ii: Ac impedance spectra of carbon steel immersed in various test solutions (Bode plot-phase) (a) - well water (Blank) (b) -well water +TSC (50ppm)+Zn^{2+} (25ppm)

Table 6. Corrosion parameters of carbon steel immersed in well water obtained form AC impedance spectra

System	R_t, ohm cm^2	C_{dl}, F/cm^2	Impedance [log(Z/ohm)]
Well water	1779.8	2.865 x 10^{-9}	3.305
Well water + TSC(50ppm)+ Zn^{2+} (25ppm)	2080.4	2.451 x 10^{-9}	3.340

3.6. Analysis of FTIR spectrum

The structure of trisodium citrate (TSC, $C_6H_5Na_3O_7$, Mw=258.06) is shown in scheme 1:

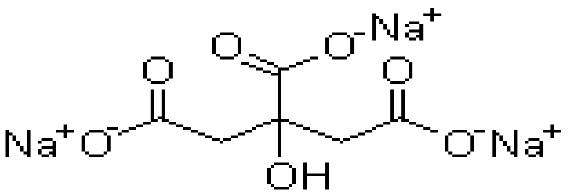

FTIR spectrum of pure TSC is shown in Fig.4.a.The C=O stretching frequency occurs at 1599 $cm^{-1.}$ The FTIR spectrum of the film scratched from the surface of the metal immersed in well water 50 ppm of TSC and 25 ppm of Zn^{2+} is given in Fig. 4 b . It is seen from the spectrum that the C=O stretching frequency of TSC in the free state has shifted from 1599cm^{-1} to 1590 cm^{-1}. This shift indicates that the carbonyl oxygen atom was coordinated to Fe^{2+} resulting in the formation of Fe^{2+}-TSC complex on the anodic sites of the metal surface. The band at 1351 cm^{-1} was appeared due to the presence of $Zn(OH)_2$.

3.7. SEM Analysis of Metal surface

SEM provides a pictorial representation of the surface. To understand the nature of the surface film in the absence and presence of inhibitors and the extent of corrosion of carbon steel, the SEM micrographs of the surface are examined.

DOI: 10.17628/ecb.2012.1.150-157

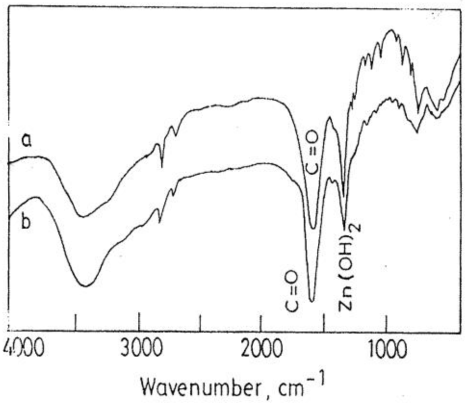

Figure 4. FTIR Spectra. a - Pure TSC; b- Film formed on surface of metal after immersion in well water + TSC(50ppm) + Zn^{2+}(25ppm)

The SEM images of different magnification (X500, X1000) of carbon steel specimen immersed in the well water for 1 day in the absence and presence of inhibitor system are shown in Fig 5 .

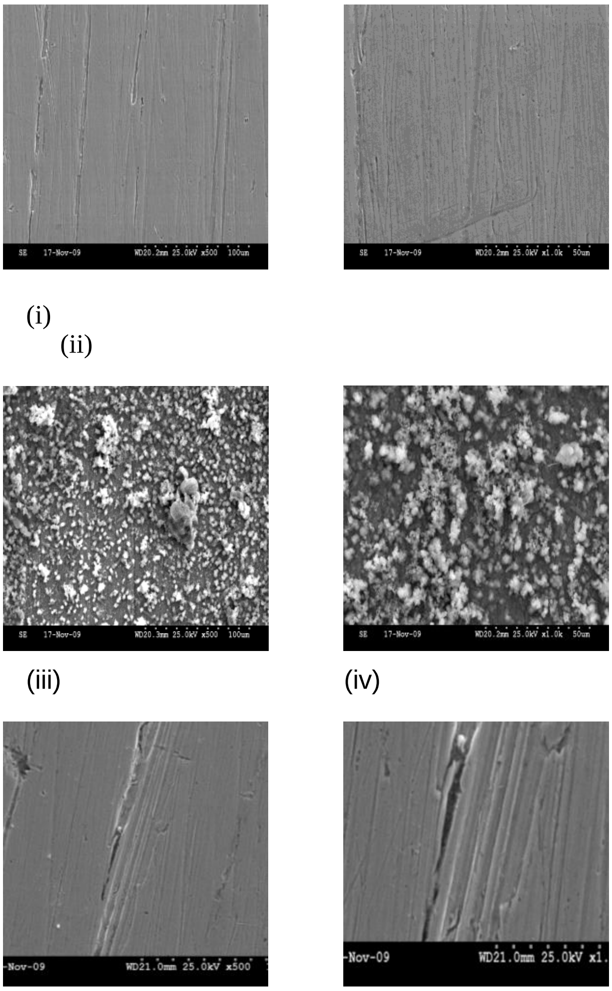

(i)
(ii)

(iii) (iv)

Figure 5. SEM micrographs: Carbon steel (control), magnification – x500 (i), x1000 (ii); Carbon steel immersed in well water, magnification –x500 (iii), x1000 (iv); Carbon steel immersed in well water containing TSC (50 ppm)+ Zn^{2+} (25 ppm), magnification - x500 (v), x1000 (vi).

The SEM micrographs of polished carbon steel surface (control) in Fig 5.i and ii show the smooth surface of the metal. This shows the absence of any corrosion products or inhibitors complex formed on the metal surface.

The SEM micrographs of carbon steel surface immersed in well water in Fig 5 iii & iv shows the roughness of the metal surface which indicates the corrosion of carbon steel in well water. Fig.5 v & vi shows the SEM micrographs of the metal surface immersed in well water containing 50 ppm of TSC, 25 ppm of Zn^{2+} creates a thin protective film, which inhibits carbon steel dissolution.

3.8. Atomic Force Microscopy Characterization

Atomic force microscopy (AFM) is a powerful technique for the gathering of roughness statistics from a variety of surface.[18] AFM is becoming an accepted method of roughness investigation.[19-23]

All atomic force microscopy images were obtained on a Veeco di Innova AFM instrument operating in tapping mode in air. The scan sizes of all the AFM images are 5μm x 5μm areas at a scan rate of 2.4 lines per second.

The two dimensional (2D), three dimensional (3D) AFM morphologies and the AFM cross-sectional profile for polished carbon steel surface (reference sample), carbon steel surface immersed in well water (blank sample) and carbon steel surface immersed in well water containing the formulation of 150 ppm of TSC and 25 ppm of Zn^{2+} are shown in Fig 6 (a,d,g), (b,e,h), (c,f,i) respectively.

Root-mean-square roughness, average roughness and peak-to-valley value

AFM image analysis was performed to obtain the average roughness, R_a (the average deviation of all points roughness profile from a mean line over the evaluation length), root-mean-square roughness, R_q (the average of the measured height deviations taken within the evaluation length and measured form the mean line) and the maximum peak-to-valley (P-V) height values (largest single peak-to-valley height in five adjoining sampling heights [24]. R_q is much more sensitive than R_a to large and small height deviations from the mean [25].

Table 7 is the summary of the average roughness (R_a), rms roughness (R_q) maximum peak-to-valley height (P-V) value for carbon steel surface immersed in different environments.

The values of R_q,R_a and P-V height for the polished carbon steel surface (reference sample) are 3.50 nm, 2.211nm and 22.0nm respectively, which shows a more homogeneous surface, with some places in where the height is lower than the average depth [18]. Fig.6. (a,d,g) displays the uncorroded metal surface. The slight roughness observed on the polished carbon steel surface is due to atmospheric corrosion.

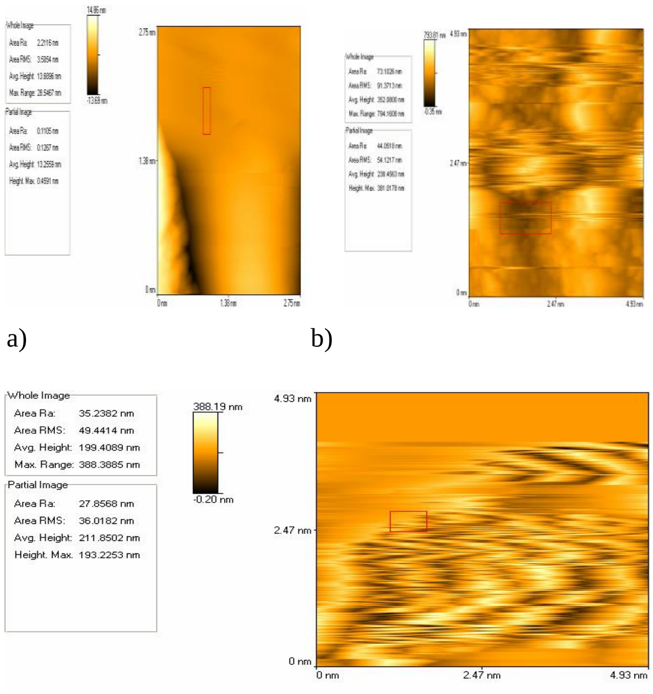

a) b)

c)

Figure 6. 2D AFM images of the surface of polished carbon steel (control) (a); Carbon steel immersed in well water (blank) (b); Carbon steel immersed in well water containing TSC (50 ppm) + Zn^{2+} (25ppm) (c)

The rms roughness, average roughness and P-V height values for the carbon steel surface immersed in well water are 91.37 nm, 73.10 nm and 411.9 nm respectively. These data suggest that carbon steel surface immersed in well water has a greater surface roughness than the polished metal surface, which shows that the unprotected carbon steel surface is rougher and was due to the corrosion of the carbon steel in well water environment. Fig. 6 (b,e,h) displays corroded metal surface with few pits.

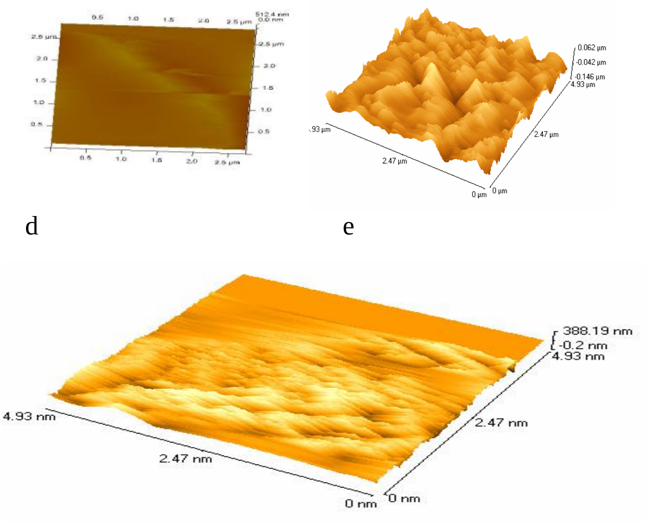

d e

f

Figure 6. 3D AFM images of the surface of polished carbon steel (control) (d); Carbon steel immersed in well water (blank) (e); Carbon steel immersed in well water containing TSC (50 ppm) + Zn^{2+} (25ppm) (h)

The presence of 150 ppm of TSC and 25 ppm of Zn^{2+} in the well water environment reduces the Rq by a factor of 49.44nm from 91.37 nm and the average roughness is significantly reduced to 35.24 nm when compared with 73.10 nm of carbon steel surface immersed in well water. The maximum peak-to-valley height also was reduced to 190.0 nm. These parameters confirm that the surface appears smoother. The smoothness of the surface is due to the formation of a compact protective film of Fe^{2+} -TSC complex and $Zn(OH)_2$ on the metals surface thereby inhibiting the corrosion of carbon steel.

Also the above parameters observed for carbon steel immersed in well water are somewhat greater than the AFM data of polished metal surface which confirms the formation of the film on the metal surface, which is protective in nature.

Table .7 AFM data for carbon steel surface immersed in inhibited and uninhibited environments

Samples	RMS (R_q) Roughness (nm)	Average Roughness (R_a) (nm)	Maximum peak-to-valley height (nm)
Polished carbon Steel (control)	3.50	2.211	22
Carbon steel immersed in well water (blank)	91.37	73.10	411.9
Carbon steel immersed in well water containing TSC (50 ppm) + Zn^{2+} (25ppm)	49.44	35.24	190.0

3.9. Effect of TSC – Zn^{2+} formulation on the biocidal efficiency of CTAB

The influence of TSC-Fe^{2+} system on the biocidal efficiency of CTAB is shown in Table 8. The biocidal efficiency of TSC – Fe^{2+} system in the absence of CTAB is found to be 8 percent. The number of colony forming units/ml is 424 x 10^3, which is objectionable. When 200 ppm of CTAB is added, nil CFμ/ml is obtained. The biocidal efficiency is 100%. Hence the optimum concentration of CTAB is 200 ppm. Thus it is seen in Table 8, that the formulation consisting of 50ppm of TSC, 25ppm of Zn^{2+} and 200 ppm of CTAB has 49% of corrosion inhibition efficiency and 100% of biocidal efficiency

3.10. Effect of TSC –Zn^{2+} formulation on the biocidal efficiency of SDS

The biocidal efficiency of TSC –Zn^{2+} in the absence of SDS was found to be 7 percent. The number of colony forming units/ml was 429x 10^3 this is objectionable. When 200 ppm of SDS was added , nil CFμ/ml was obtained. The biocidal efficiency was 100%. Hence the optimum concentrations of SDS are 200 ppm. Thus it was seen from the Table 9 that the formulation consisting of 50 ppm of TSC, 25 ppm of Zn^{2+} and 150 ppm of SDS has 44 percent corrosion inhibition and 100% biocidal efficiency.

DOI: 10.17628/ecb.2012.1.150-157

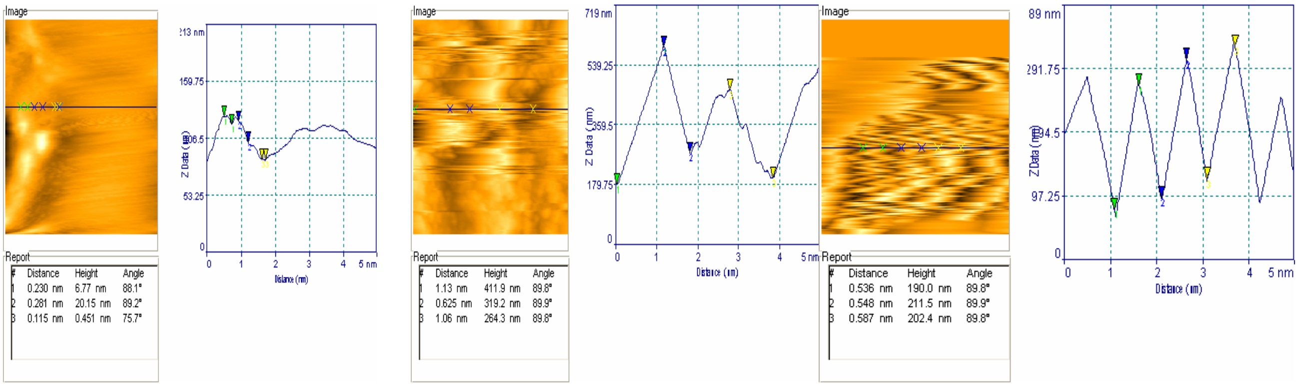

g h i

Figure 6. The cross-sectional profiles, which are corresponding to as shown broken lines in AFM images of the surface of polished carbon steel (control) (g); carbon steel immersed in well water (blank) (h); carbon steel immersed in well water containing TSC (50 ppm) + Zn^{2+} (25ppm) (i)

Table 8. The corrosion inhibition efficiency and the biocidal efficiency of the TSC– Zn2+ - CTAB system

TSC, ppm	Zn^{2+}, ppm	CTAB, ppm	IE, %	CR, mdd	Clony corming units/ml	Biocidal efficiency, %
0	0	0	--	23.64	460 x 10^3	--
50	25	0	70	7.09	424 x 10^3	8
50	25	50	64	8.51	360 x 10^3	22
50	25	100	59	9.69	242 x 10^3	47
50	25	150	53	11.11	89 x 10^3	81
50	25	200	49	12.10	Nil	100
50	25	250	45	13.00	Nil	100

Table 9. The corrosion inhibition efficiency and the biocidal efficiency of the TSC – Zn^{2+} - SDS system

TSC, ppm	Zn^{2+}, ppm	SDS, ppm	IE, %	CR, mdd	Clony corming Units/ml	Biocidal Efficiency, %
0	0	0	--	23.64	460 x 10^3	--
50	25	0	70	7.10	429 x 10^3	7
50	25	50	61	9.22	369 x 10^3	20
50	25	100	55	10.64	245 x 10^3	47
50	25	150	49	12.10	90 x 10^3	80
50	25	200	44	13.24	Nil	100
50	25	250	40	14.18	Nil	100

REFERENCES

[1] Ghareba S., Omanovic, S. *Electrochim. Acta*, **2011**, *56*, 3890.

[2] Shi, H. W., Han, E. H., Liu, F. C., *Corr. Sci.* **2011,** *53*, 2374.

[3] Lowmunkhong, P., Ungthararak, D., Sutthivaiyakit, P., *Corr. Sci.*, **2010**, *52*, 30.

[4] Gece, G., Bilgiç, S., *Corr. Sci. 2010,* 52, 3435.

[5] Qiong Deng, Hong-Wei Shi, Na-Na Ding, Bao-Qin Chen, Xiao-Peng He, Guixia Liu, Yun Tang, Yi-Tao Long, Guo-Rong Chen, Corrosion Science, Volume 57, April 2012, Pages 220-227

[6] Garcia-Arriaga, V. Alvarez-Ramirez, J. Amaya, M. Sosa, E. *Corr. Sci.*, **2010**, *52*, 2268.

[7] Quartarone, G. Battilana, M. Bonaldo, L. Tortato, T. *Corr. Sci.*, **2008**, *50*, 3467.

[8] Mohammed A. A., Abd El Rehim, S. S., Abdel-Fatah, H. T. M., *Corr. Sci.* **2009**, *51*, 882.

[9] Lebrini, M. Fontaine, G. Gengembre, L. Traisnel, M. Lerasle, O. Genet, N., *Corr. Sci.* **2009**, *51*, 1201.

[10] Khaled, K.F. *Corr. Sci.*, **2010**, *52*, 3225.

[11] Galal, A. Atta, N.F. Al-Hassan, M.H.S. *Mater. Chem. Phys.*, **2005**, *89*(1), 28.

[12] Ein-Eli, Y. Auinat, M. 2005 Meeting Abstracts, (MA) **2005**, 584.

[13] Saleh, R.M. Shams El Din, A.M. *Corr. Sci.*, **1972**, *12*(9), 689.

[14] Amin, M. A., Khaled, K. F., *Corr. Sci.*, **2010**, *52*, 1194.

DOI: 10.17628/ecb.2012.1.150-157

[15] Eddy, N. O. *J. Advanced Res.*, **2011**, *2*, 35.

[16] Singh, S.K. Mukherjee, A.K., *J. Mater. Sci. Technol.*, **2010,** *26*, 264.

[17] Amin, M. A., Ibrahim, M. A. *Corr. Sci.*, **2011**, *53*, 873.

[18] Avci, G. *Colloid and Surfaces A: Physicochem. Eng. Aspects*, **2008**, *317*, 730.

[19] Lua, Z. L., Qiua, Y. B. and Guo, X. P. *Acta Phys-Chim. Sinica*, **2008**, *24*, 243.

[20] Quartarone G., Bonaldoa L. and Tortatoa, C. *Appl. Surface Sci.*, **2006**, *252*, 8251.

[21] Kern P. and Landolt D. *Corr. Sci.*, **2002**, *44*, 1809.

[22] Bilgiç, S. *Mater. Chem. Phys.*, **2002**, *76*, 52.

[23] Kern P. and Landolt, D. *Electrochim. Acta*, **2001**, *47*(4), 589.

[24] Agarwal P. and Landolt, D. *Corr. Sci.* **1998**, *40*(4-5) 673.

[25] Kálmán, E. Kármán, F. H. Telegdi, J. Várhegyi, B. Balla J. and Kiss, T. *Corr. Sci.* **1993,** *35*(5-8), 1477.

[26] Yurt, A. Bereket G. and Ogretir, C. *J. Mol. Struct. THEOCHEM*, **2005**, *725*(1-3), 215.

[27] Spah, M., Spah, D. C., Deshwal, B., Lee, S. M., Chae, Y. K. and Park, J. W., *Corr. Sci.*, **2009**, *51*(6), 1293.

[28] Sagoe-Crentsil, K.K. Yilmaz V.T. and Glasser F. P. *Cement Concrete Res.*, **1993**, *23*(6), 1380.

[29] Hassan, H. H. *Electrochim. Acta*, **2005**, *51*(3), 526.

[30] Torchio, S *Corr. Sci.*, **1991**, *32*(12), 1377.

Received: 28. 08. 2012.

Accepted: 06.09.2012.

DOI: 10.17628/ecb.2012.1.150-157

SYNTHESIS OF SEC-BUTANOL FROM n-BUTENES AND WATER WITH MOLECULAR SIEVE CATALYSTS

Zhang Yongmei,[a] and You Hongjun[b]

Keywords: sec-butanol; molecular sieve; synthesis; n-butenes; reaction condition

Using n-butenes and water as feedstocks and molecular sieves as catalysts, effects of the reaction temperature, the reaction pressure, the weight hour space velocity (WHSV), and the ratio of water to n-butenes on the conversion of n-butenes were studied. The experimental results showed that the optimal reaction temperature, the pressure, the WHSV, and the ratio of water to n-butenes were 180 °C, 8.0 MPa, 0.2 h^{-1}, and 8, respectively; the single conversion of n-butenes and the selectivity of 2-butanol formation were found to be 35.52% and 99%, respectively.

* Corresponding Author
Fax: 1-403-777-6272
E-Mail: youhongjun@hotmail.com
[a] Liaoning Shihua University, Fushun, Liaoning, P.R. China.
[b] SAIT Polytechnic, Calgary AB, Canada.

Introduction

n-Butenes are basic petrochemical and organic chemical products and due to their high combustion heat they are frequently burnt as fuel. The use of n-butenes as feedstocks improves the efficiency of raw material utilization and increases the economic income of a chemical plant.[1]

The preparation of 2-butanol from n-butenes and water is a well known process, which is catalysed by sulphuric acid,[2] strongly acidic ion-exchanger resins,[3] or heteropolyacids.[4]

Indirect hydration with sulphuric acid as catalyst can be described as follows. The reactor is a kind of tower, and the process consists of four steps, such as esterification, hydrolysis, fractionation, and dilution of sulphuric acid. Sec-butyl ether by-product formation occurred. When an industrial C_4 fraction containing n-butenes were pre-treated with 80% sulphuric acid[5], the butyl sulphate produced was transformed into 2-butanol via hydrolysis and fractionation. The advantages of the method were that the content of n-butenes was not limited, and the reaction conditions were mild and could be easily controlled. The main disadvantages were that the equipment was seriously corroded, thus requiring more investment, and large amount of sulphuric acid and alkaline material for its neutralization were required.

The ion-exchange resin catalyzed direct hydration reaction conditions were as follows: the reactor was a kind of cylinder which included the solid sulfonic acid resin catalysts. The life cycle of the catalyst was about one year. The process could be performed in a simple way, no corrosion of the equipment was observed. The main disadvantage of the method was that high content of n-butenes was required in the input stream and the single yield of 2-butanol was very low (less than 10%).

Heteropolyacid catalyzed direct hydration was peformed in the following way using the unit built in 1985: the reactor was a vertical stirred cylinder in which the catalyst was a mixture of molybdate and organic metal-containing additive. The optimal reaction temperature, pressure, single conversion of n-butenes, and selectivity for 2-butanol were found to be 200–230 °C, 19.0 MPa, 25–30%, and more than 97%, respectively. n-Butenes were proved to be not only simple reactants but also supercritical extracting agents. The efficiency of the reaction was very high, but the reaction required relatively high pressure.

In this paper, the reaction of n-butenes and water on molecular sieves as catalysts was studied. Effects of the reaction temperature, the pressure, and the WHSV, and the ratio of water to n-butenes on the conversion of n-butenes were determined. Experimental results indicated that the conversion of n-butenes and the selectivity for 2-butanol were higher and better than that of other methods.

Experimental section

Feedstock

n-Butenes were obtained from Fushun Ethylene Chemical Plant. The compositions of n-butenes used are shown in Table 1.

Table 1. Compositions of n-butenes

Components	C_2	$C_3^=$	C_3^0	iC_4^0	nC_4^0	$nC_4^=$
Composition, % m/m	0.14	0.17	0.04	0.06	0.15	99.44

Catalyst

Properties of the applied modified molecular sieve catalyst are presented in Table 2.

Table 2. Properties of molecular sieve catalyst

Particle size, mm	Length, mm	Stacking density, g*cm^{-3}	Intensity, kg*mm^{-1}
1.5~1.8	5~9	0.671	>10

Reaction principle

2-Butanol can be produced from n-butenes and water using molecular sieve as catalyst, according to Eqn. (1) and (2):

$$CH_2=CH-CH_2-CH_3 + H_2O \rightarrow CH_3-CHOH-CH_2-CH_3 \tag{1}$$

$$CH_3-CH=CH-CH_3 + H_2O \rightarrow CH_3-CHOH-CH_2-CH_3 \tag{2}$$

DOI: 10.17628/ecb.2012.1.158-160

Apparatus

n-Butenes and water were pumped into the reactor. When the reaction was completed, the product was separated in a separation tank. The final product and gases were discharged at bottom and top of the tank, respectively. The schematic drawing of the experimental apparatus is shown in Figure 1.

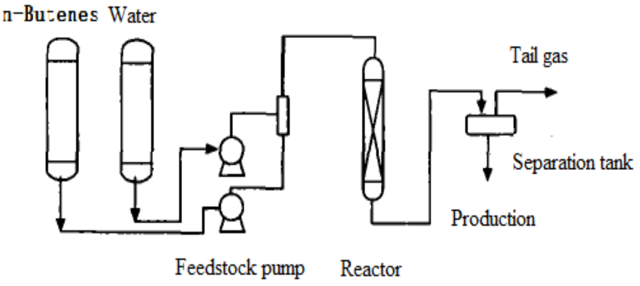

Figure 1. Schematic drawing of the experimental apparatus

Results and discussion

Effects of the reaction pressure and the WHSV on the conversion of n-butenes

Effects of the reaction pressure and the WHSV on the conversion of n-butenes were studied with keeping the reaction temperature and the ratio of water to n-butenes at values of 180 °C and 8, respectively.

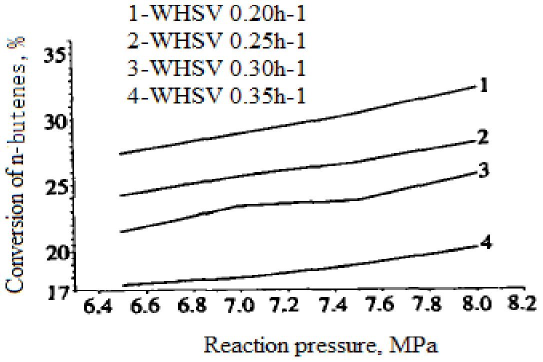

Figure 2. The relationship between the pressure, the WHSV, and the conversion of n-butenes

Figure 2 shows the relationship between the pressure, the WHSV, and the conversion of n-butenes. The conversion of n-butenes at the same WHSV increased with the increase of the reaction pressure, but the conversion of n-butenes at the same reaction pressure decreased with the increase of the same WHSV. The maximal conversion of n-butenes could be obtained at 8.0 MPa pressure and 0.2 h^{-1} weight hour space velocity.

Effects of the reaction temperature and the WHSV on the conversion of n-butenes

Effects of the reaction temperature and the WHSV on the conversion of n-butenes were studied at 8.0 MPa pressure and at the ratio of water to n-butenes of 8.

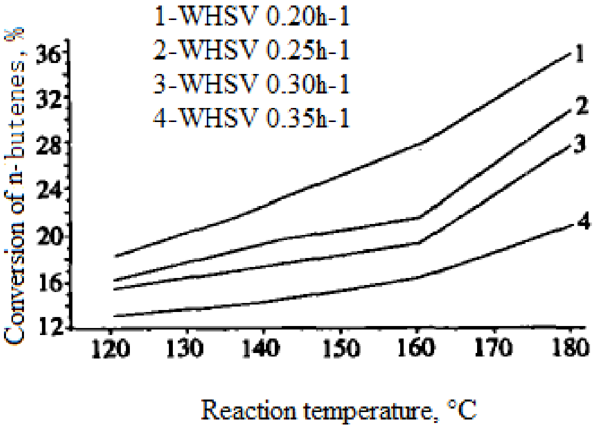

Figure 3. The relationship between the temperature, the WHSV, and the conversion of n-butenes

Figure 3 shows the relationship between the reaction temperature, the WHSV, and the conversion of n-butenes. The conversion of n-butenes at the same WHSV increased with the increase of the reaction temperature, but the conversion of n-butenes at the same reaction temperature decreased with the increase of the same WHSV. The conversion of n-butenes had a maximum value when the reaction temperature and the WHSV were 180 °C and 0.2 h^{-1}, respectively.

Effects of the ratio of water to n-butene and the WHSV on the conversion of n-butenes

The reaction pressure and the reaction temperature in these experiments were 8.0 MPa and 8, respectively. Effects of the ratio of water to n-butenes and the WHSV on the conversion of n-butenes were studied.

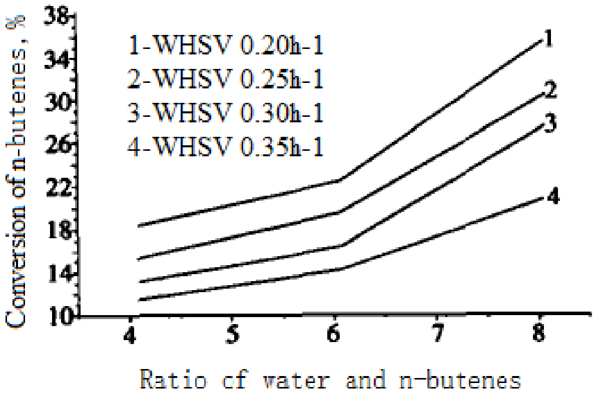

Figure 4. The relationship between the ratio of water to n-butene, WHSV, and the conversion of n-butenes

Figure 4 shows the relationships between the ratio of water to n-butenes, the WHSV, and the conversion of n-butenes. The conversion of n-butenes at the same WHSV increased with the increase of the ratio of water to n-butenes, but the conversion of n-butenes at the same ratio of water to n-butenes decreased with the increase of the same WHSV. The conversion of n-butenes had a maximum value when the ratio of water to n-butenes and the WHSV were 8 and 0.2 h^{-1}, respectively.

Based on experimental data, the regression resulted in a three-variable equation, which can be written as follows:

$$\varphi, \% = A + BX_1 + CX_3 + DX_1X_2 + EX_2^2 \qquad (3)$$

where φ - the conversion of butanes, in %,

X_1 - the pressure, MPa,

X_2 - the ratio of water to n-butenes

X_3- the WHSV, h^{-1}.

A= –159.08

B= 33.88

C=0.64

D=332.89

E=15960.52

Conclusion

Using water and n-butenes as feedstocks and molecular sieves as catalysts, effects of the reaction temperature, the pressure, the WHSV, and the water/n-butenes ratio on the conversion of n-butenes were studied. The experimental results obtained are as follows:

(1) The conversion of n-butenes at the same WHSV increased with the increase of the reaction temperature, the pressure, and the water/n-butenes ratio.

(2) The conversion of n-butenes at the same reaction temperature, the same reaction pressure, and the same water/ n-butenes ratio decreased with the increase of the WHSV**.**

(3) Molecular sieve catalysts exhibit high activity and conversion efficiency in the n-butene water reaction. Good economic and social benefits can be obtained using this type of molecular sieve catalysts in the reaction of n-butenes with water.

References

[1] Fang, D. R., Jiang, X. M., .Wang, Z. Y., Qiu, Z. P. and Zhang, H. M. *Petrochem. Technol.*, **2011**, *1*, 49-54.

[2] Shan, H. Y and Yong, B. *J. Jilin Univ.*, **2011**, *3*, 540.

[3] Ma, J. and Zhu, N. *Chin. J. App. Chem.*, **2011**, *12*. 1397.

[4] Li, B. and Kang, L. J. *Chem. Intermed.*, **2011**, *3*. 58.

[5] Ma, H. W., Fang, M. and You, H. J. *Liaoning Ind. Chem.*, **2003**, *5*, 199.

Received: 27.08.2012.

Accepted: 09.09.2012.

UTILIZATION OF ENVIRONMENTAL WASTE MATERIALS (COAL FLY ASH AND *PROSOPIS JULIFLORA* CARBON) IN THE REMOVAL OF CHROMIUM, LEAD, ZINC AND COPPER FROM INDUSTRIAL EFFLUENTS

K.K. Sivakumar[a] and M.S. Dheenadayalan[b]

Keywords: Adsorption, heavy metal, fly ash, effluent treatment

Waste materials such as coal fly ash generated from power plant in India and environmental threat causing plant such as *Prosopis juliflora* has been converted into a cheap potential adsorbent. This has been characterized and utilized for the removal of chromium, lead, zinc and copper from synthetic and actual wastewater. The sorption efficiency decreases with increase in pH. Adsorption of chromium, lead, copper and zinc on Coal Fly ash (CFA) and *Prosopis Juliflora* Carbon (PJC) individually and 50:50 mixture of CFA and PJC follows the Freundlich adsorption isotherm and these have been used to obtain the thermodynamic parameters of the process. The sorption capacity of these adsorbents for the heavy metal removal is found to be better alternative comparable to other low cost adsorbents.

* Corresponding Authors
E-Mail: sivakumarccet@gmail.com
[a] Department of Chemistry, Chettinad College of Engineering & Technology, Karur-639 114. Tamil Nadu, INDIA
[b] PG and Research Department of Chemistry, GTN Arts College, Dindigul. Tamil Nadu, INDIA

Introduction

Toxic metal is defined as that metal, which is neither essential nor has beneficial effect, on the contrary, it displays severe toxicological symptoms at low levels. With increasing industrialization, more and more metals are entering into the environment.[1] These metals stay permanently because they cannot be degraded from the environment. They pass into the food and they ultimately make their passage into the tissue.

Cr(III) is a very stable oxidation state for chromium. In this state, the chromium is labile and kinetically very slow to react or form complexes. It is not a strong oxidizer and the human's natural body acidity is enough for the chromium to keep as Cr(III) state. Chromium enters the air, water and soil mostly in the form of chromium(III) and chromium(VI). Chromium(III) is an essential nutrient that helps the body use sugar, protein, and fat.

Cr(VI) is not a very stable state when compared to Cr (III). The Cr(VI) is a very strong oxidizing agent and likely to form complexes. Breathing high level can cause irritation to the nose, such as runny nose, nosebleeds, ulcers and holes in the nasal septum. Ingesting large amounts can cause stomach upsets and ulcers, convulsions, kidney and liver damage and even death.

The main reason for which Cr(VI) is so toxic is that one of the reduction products of Cr(VI) is Cr(V). Chromium(V) is a known carcinogen and will lodge in any tissue to form cancerous growths. There are reports that chromium(V) is also a factor leading to premature senility in parts of Russia. In the body, the acidity and action of enzymes on Cr(VI) will promote the formation in small quantities of Cr(V). However, as the size of this is normally too large to be adopted by a tissue, the Cr (V) will pass out. The only place where the Cr (V) is likely to lodge is in some of the fine capillaries in the kidneys, intestines or lungs.

Lead is a poisonous metal that can damage nervous connections (especially in young children) and cause blood and brain disorders. Lead poisoning typically results from ingestion of food or water contaminated with lead; but may also occur after accidental ingestion of contaminated soil, dust, or lead based paint and textiles. Long-term exposure can cause nephropathy and colic-like abdominal pains. The main target for lead toxicity is the nervous system, both in adults and children. It may also cause weakness in fingers, wrists, or ankles. Lead exposure also causes small increases in blood pressure, particularly in middle-aged and older people and can cause anaemia. Exposure to high lead levels can severely damage the brain and kidneys in adults or children and ultimately cause death. In pregnant women, high levels of exposure to lead may cause miscarriage.

Copper exposure in high level builds up first in the liver and disrupts the liver's ability to detoxify the blood in general. It can give rise to many psychological imbalances such as mood swings, depression, mental agitation, feeling over-stimulated, restlessness, anxiety, insomnia and a racing mind with too many thoughts are all hallmarks of elevated copper toxicity.

Acute toxicity of zinc may result in sweet taste, throat dryness, cough, weakness, generalized aching, chills, fever, nausea and vomiting. Eating large amounts of zinc, even for a short time, can cause stomach cramps, nausea, and vomiting. The proposed limit of zinc in drinking water is 5 ppm as proposed by FDA.

Coal Fly ash (CFA) and Prosopis Juliflora Carbon (PJC) is used as adsorbent for Cr^{6+}, Pb^{2+}, Cu^{2+} and Zn^{2+} removal from aqueous solution. Chromium, lead, copper and zinc and its compounds are widely used in many industries such as metal finishing, dyes, pigments, inks, glass, ceramics,

DOI: 10.17628/ecb.2012.1.161-167

chromium tanning, textile dyeing and wood preserving industries and certain glue. The effluent from textile dyeing and bleaching industries contain hexavalent chromium concentrations ranging from 0.2 to 0.3, divalent lead concentrations ranging from 0.2 to 1.9 mg L^{-1}, divalent copper concentrations ranging from 2.2 to 4.5 mg L^{-1} and divalent zinc concentration ranging from 6.1 to 11.2 mg L^{-1}. Both Chromium and lead is considered by IARC as a powerful carcinogenic agent that modifies the DNA transcription process causing important chromosomic aberrations. The USEPA recommends that the levels of Cr(VI) in drinking is allowed up to 0.05 mg L^{-1}, Pb(II) in drinking water should be 0.05 mg L^{-1}, copper in drinking water is allowed up to 0.05 mg L^{-1} and zinc in drinking water is allowed up to 0.5 mg L^{-1}. Consequently, the removal of these ions from industrial wastewater has become a research topic of great interest.[2]

Scope of the study

Several methods such as chemical precipitation, ion exchange, electrochemical precipitation, solvent extraction, reverse osmosis, etc. These methods are cost intensive and are unaffordable for large scale treatment of wastewater that is rich in Cr (VI), Pb (II), Cu (II) and Zn (II) especially to developing countries like India.[3] Adsorption using the activated carbon is an effective method for the treatment of industrial effluents contaminated with Cr (VI), Pb (II), Cu (II) and Zn (II), moreover is quite popular as compared to other methods. The cost associated with the commercial activated carbon is very high which make the adsorption process expensive. This indicates that the cost effective alternate adsorbents for the treatment of Cr (VI), Pb (II), Cu (II) and Zn (II) contaminated waste streams are needed at present.[4]

Aim and objectives

Power plant waste product such as coal fly ash and indigenous carbon prepared from eco-hate prosopis juliflora is used as an adsorbent for the removal of Cr(VI), Pb(II), Cu(II) and Zn(II) from wastewater. Batch experiments are carried out for kinetic studies on the removal of Cr(VI), Pb(II), Cu(II) and Zn(II) from aqueous solution. Heavy metal contamination exists in aqueous wastes of many industries, such as metal plating, mining operations, tanneries, chloralkali, radiator manufacturing, smelting, alloy industries and storage batteries industries, etc. The effects of various influencing parameters such as initial pH, contact time, dose of adsorbent and initial concentration of adsorbate are studied. The equilibrium isotherm data and kinetic data are tested with various isotherm models and kinetic models.[5-7]

Experimental materials

Preparation of adsorbent (Fly ash)

The fly ash used in this study is collected from National Thermal Power Corporation (NTPC), Ramagundum, AP. The fly ash is washed with distilled water and then activation is carried out by treating it with concentrated sulphuric acid (98 % w/w) in 1:1 weight ratio and is kept in an oven maintained at a temperature range of 150 ºC for 12 hours. Again it is washed with distilled water to remove the free acid and finally dried at 110 ºC for 5 hours.

Preparation of adsorbent (*Prosopis Juliflora* Carbon)

The *Prosopis Juliflora* wood used in this study is collected from in and around of Virdhunagar District, Tamil Nadu. The process of activation is carried out in two stages. Firstly the *Prosopis Juliflora* wood is converted into wooden charcoal by carbonization process which is usually carried out in mud-pits, brick kilns and metallic portable kilns. Secondly wood charcoal is activated by treating it with concentrated sulphuric acid at a temperature of 150 ºC for about 12 hours in an oven. The chemical activation takes place at the internal surface area, creating more sites for adsorption.

Characterization of adsorbents

The physicochemical characteristics like moisture content, particle density, ash content and water soluble components of adsorbents such as activated coal fly ash and activated prosopis juliflora carbon were determined and given in Table 1.

Table 1. Parameters for CFA and PJC

Parameters	CFA	PJC
pH	6.1	5.9
Bulk density (g/cc)	0.96	0.97
Moisture (%)	26	8
Ash (%)	70	24

The bulk density and particle density affect the adsorption of metal ions. The decrease in the bulk density enhances the adsorption of metals ions. The adsorption process will be higher if the size of the adsorbent is fine. The bulk density value less than 1.2 indicates the adsorbent materials are fine nature. When this value falls within the range of 1.2-2 the materials are medium and the value more than 2 indicates that the materials are coarse in nature. The particle density value is less than 2.2, which indicates the materials are finer, the value between 2.2-4 are medium and more than 4 indicates materials are coarse in nature. In the present study, the bulk density and particle density values obtained are closer to fine in nature.

Moisture content, though does not affect the adsorption power, dilutes the adsorbents and therefore necessitates the use of additional weight of adsorbents to provide the required weight. Ash content generally gives an idea about inorganic constituents associated with carbon. In any case, the actual amount of individual inorganic constituents will vary from one type to another as they are mainly derived from different source of material. The values of matter soluble in water and acid are more informative for designing the adsorption process.

DOI: 10.17628/ecb.2012.1.161-167

Other Chemicals

All other chemicals used are of analytical reagent grade and were obtained from Loba and Glaxo/BDH, Buffer solutions of pH equal to 4, 7 and 9 for calibration of the pH meter, concentrated nitric acid, individual standard solution for Cr(VI) ion, individual standard solution for Pb(II) ion, individual standard solution for Cu(II) ion, individual standard solution for Zn(II) ion, sodium hydroxide pellets, sodium nitrate and 0.5 N hydrochloric acid.

Chemical analysis

The test methods cover the determination of dissolved and total recoverable chromium, lead, copper and zinc in water and waste water by atomic-absorption spectrophotometry. The reason to choose the AAS is the results produced are reproducible and accurate and moreover applicable to industrial discharges which may contain less than 10 mg L^{-1} of any heavy metal.

In atomic absorption a sample is aspired into a flame and atomized. A light beam is directed through the flame into a monochromator, and onto a detector that measures the amount of light absorbed by the atomized element in the flame. For some metals, atomic absorption exhibits superior sensitivity over flame emission. Because each element has its own characteristic absorption wavelength, a source lamp composed of that element is used, which is called the Hollow Cathode Lamp. This makes the method relatively free from spectral or radiation interference. The amount of energy at the characteristic wavelength absorbed in the flame is proportional to the concentration of the element in the sample over a limited concentration range. The instrument used in determination of heavy metals is the Atomic Absorption Spectrophotometer Perkin-Elmer Model 403 equipped with a Honeywell Electronik 193 strip chart recorder. The method used for the determination of heavy metals was (Direct Air- Acetylene Flame Method).

In case of the hexavalent chromium, the absorption of the color complex measured at a wavelength of 540 nm, the divalent lead, the absorption of the color complex measured at a wavelength of 283.3 nm, the divalent copper, the absorption of the color complex measured at a wavelength of 324.7 nm and the divalent zinc, the absorption of the color complex measured at a wavelength of 213.8 nm.

Batch experiments

The batch experiments are carried out in 250 mL borosil shaker bottles by shaking a pre weighed amount of the CFA, PJC and 50:50 mixture of CFA and PJC with 100 mL of the aqueous solutions for a pre determined period (found out from the kinetic studies) at 30ºC with an initial adsorbate concentration of 100 mg L^{-1} and an adsorbent of 10 g L^{-1}. The effect of adsorbent amount is studied by varying it in the range of 10 to 50 g L^{-1} with the adsorbate concentration range of 5 to 25 mg L^{-1} at 30ºC. The effect of pH of adsorbate on adsorption is studied by varying it in the range of acidic 2 to alkaline 12. Moreover the effect of contact time between adsorbate and adsorbent is studied by varying it in the range of 15 to 180 minutes.

The various experimental parameters which influence the process are as follows:

(i) Effect of varying the concentration of dyes

(ii) Effect of varying the pH of the solution

(iii) Effect of varying the amount of photocatalyst

(iv) Effect of varying the contact time

Effect of varying the concentration

The effect of initial concentration of Cr(VI), Pb(II), Cu(II) and Zn(II) on the amount of CFA, PJC and 50:50 mixture was studied with a fixed dose of adsorbent (10 g L^{-1}) and constant contact time (60 min) by varying the initial concentration of above adsorbate. From the experimental results, it is found that the amount of adsorbate adsorbed exponentially increases while the percentage removal decreases with the increase in initial concentration of adsorbate. This indicates that there exists a reduction in immediate solute adsorption due to the lack of available active sites on the adsorbent surface compared to the relatively large number of active sites required for the high initial concentration of adsorbate. Similar results have been reported in literature on the extent of removal of heavy metals by various adsorbent materials. The effect of concentration on the percentage removal of adsorbate is shown in this chapter Fig. 1 to 4.

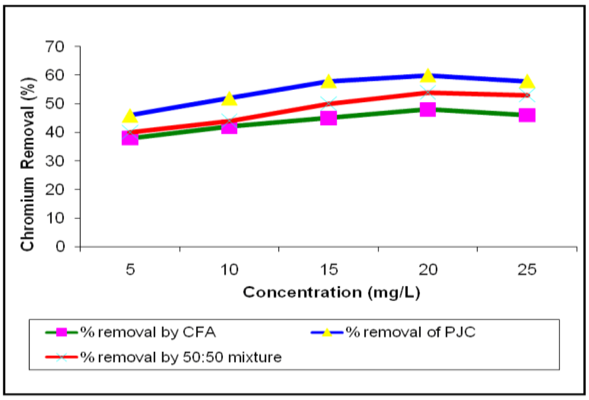

Figure 1. Effect of concentration for Cr removal

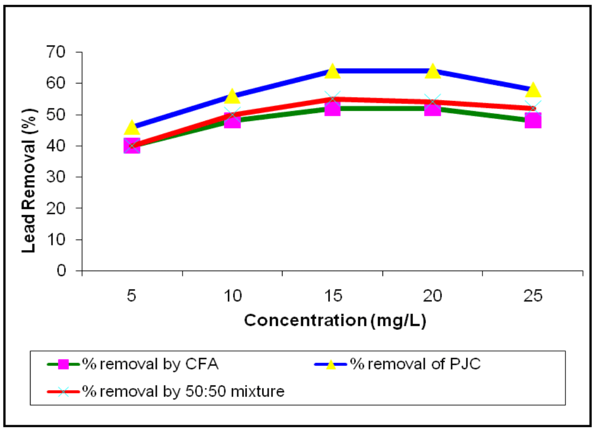

Figure 2. Effect of concentratione for Pb removal

DOI: 10.17628/ecb.2012.1.161-167

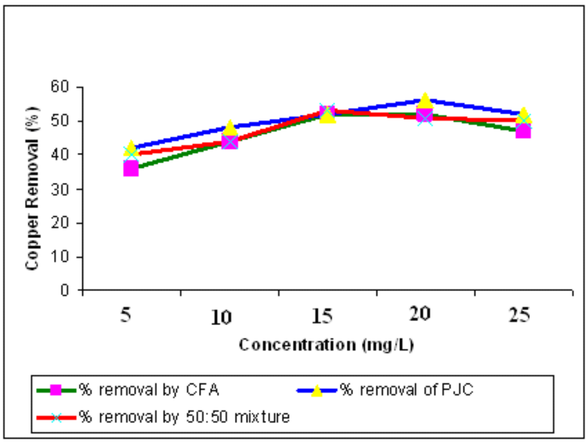

Figure 3. Effect of concentration for Cu removal

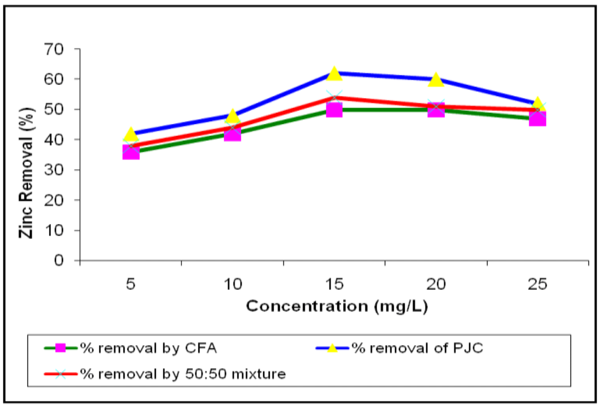

Figure 4. Effect of concentration for Zn removal

The relative adsorption capacity of CFA, PJC and 50:50 mixture also reveals that under identical experimental conditions, compared to CAC, the adsorptive capacities of CFA, PJC and 50:50 mixture are less (Table 2). This may be due to the porous textural nature of the surface of AC. These low cost adsorbents possess nearly 50% adsorptive capacities compared to that of AC. The percentage removal of adsorbate by above mentioned adsorbent is found to exponentially decrease with increase in initial concentration of heavy metal, which may be due to the lack of available active sites on the surface of the adsorbent. The amount of adsorbate adsorbed on an adsorbent increases with increase in initial concentration of heavy metal. The optimum concentration of heavy metals found to be 15-20 ppm.

Table 2. Identical and Optimum removal

Adsorbent	Experimental Condition	
	Identical	Optimum
CFA	48	60
PJC	58	70
50:50 (CFA:PJC) mixture	52	64

Effect of dose of adsorbent

To study the influence of the adsorbent dosage on the removal of heavy metal ions, different values have been taken by varying the adsorbent concentration ranging from 10-50 g L^{-1} by keeping the volume of the effluent solution constant under optimum temperature and contact time.

Figure 5 to 8 shown in this chapter shows the effect of adsorbent dosage on the removal of chromium, lead, copper and zinc by CFA, PJC and 50:50 ratio of CFA: PJC at optimum temperature of 296 K and time 60 min. In case of PJC, chromium removal of 46 % to 60 % achieved with respect to dose of 10 to 50 g L^{-1}, lead removal 46 % to 64 % achieved with respect to dose of 10-50 g L^{-1}, copper removal of 42-56 % achieved with respect to dose of 10-50 g L^{-1} and zinc removal of 42-60 % is achieved with respect to dose of 10-50 g L^{-1}.

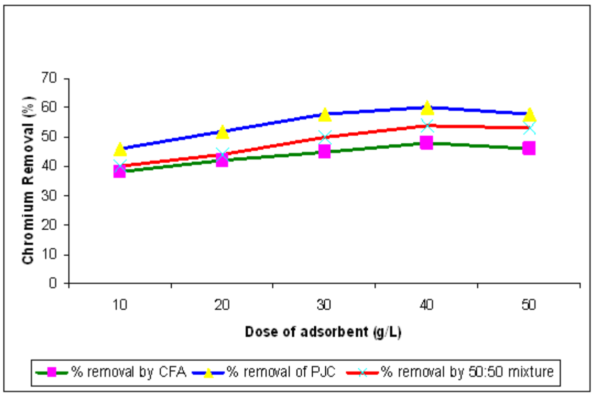

Figure 5. Effect of dose of adsorbent for Cr removal

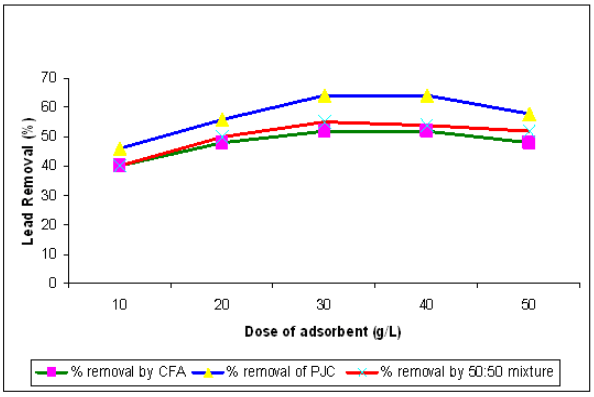

Figure 6. Effect of dose of adsorbent for Pb removal

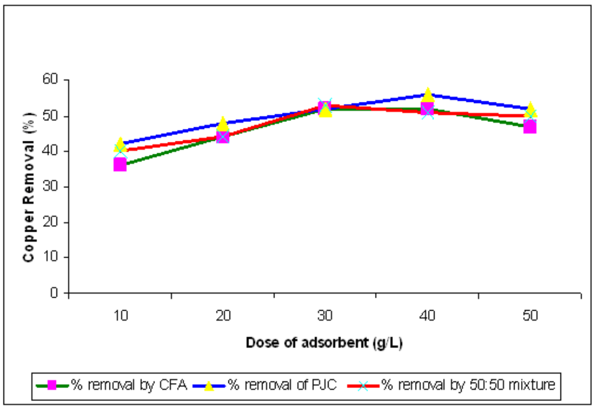

Figure 7. Effect of dose of adsorbent for Cu removal

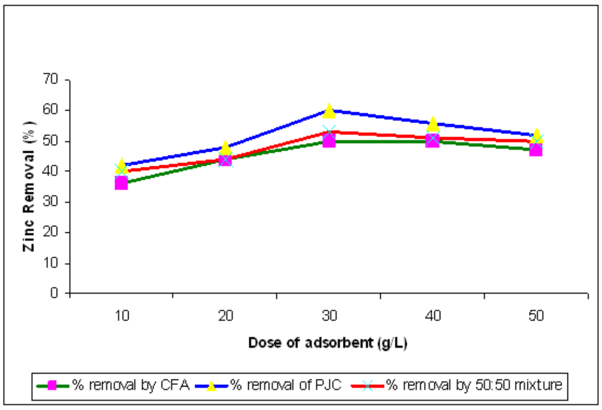

Figure 8. Effect of dose of adsorbent for Zn removal

In case of CFA, chromium removal of 38 % to 48 % achieved with respect to dose of 10 to 50 g L^{-1}, lead removal 40 % to 52 % achieved with respect to dose of 10-50 g L^{-1}, copper removal of 36-52 % achieved with respect to dose of 10-50 g L^{-1} and zinc removal of 36-50 % is achieved with respect to dose of 10-50 g L^{-1}.

But in case of 50:50 mixture, chromium removal of 40 % to 54 % achieved with respect to dose of 10 to 50 g L^{-1}, lead removal 40 % to 55 % achieved with respect to dose of 10-50 g L^{-1}, copper removal of 40-53 % achieved with respect to dose of 10-50 g L^{-1} and zinc removal of 40-53 % is achieved with respect to dose of 10-50 g L^{-1}.

The observation made in this study promotes the extend of removal of heavy metal ions from the textile dye effluent increases with increase in adsorbent dosage. This can be explained by the availability of the exchangeable sites or surface area on the adsorbents.[8] In the minimum adsorbent dosage level (10 g L^{-1}) there will be a low availability of exchangeable sites, ultimately the removal of metal ions at low adsorbent dosage is also minimum. But at the maximum adsorbent dosage level (50 g L^{-1}) there will be a greater availability of exchangeable sites or surface area, hence the removal of metal ions at maximum adsorbent dosage is also maximum.

Success of removal of heavy metal ions with the effect of adsorbent dosage has been evaluated through the study of the percentage of ratio, before and after individual adsorbent dose.

Effect of pH

The effect of pH on the removal of heavy metal ions was studied by varying the pH ranging from 2 to 12 and keeping the concentration of the individual solution and dose of adsorbent are constant under optimum condition of temperature 296 K and time 60 min.

The removal of heavy metals is found to be highly pH dependent. The figure 9 to 12 in this chapter shows that the percentage removal of chromium varies from 20% to 63% for the pH range of 2-10, the percentage removal of lead varies from 18% to 66% for the pH range of 2-10, the percentage removal of copper varies from 16% to 68% for the pH range of 2-10 and the percentage removal of zinc varies from 12% to 58% for the pH range of 2-10 respectively. It was observed that the adsorption capacity of adsorbents increased when pH of heavy metal solution increased. As pH value increases, the extent of removal increases, reaches a maximum value and then decreases further increased up to optimum pH.

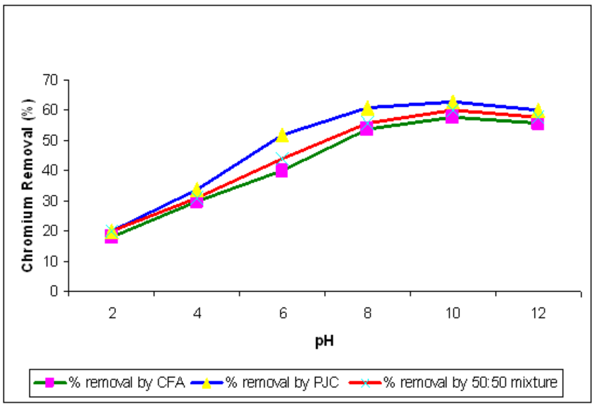

Figure 9. Effect of pH for Cr removal

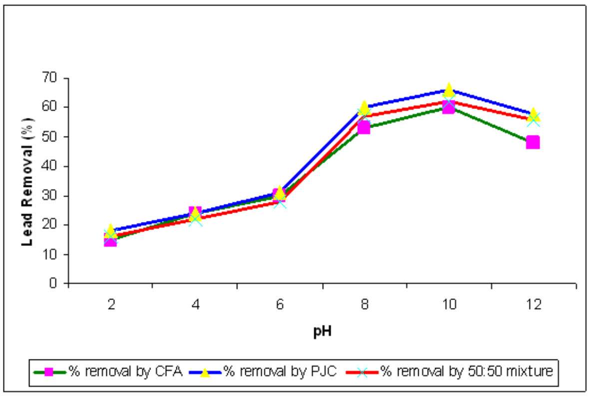

Figure 10. Effect of pH for Pb removal

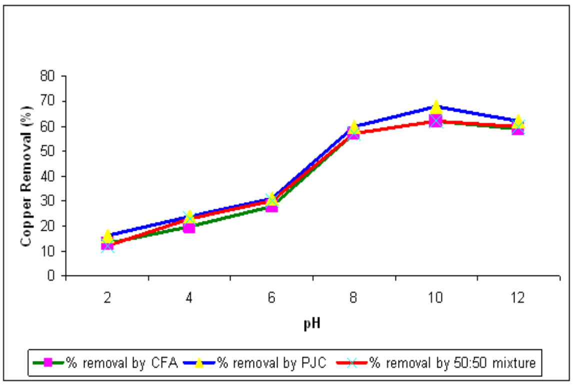

Figure 11. Effect of pH for Cu removal

The optimum pH, for the removal of Cr^{6+} is fixed as 8.5 for CFA, PJC and 50:50 mixture, for the removal of Pb^{2+} is fixed as 9.0, for the removal of Cu^{2+} is fixed as 8.2 and for the removal of Zn2+ is fixed as 8.3 respectively. A slight alkaline pH is found to be favourable. The pH value slightly decreases and change in pH (ĂpH = initial pH – final pH) values after adsorption are found to decreases in the order of 0.2 to 0.5 units. This suggests that during the adsorption of heavy metal species, protons are released from the surface functional groups like phenolic, carboxylic and enolic groups present on the carbons.

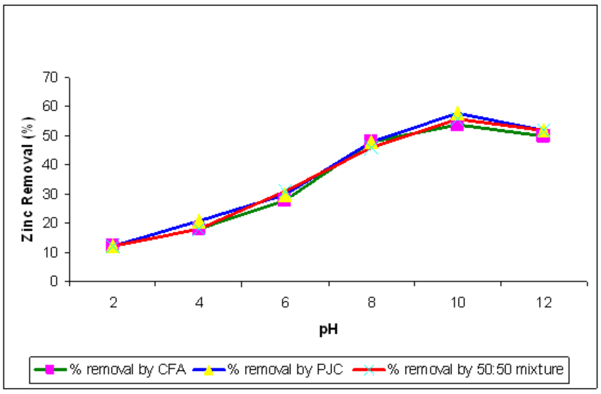

Figure 12. Effect of pH for Zn removal

These adsorption data suggest that the studied alternatives could be used as low cost adsorbent alternative to any other adsorbent which is currently used for the cost effective treatment of effluents, especially for the removal of metal ions.

Effect of contact time

The influence of the contact time on the removal of heavy metal ions at different time intervals ranging from 15 min to 180 min while keeping the concentration of the individual solution constant under optimum temperature 296 K and adsorbent dosage of 50 g L^{-1} was studied. The figure 13 to 16 in this chapter explains the removal of Cr, Pb, Zn and Cu is optimum at the contact time of 60 minutes.

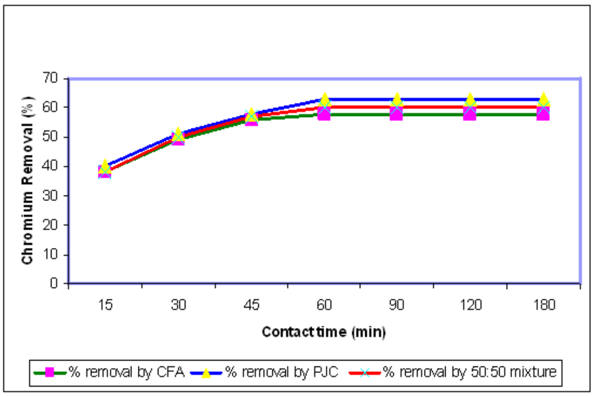

Figure 13. Effect of contact time for Cr removal

Adsorption mechanism

In the present study, the initial pH of solution is maintained at pH value 3. At the lower value of pH, in case of Cr(VI) is $HCrO_4^-$ while the surface of adsorbent is charged positively. The increase in Cr(VI) adsorption is due to the electrostatic attraction between positively charged groups of adsorbent surface and the $HCrO_4^-$ which is dominant at lower value of 3. Similarly, other heavy metal ion shows increased adsorption due to certain interaction.

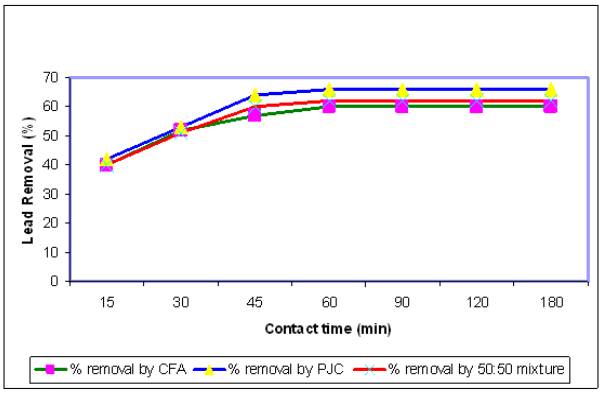

Figure 14. Effect of contact time for Pb removal

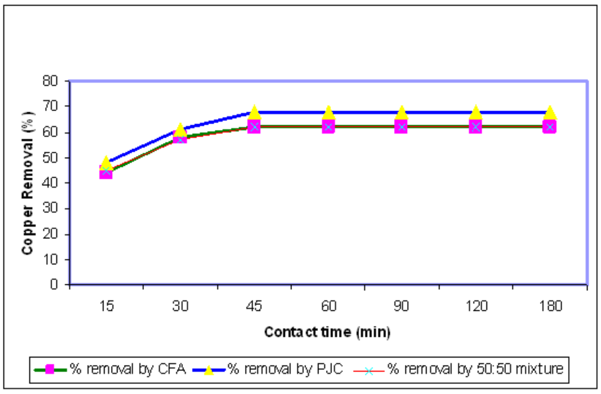

Figure 15. Effect of contact time for Cu removal

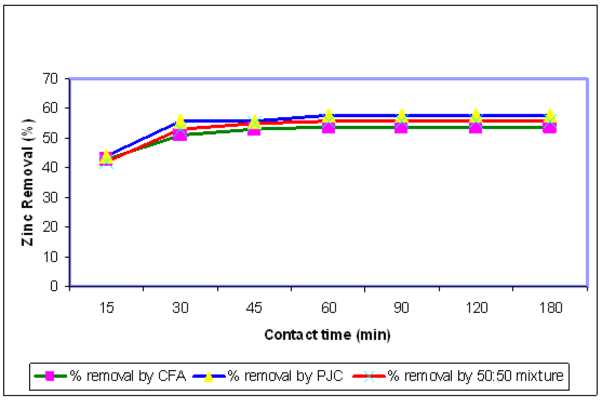

Figure 16. Effect of contact time for Zn removal

Adsorption Isotherm

In the present study, as the new adsorbent is developed, hence it is needed to test the equilibrium data obtained for heavy metal ions removal using activated tamarind seeds with different isotherm models available in the literature. In the present work, Freundlich isotherm model is tested with the experimentally obtained equilibrium data.

Freundlich Isotherm model

The adsorption data are fitted with the linearised form of Freundlich adsorption isotherm:

DOI: 10.17628/ecb.2012.1.161-167

$$\log (x/m) = \log k + (1/n) \log C_e \quad (1)$$

Where, (x/m) is the amount of adsorbate adsorbed per unit mass of the adsorbent, C_e is the equilibrium concentration and k and 1/n are the Freundlich constants, which are the measure of the adsorptive capacity and adsorption intensity, respectively. The $\log(x/m)$ values are found to be linearly correlated to the log C_e values in the case of all the adsorbents. The computed r values which are very close to unity conclude that the Freundlich model is applicable to the experimental data.

The observed high values (2 to 4) of 1/n in the case of all the adsorbents indicate an adsorption mechanism with an intraparticle diffusion or mass transfer as the rate limiting step. The increasing order of the adsorptive capacities of these adsorbents as indicated by the k values (log k values) for CFA, PJC and 50:50 mixture.

Adsorption kinetics

In order to understand the kinetics of removal of hexavalent chromium, divalent lead, divalent copper and divalent zinc using CFA, PJC alone and 50:50 mixture as an adsorbent, pseudo first order and second order kinetics are tested with the experimental data. As per the application of second order kinetics, it obeys better than any other.

Pollution index

The pollution index was used in this study to evaluate the degree of heavy metal contamination. The tolerable level of the element concentration in the water considered safe for human consumption. The BIS drinking water standards (2009) were used as tolerable level for water and the pollution index can be calculated by the formula below.

$$PI = \frac{C_{Me} / C_T}{N} \quad (2)$$

where C_{Me} is the heavy metal concentration in water, C_{T} is the tolerable level, and N is the number of heavy metals. The PI among all sites varied from 0.01 to 1.5 and 0.106 to 5.0 for highly polluted and less polluted sites respectively. Concentrations of lead and chromium in most of the water samples were comparatively high than the given tolerable levels while in few water samples showed lower concentration. PI was below 0.1 at 4 and 6 sample representing (27.2 and 37.5%) of the total samples, between 0.1 to 0.3 at 6 and 8 samples (37.5 and 50%) and greater than 0.3 at 5 and 2 samples (33.3 and 12.5%) for least treating industries, respectively.

Conclusion

The following conclusions could be drawn from the present study:

The maximum adsorption of Cr(VI), Pb(II), Cu(II) and Zn(II) was observed at the pH value of 8.5, 9.0, 8.2 and 8.3 respectively.

The equilibrium time for the adsorption of Cr(VI), Pb(II), Cu(II) and Zn(II) on the CFA, PJC and 50:50 mixture ranges from is 45 to 90 minutes.

The percentage removal of Cr(VI), Pb(II), Cu(II) and Zn(II) increases with increase in the adsorbent amount. Optimum dose found in this study for various adsorbents ranges from 30 to 50 g L^{-1}.

The equilibrium data obtained for the adsorption of Cr(VI), Pb(II), Cu(II) and Zn(II) can be well described by Freundlich adsorption isotherm model.

Adsorption follows and obeys second order rate equation.

Among the various adsorbents, PJC (*Prosopis Juliflora* Carbon) proves that as a waste material has negligible cost and has also been proved to be an efficient alternative to commercial activated carbon.

Acknowledgement

The authors are highly thankful to their respective Management and Principal for providing necessary facilties.

References

[1] Khan, N. A., Ibrahim, S. and Subramaniam, P., *Malaysian J. Sci.*, **2004,** *23*, 43.

[2] Chandra, B. S.. Saswati, G. and Chand, G. U., *J. Environ. Sci. Eng.*, **2005**, *47*(4), 316.

[3] Rao, M., Parwate A.V. and Bhole, A.G., *J. Environ Std. Policy*, **2001**, *4*(1), 11.

[4] Gopalakrishnan, K. and Jeyadoss, T. *Indian J Chem Tech.*, **2011**, *18*, 61.

[5] Lark, B. S., Mahajan R.K. and Walia, T.P.S. *Indian J. Environ. Health.*, **2002**, *44*(2), 164.

[6] Robinson, T., Chandran, B. and Nigam, P., *Bioresource Technol.*, **2002**, *84*(3), 299.

[7] Saravanane, R., Sundarajan, T. and Reddy, S. S., *Indian J. Environ. Health*, **2002**, *44*(2), 78.

[8] Kadirvelu, K., Senthil Kumar, P., Tamaraiselvi, K. and Subburam, V., *Bioresouce Technol.*, **2002**, 81(1), 87-90.

Received: 06.09.2012.

Accepted: 10.09.2012.s

ECONOMIC BENEFITS OF C_2 UTILIZATION IN CHINA

Lu Hongjie[a] and Linda Zhang[b]

Keywords: economic benefits; C_2 utilization; ethylene production from bioethanol; chloroethylene production;

Resources and utilization of C_2 compounds in China has been reviewed. Transformations of bioethanol feedstock into ethylene, acetylene and ethylene feedstocks into chloroethylene, and ethylene feedstock into ethylene oxide have been discussed, and effects of these processes on the energy utilization and environmental damage have been evaluated. The viewpoints of economic or social benefits have also been discussed.

* Corresponding Author
Fax: 1-403-2649136
E-Mail: lindazhang362@hotmail.com
[a] Liaoning Shihua University, Fushun, Liaoning, P.R. China.
[b] SAIT Polytechnic, Calgary, AB, Canada.

INTRODUCTION

With the decrease of available mineral oil resources, the importance of traditional energy resources, such as coal and natural gas, increases and converting C_2 components into higher value products becomes more and more important. This latter is expected to result in economic and social benefits[1].

Chinese economic and social development has been limited due to the shortage of natural resources. The output of Chinese crude oil production has been varied between $1.8x10^8$ and $2.5x10^8$ t per year.[2] Since the Chinese crude oil reservation is about $32.7x10^8$ tons, the known crude oil resources are expected to cover the Chinese demands only for 16 years. Since 52% of the processed crude oil comes from overseas, the Chinese government introduced various policies to increase the energy production efficiencies[3] and to decrease taxes for those companies which turn efforts to use renewable energy resources such as wind, water, C_2, etc.

Nowadays the efficiency of C_2 utilization is very low in China, because most of these resources are fired and discharged into the environment. This latter has a serious negative effect on our health and living, strongly degrades the environment, and causes serious pollution; therefore researchers and engineers turn a lot of effort in the development of this area, focusing on increasing the efficiency of C_2 source utilization with maximal economic benefits.

It is an urgent demand to utilize C_2 sources in a more rational way as simple fuel, involving new processes, which could result in improving the product's value. These new processes could improve the energy efficiency and decrease the environmental pollution as well. In this paper, three important methods are reviewed, namely the production of ethylene, chloroethylene, and ethylene oxide, based on various C_2 sources.

DISCUSSION

Alcohol as feedstock to produce ethylene

Gong Linjun [4] developed a method to produce ethylene using bioethanol as C_2 resource. Effects of the reaction temperature, the concentration of alcohol, and the liquid weight hour space on the yields of ethylene were studied in detail.

Table 1 shows the effect of reaction temperature on the yield of ethylene at 10% feedstock ethanol concentration (mass percentage), 150 °C ethanol input temperature, and 0.3 h^{-1} liquid weight hour space velocity. The yield of ethylene firstly increased then decreased with the increase of the reaction temperature. The maximal ethylene yield (99.8%) was observed at 360 °C.

The effect of ethanol concentration on the yield of ethylene can be shown in Table 2. The reaction temperature, input temperature of ethanol, and the liquid weight hour space velocity were 340 °C, 150 °C, and 0.3 h^{-1}, respectively. Keeping the reaction temperature at 340 °C, the yield of ethylene was proven to be more than 97% between 10 and 70 % ethanol concentration. However, above 95 % ethanol concentration the yield of ethylene decreased to 83.5%.

Table 3 shows the effect of liquid weight hour space velocity on the yield of ethylene at two different ethanol concentrations. The reaction temperature, ethanol concentrations, and the input temperature of alcohol were selected to be 340 °C, 40 and 70%, and 150 °C, respectively. At 0.6 h^{-1} liquid weight hour space velocity the yield of ethylene was more than 98%, but increasing the liquid weight hour space velocity above 0.6 h^{-1}, the yield of ethylene decreased to 92.6%. The ethanol concentration has no significant effect on the ethylene yield in this concentration range.

Acetylene and ethylene as feedstocks to generate chloroethylene

Wang Xianzhong[5] developed a method for producing chloroethylene by using a combined gas (acetylene and ethylene) mixture as feedstock with utilization of residual heat of acetylene heater. The feedstocks (acetylene and ethylene) were obtained from Chongqing Chemical Institute. The compositions of C_2 mixture can be seen in Table 4.

The main reactions are the followings.

$$C_2H_4 + Cl_2 \rightarrow C_2H_4Cl_2 \quad (1)$$

$$C_2H_4Cl_2 \rightarrow C_2H_3Cl + HCl \quad (2)$$

$$C_2H_2 + HCl \rightarrow C_2H_3Cl \quad (3)$$

Eqn. (1), (2), and (3) can be combined and expressed as Eqn. (4).

$$C_2H_4 + Cl_2 + C_2H_2 \rightarrow 2\ C_2H_3Cl \quad (4)$$

DOI: 10.17628/ecb.2012.1.168-169

Table 1. The effects of reaction temperature on the yield of ethylene

Reaction temperature (°C)	160	220	240	300	320	360	420
Yield of ethylene (%)	6.9	49.3	67.2	68.9	98.6	99.8	96.5

Table 2. The effect of alcohol concentration on the yield of ethylene

Concentration of alcohol (%)	10	40	70	95
Yield of ethylene (%)	99.8	97.6	98.5	83.5

This method is called “One Heater and Three Gases” procedure. Three gases are acetylene, ethylene, and chlorine. They were purified before use. Acetylene was mixed with hydrogen chloride in the acetylene reactor for producing chloroethylene. Ethylene gas was introduced into the reactor and reacted with chlorine to produce dichloroethane. Dichloroethane was used as feedstock and cracked into chloroethylene and hydrogen chloride. Hydrogen chloride was recycled into the acetylene reactor, and the tail gas of the acetylene reactor could be used to produce methanol, dimethyl ether, ammonia, chloroethylene, and polyvinyl chloride. Chongqing Chemical Institute developed this method (“One Heater and Three Gases”) and could improve the efficiency of the acetylene heater unit with ca. 22.8% and could increase the capacity of acetylene heater and the output of acetylene with about 1.5 times and 10.7%, respectively.[5]

Ethylene conversion to ethylene oxide

Wang Chenggang[6] developed a method to oxidize ethylene directly to ethylene oxide. A fixed-bed tube reactor was evaluated in the framework of a one dimensional pseudo homogenus reactor model. This model was proven to be reliable based on the comparison of calculated and measured industrial results. The activity correction coefficient was calculated by a multi-objective optimization method based on the macroscopic reaction kinetics of silver catalyst. Variations of activity correction coefficients with time were investigated and provided certain theoretic reference for the later operation of production.

Table 3. The effects of liquid weight hour space on the yield of alcohol

Mass percentage of alcohol (%)	40	40	40	70	70	70	70
Liquid weight hour space (h^{-1})	0.2	0.3	0.4	0.4	0.5	0.6	0.7
Yield of ethylene (%)	99.8	99.8	99.8	99.8	99.8	99.5	99.6

Generation of ethylene from bioethanol

Yang Bo [7] developed a new technology for ethylene production from bioethanol using dehydration catalysts. The trend of catalyst development was pointed out according to the problems existed in bioethanol dehydration. China is one of the largest of agricultural countries and has no less than 10 billion tons of biomass (such as corn, potato, cane, and so on), which is converted into about 3 billion ton of bioethanol every year. Bioethanol is a renewable source, which can be transformed directly into ethylene. Ethylene can be produced this way in higher purity and with lower separation and investment costs than the ethylene from mineral oil.

Table 4. Composition of the C_2 raw material, % (v/v)

Composition	Content, v%
C_2H_2	6.0 ~ 7.5
C_2H_4	7.0 ~ 9.0
CO	19.0 ~ 21.5
CO_2	2.4 ~ 2..75
CH_4	9.6 ~ 14.5
H_2	44.5 ~ 49.5
C_2H_6	0.25 ~ 0.5
C_3H_6	1.1 ~ 1.75
C_3H_8	small amounts
N_2	0.3 ~ 0.5
O_2	0.05 ~ 0.2

CONCLUSION

The C_2 sources can be used to produce high value chemicals in China. These C_2 source based methods protect the environment and increase the income of a petrochemical plant. The main benefits are as follows: using coal and protecting the local environment, decreasing fossil fuel consumption, and avoiding greenhouse gas emissions, such as SO_2, NO_x, and CO_2, and total suspended particles. Economic developments are initiated and improved using the reviewed new developments.

REFERENCES

[1] Ma, Z. Y., Meng, X. Y, Wang, H. W., Zhou, W. and Jiang, H. Y. *Petrochemicals*, **2009**, *38*(4), 456.

[2] Li, Z. L. *Chem. Catal. Methanol Technol.*, **2007**, *6*, 16.

[3] Gu, W. *Sandong Chem. Ind.*, **2002**, *31*(5), 23-26.

[4] Gong, L. J., Han C. and Tan T. W. *Ind. Technol.*, **2006**, *10*, 56.

[5] Wang, X. Z., Wu, Y. and Wang, H. R. *Petroleum and Natural Gas Ind.*, **2003**, *32*(1), 7.

[6] Wang, C. G., Li, T., Ying, W. Y. and Fang, D. Y. *Chem. Product. Technol.*, **2009**, *16*(6), 23-25.

[7] Yang, B. and Zhou H. *Technol. Dev.Chem. Ind.*, **2009**, *38*(12), 27.

Received: 02.09.2012.

Accepted: 13.09.2012.

AN OVERVIEW OF SHALE OIL UTILIZATION

Zhang Yongmei,[a] and You Hongqing[b]*

Keywords: oil shale; shale oil; utilization; overview; processing, recovery of rare earth metals

The contribution of shale oil as raw material to the mineral oil processing industry has been increased due to the worldwide energy demand. This review article discusses the principles of shale oil processing using rotary dry distillation boilers and the practical applicability of shale oil. The complete utilization of oil shale sources results in good economic and social benefits.

* Corresponding Author
Fax: 86-24-56320177
E-Mail: zh6688551@163.com
[a] Liaoning Shihua University, Fushun, Liaoning, P.R. China.
[b] Fushun Petrochemical Plant, Fushun, Liaoning, P.R. China.

Introduction

Oil shale is a solid-state organic-rich sedimentary and combustible rock with high ash content.[1] Shale oil recovered from oil shale contains not only a lot of unsaturated hydrocarbons but numerous non-hydrocarbon compounds, which cause its bad stability and black colour.[2]

Oil shale comprises a host rock and kerogen material, which can be transformed into conventional light oil without elevated temperature and pressure. Oil shale can be found near the surface, which is advantageous in using as source of liquid fuels, compared to mineral oil or coal. There are about 1.5 trillion of barrels of oil shale which is located near the borders of Wyoming, Utah, and Colorado. Shale oil as a supplemental energy source provides economic and social benefits for public.[3]

In this paper, the main properties, processing, and utilization of shale oil are reviewed, including a detailed discussion of processing using a rotary dry distillation boiler.

Discussion

Properties of shale oil

Table 1 shows the properties of different shale oil samples.[4] The composition and properties, such as density, wax content, setting point, and asphaltene content of different shale oils vary between a wide range, but the ratio of carbon to hydrogen generally varies between 7 and 8, which is very close to the relevant value of petroleum. Shale oil as fuel may become an important substitute of petroleum in the near future.

Shale oil contains a lot of unsaturated hydrocarbons and non-hydrocarbon compounds as well. *Fushun* shale oil has higher nitrogen content than that of *Maoming* or *Estonia*, while *Estonia* shale oil has higher oxygen content than shale oils from other sources (see Table 1). Mineral oils, however, contains in general smaller amounts of unsaturated hydrocarbons, nitrogen or oxygen compounds than shale oil.

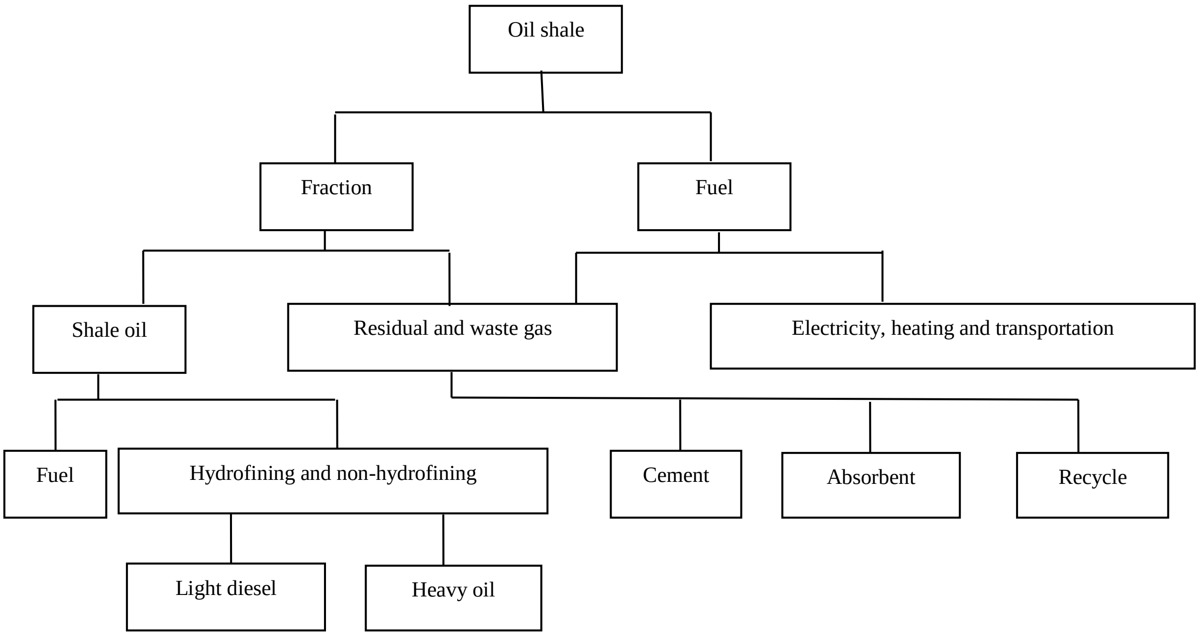

Figure 1. Flow chart of oil shale utilization

DOI: 10.17628/ecb.2012.1.108-111

Fushun shale oil contains less amount of light fraction, e.g. its gasoline fraction content is varied between 2.5 and 2.7 % and the amount of fraction boils below 360 °C is varied between 40 and 50%. Its wax and residual oil content were between 25 and 30% or 20 and 30%, respectively.[5] *Fushun* shale oil belongs to the group of high nitrogen compound containing paraffinic oils with high wax content and setting point, and low asphaltene content.

Shale oil processing in the world

Two kinds of oil shale processing exist, the so-called underground and the above-ground retorting.[6] In the underground retorting method the oil shale is not mined out, but treated locally at its occurrence site in the deepness, then the oil is pumped out to the ground. This processing can cause environmental pollution, thus it is not a widely used method. The above-ground retorting means that oil shale is mined and processed into oil at the ground.

Table 2 shows the parameters of main oil shale processing plants. There are low outputs (100 t per day) in *Fushun* and *Kivioli*, due to sites are wide-spread. Shale oils in *Fushun* and Kivioli ensure about 65 % output yields, but only low heating value shale ash is obtained. Higher output yields (between 1500 and 6000 tons/day) are found in *Sao Mateus*, *Narva*, and *Stuart*. Yield of oils varies between 80 and 90 % and shale ash residues have high heating value.

Shale oil utilization

Due to improving processing technologies and environmental protection requirements, over using as simple energy source new utilization possibilities of shale oil have been appeared.[7] They improve utilization efficiencies of shale oil resources, decrease specific investment costs and decrease environment pollution.

Figure 1 shows the flow chart of oil shale utilization. Oil shale can directly be used as fuel or can be fractionated. Shale oil, one of the main fractions which can be separated into components by distillation, is used as fuel. Light diesel and heavy oil fractions obtained by hydrofining or non-hydrofining methods increase the value of shale oil. On the other hand, oil shale can directly be used as fuel to generate electricity or steam, e.g. *Estonia* uses oil shale to generate electricity and heat in power plants. The ratio of produced electricity and heat from shale oil based on tax in Estonia is 76% to 14%, respectively. The combustion residues can be used to fill wells, generate cement or brick. Waste gases can also be burnt to provide energy.

Processing in a rotary dry distillation boiler

Combustion Resources Company developed a new shale oil treatment technology and designed a new rotary dry distillation boiler which is shown in Figure 2.[8] The boiler has indirect heating, simple construction, and good performance, and the shale and the shale oil can be easily separated without environmental pollution. Figure 3 shows the flow chart of the rotary dry distillation boiler. It consists of a unit for the generation of hydrogen, a unit to produce shale oil, and a unit for fining of shale oil. Coal is used as raw material for low price hydrogen production. Oil shale was grounded (<10mm) and transported into the rotary dry distillation boiler, which was heated up to 500 °C indirectly with the produced hydrogen. Shale oil gas was separated and recycled. Shale oil and heavy carbon were cracked and fined to obtain different motor fuels.

Table 1. Properties of different shale oils

Name	Fushun	Maoming	Estonia	USA
Density (20°C)/kg·m^{-3}	903.3	912.2	1010	934.0
Setting point °C	33	30	-15	24
ω (Wax), %	20.2	13.2	-	-
ω (Asphaltenes), %	0.85	1.54	-	-
ω (Gum), %	42	43	-	-
Distillation range °C				
IBP	216	214	190	66
30%	318	306	320	326
50%	362	350	370	410
ω Element analysis %				
C	85.39	84.82	83.30	84.69
H	12.09	11.40	10.00	10.71
S	0.54	0.48	0.70	0.84
N	1.27	1.10	0.30	1.85
O	0.71	2.20	5.70	1.90
C/H	7.06	7.44	8.33	7.90

DOI: 10.17628/ecb.2012.1.108-111

Table 2. The main oil shale processing plants in the world

Country	Place	Oil shale (t/d)	Shale (m/m)	Yield (%)	Production
China	Fushun	100	10-75	65	Fuel, low heating value gas, shale ash
Estonia	Kivioli	100	10-100	68	Fuel, chemicals, low heating value gas, shale ash
Brazil	Sao Mateus	1500 and 6000	6-50	85-90	Light oil, sulfur, high heating value gas, shale semi-coke
Estonia	Narva	3000	0-25	85-90	Fuel, chemicals, high heating value gas, shale ash
Australia	Stuart	6000	0-16	85-90	Light fuel, light oil with low S content, high heating value gas, shale ash

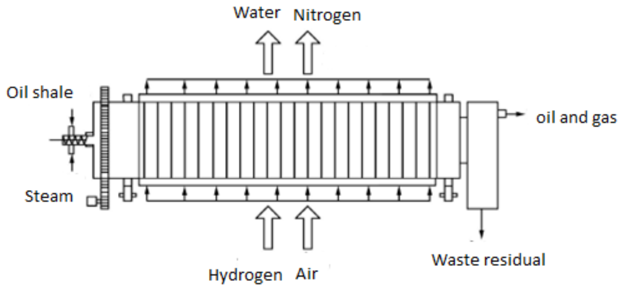

Figure 2. Construction of the rotary dry distillation boiler

The practical appliance of shale oil in China

The Chinese government implemented several policies to save energy and green environment, thus researchers are working to fulfil these requirements, for example, in the field of utilization and processing of shale oil. The main research areas are focusing on the distribution and reserve of shale oil, and on the development of new processing methods and equipments. Industrialization of these methods is in progress; e.g. *Fushun* Shale Oil Plant started its operation in 1989 and by now the output of the plant has already reached 9 million tons/year.[9]

Chinese economy requires large amount of mineral oil, and considerable amount of mineral oil has to be imported from other countries. This situation damages the Chinese petroleum strategy, so introduction of other mineral oil based product sources as shale oil is very important for China. The Chinese petroleum strategy has to be adjusted toward energy safety control and environment protection policies.

Oil shale provides different quality fuel materials, fuel gas and raw material for production of various chemicals. The residues of oil shale separation can be used for manufacturing bricks and cement. For example, heating 1000 kg of grounded oil shale at 500 °C produces shale oil in the amount varied between 38 and 378 L.

Hydrocracking of shale oil produces gasoline, kerosene, diesel oil, wax, and paraffin oils.

Oil shale can be used directly as fuel in power plants to provide electricity. Oil shale can also be separated into shale oil, fuel gas, and shale residue. The shale residue can be used to produce brick and cement, and for the recovery of different rare earth elements, such as La, Ce, Pr, Nd, Sm, Eu, Ho, Er, Tm, Yb, Lu, and Y, and to produce different kinds of manure.[10]

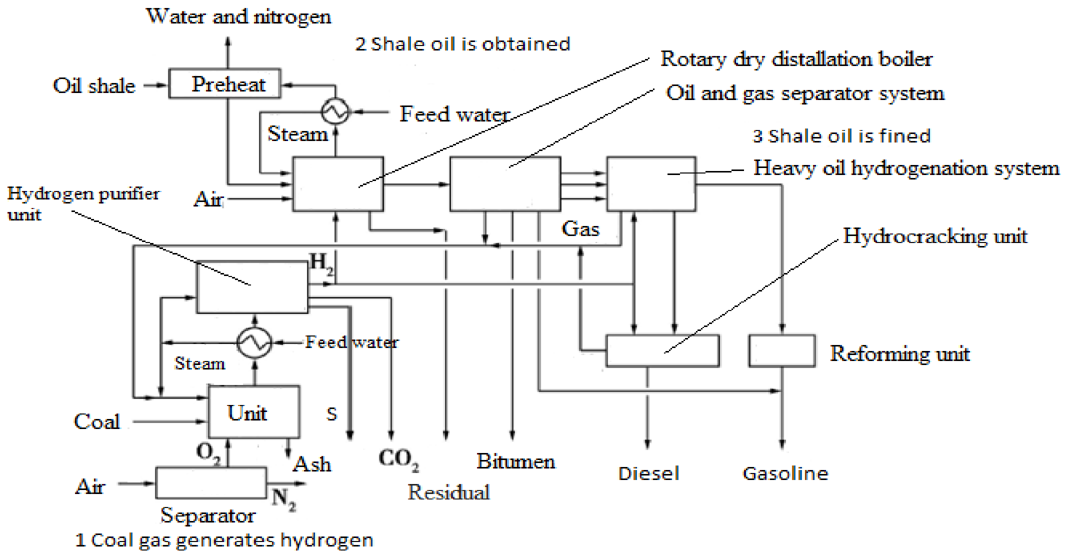

Figure 3. Flow chart of the rotary dry distillation boiler

Conclusion

Shale oil can be used directly as fuel instead of coal, or can be transformed into more valuable products in order to meet Chinese energy requirements. Utilization of shale oil provides less damage to the natural environment and ensures other economic advantages as well. There is a huge demand to find possibilities and opportunities to utilize shale oil in different petrochemical processes, in more rational way than a simple combustion, with introduction of new technologies. These new methods are expected to improve energy efficiency and to reduce pollution and damage toward the ecological environment.

References

[1] Sun, B. Z., Wang, Q., Shen, P. Y. Qin, H. and Li, S. H. *Oil Shale*, **2012**, 29(1), 63.

[2] Zhao, G. F., Yao, C. L. and Quan H. *Contemporary Chem. Ind.*, **2008**, *37*(5), 496.

[2] Zhao, G. F., Yao, C. L. and Quan H. *Contemporary Chem. Ind.*, **2008**, *37*(5), 496.

[3] Qian, J. L., Wang, J. Q. and Li, S. Y. *Chinese Energy*, **2006**, *28*(8), 16.

[4] Chi, Y. L., Li, S. Y. and Yue C. T. *Modern Chem. Ind.*, **2005**, *25*, 44.

[5] Song, Y. *Coal Process. Utilization*, **2004**, *4*, 49-51.

[6] Qian, J. L. and Wang, J. Q. *J. China Foreign Energy*, **2007**, *12*(1), 7.

[7] Li, D. M., Tang, D. Z. and Yang, Y. F. *Petroleum Exploration and Dev.*, **2006**, *33*(6), 657.

[8] Hatfield, K. E., Coates, R. L., Smoot, L. D., US 2008202985.

[9] He, H. M., Xu, D. P. and Zhang, X. L. *Clean Coal Technol.*, **2002**, *8*(2), 44.

[10] Chen, X. F., Gao, W. J., Zhao, J., Huang, J. N., Wu, Y. X., Zhang, J. Q., Dou, J. L., Tian, P. J. and Zhang, Z. M. *Clean Coal Technol.*, **2010**, 6, 29.

Received: 01.09.2012.
Accepted: 16.09.2012.

DOI: 10.17628/ecb.2012.1.170-173